

**PHYSICAL PROPERTIES OF FOOD OILS AND FACTORS
AFFECTING BUBBLE DYNAMICS DURING FRYING**

by

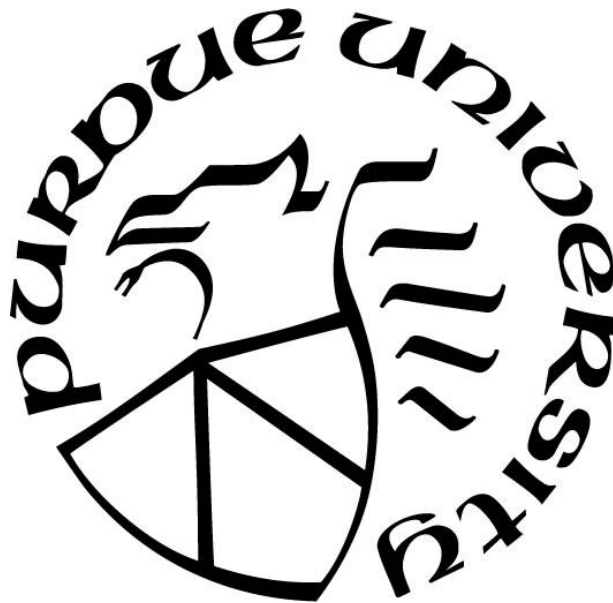
Shreya N. Sahasrabudhe

A Dissertation

Submitted to the Faculty of Purdue University

In Partial Fulfillment of the Requirements for the degree of

Doctor of Philosophy



Department of Food Science

West Lafayette, Indiana

May 2019

**THE PURDUE UNIVERSITY GRADUATE SCHOOL
STATEMENT OF COMMITTEE APPROVAL**

Dr. Brian Farkas, Chair

Department of Food Science

Dr. Carlos Corvalan

Department of Food Science

Dr. Owen Jones

Department of Food Science

Dr. Osvaldo Campanella

Carl E. Haas Endowed Chair in Food Industries

Department of Food Science and Technology, Ohio State University

Approved by:

Dr. Arun Bhunia

Head of the Graduate Program

Dedicated to my Parents, Mrs. Amita and Mr. Narayan Sahasrabudhe and my husband, Mr. Sameer Kulkarni for their guidance and unconditional love and support to help me succeed through this journey.

ACKNOWLEDGMENTS

I wish to extend my deepest gratitude to my advisor, Dr. Brian Farkas for his constant support, encouragement and guidance throughout my graduate program. I have learned a great deal from him about what it is to be a true scientist and engineer. I would also like to thank my committee members: Dr. Carlos Corvalan, Dr. Owen Jones, and Dr. Osvaldo Campanella for serving as my graduate advisory committee and for guiding me throughout my program at Purdue University. I am thankful to my friends and lab mates for making my time at Purdue enjoyable. Finally, I would like to thank my family for their unwavering support and patience in overcoming the numerous obstacles I faced through my research.

TABLE OF CONTENTS

LIST OF TABLES	9
LIST OF FIGURES	10
LIST OF ABBREVIATIONS.....	13
ABSTRACT.....	14
1. INTRODUCTION.....	16
1.1. Frying process	16
1.1.1. Physical and chemical changes during frying.....	16
1.1.2. Frying and health impact.....	17
1.2. Mechanisms for heat and mass transfer during deep-fat frying.....	17
1.2.1. Heat transfer during immersion frying.....	17
1.2.2. Oil absorption during immersion frying and post-frying cooling.....	18
1.2.2.1. Capillary mechanism	19
1.2.2.2. Condensation mechanism.....	19
1.3. Factors affecting oil absorption during deep-fat frying.....	20
1.3.1. Effect of oil quality (properties) on oil absorption.....	20
1.3.1.1. Density.....	21
1.3.1.2. Viscosity	22
1.3.1.3. Surface tension	23
1.3.1.3.1. Pendant drop.....	24
1.3.1.3.2. Sessile drop	25
1.3.1.3.3. Wilhelmy plate	26
1.3.1.3.4. Maximum bubble pressure.....	27
1.3.2. Effect of product properties on oil absorption	27
1.3.2.1. Moisture content	27
1.3.3. Effect of process parameters: Frying oil temperature and frying time.....	28
1.4. Studies on techniques for oil absorption reduction	29
1.4.1. Pre-frying treatment techniques	29

1.4.2.	Modification of frying methods	30
1.4.3.	Use of barrier layers/ coatings.....	31
1.5.	References	33
2.	DETERMINATION AND MODELING OF DENSITY, VISCOSITY AND SURFACE TENSION OF FIVE VEGETABLE OILS AT ELEVATED TEMPERATURES	38
2.1.	Introduction	38
2.2.	Materials and Methods	41
2.2.1.	Materials.....	41
2.2.2.	Density measurements.....	41
2.2.3.	Surface tension measurements	42
2.2.4.	Viscosity measurements	43
2.2.5.	Mathematical modeling.....	43
2.2.5.1.	Density.....	43
2.2.5.2.	Surface Tension	45
2.2.5.3.	Viscosity	45
2.1.1.	Percentage error.....	46
2.2.6.	Statistical Analysis	46
2.3.	Results and Discussion.....	46
2.3.1.	Effect of temperature and oil type on physical properties of oils	46
2.3.1.1.	Density.....	46
2.3.1.2.	Surface tension	48
2.3.1.3.	Viscosity	51
2.3.2.	Mathematical modeling of physical properties of oils at high temperatures	53
2.3.2.1.	Density.....	53
2.3.2.2.	Surface tension	56
2.3.2.3.	Viscosity	59
2.4.	Conclusions	62
2.5.	Acknowledgement.....	62
2.6.	References	62

3. EFFECT OF FRYING OIL DEGRADATION ON SURFACE TENSION AND WETTABILITY	65
3.1. Introduction	65
3.2. Materials and Methods	67
3.2.1. Total polar materials (TPM) measurement	68
3.2.2. Viscosity measurement	68
3.2.3. Measurement of air-oil surface tension (ST).....	68
3.2.4. Measurement of steam-oil surface tension.....	68
3.2.5. Measurement of dynamic air-oil surface tension	69
3.2.6. Contact angle measurements.....	70
3.2.7. Statistical analysis	70
3.3. Results and Discussion.....	71
3.3.1. Total polar materials.....	71
3.3.2. Dynamic Viscosity	71
3.3.3. Surface tensions (ST)	72
3.3.4. Contact angle.....	74
3.4. Conclusion.....	79
3.5. Acknowledgment.....	79
3.6. Funding source	79
3.7. References	80
4. EXPERIMENTAL MEASUREMENT OF FACTORS AFFECTING DYNAMICS OF BUBBLE GROWTH FROM A SUBMERGED ORIFICE: APPLICATIONS TO THE FRYING PROCESS	83
4.1. Introduction	83
4.2. Materials and Methods	87
4.2.1. Total polar materials (TPM) measurement	88
4.2.2. Submerged orifice assembly set-up and image processing.....	88
4.3. Uncertainty analysis	89
4.4. Theory.....	90
4.5. Results and Discussion.....	91
4.5.1. Effect of temperature.....	93

4.5.2.	Effect of surface wettability	95
4.5.3.	Effect of oil quality	97
4.5.4.	Effect of orifice diameter	99
4.5.5.	Effect of bubble dynamics on heat transfer.....	101
4.6.	Conclusion	104
4.7.	Funding sources	104
4.8.	Acknowledgements	104
4.9.	References	104
5.	PARAMETRIC STUDY ON LIQUID AND SURFACE PROPERTIES AFFECTING MENISCUS DYNAMICS DURING BUBBLE FORMATION	107
5.1.	Introduction	107
5.2.	Materials and Methods	113
5.2.1.	Protocol for silanization of glass	113
5.2.2.	Surface tension measurement- rising bubble.....	114
5.2.3.	Contact angle measurements	114
5.2.4.	Maximum bubble pressure tensiometer (MBPM).....	114
5.2.5.	Submerged orifice assembly (SOA).....	115
5.2.6.	Force of curvature estimation.....	116
5.2.7.	Design of experiments.....	116
5.2.8.	Statistical analysis	117
5.3.	Results and Discussion	118
5.3.1.	Effect of capillary diameter.....	121
5.3.2.	Effect of liquid viscosity	124
5.3.3.	Effect of surface tension and contact angle.....	125
5.4.	Conclusion	131
5.5.	References	131
6.	CONCLUSIONS AND FUTURE WORK.....	134

LIST OF TABLES

Table 2.1. Molecular weight, critical properties and Racket parameters of fatty acids	45
Table 2.2. Comparison of the average density values between five vegetable oils at different temperatures	47
Table 2.3. Intercept (ρ_0), slope (ρ_1) and correlation coefficient r^2 values corresponding to the empirical equation to predict density of each vegetable oil.....	48
Table 2.4. Intercept (γ_0), slope (γ_1) and correlation coefficient r^2 values corresponding to the empirical equation to predict surface tension of each vegetable oil	49
Table 2.5. Comparison of the average surface tension values between five vegetable oils at different temperatures measured using KRÜSS and ramé-hart goniometers	50
Table 2.6. Comparison of the average viscosity values between five vegetable oils over a range of temperatures.....	52
Table 2.7. Parameters a and b, and correlation coefficient r^2 values corresponding to the empirical equation to predict viscosity for each vegetable oil.....	53
Table 2.8. Molecular weight, critical temperature, and critical pressure of five vegetable oils ..	55
Table 2.9. Predicted density values for each vegetable oil by the modified Rackett equation and their corresponding percentage error	55
Table 2.10. Predicted surface tension values for each vegetable oil by the Eötvös equation ($KE = 6.2 \text{ dynes}\cdot\text{cm}/\text{mol}^{2/3}\cdot\text{K}$) and their corresponding percentage error comparing with experimental data obtained using KRÜSS goniometer	58
Table 2.11. Parameters a, b and c corresponding to the modified Andrade equation used to predict the viscosity of each vegetable oil	59
Table 2.12. Predicted dynamic viscosity values for each vegetable oil by the modified Andrade equation and their corresponding percentage error.....	61
Table 3.1. Comparison of contact angle between used oils (TPM 10-17) and fresh oil (TPM 3) on a PTFE surface at room temperature.	75
Table 4.1. Summary of the effects of liquid and surface properties on the formation time, lag time, bubble frequency, bubble volumes and heat transfer for vegetable oil data.....	103
Table 5.1. Variables measured using the MBPM and SOA instruments	117
Table 5.2. Physical properties of fluids used for bubble formation experiments.....	118
Table 5.3. Effect of capillary diameter on meniscus dynamics during bubble formation	123
Table 6.1. Effect of coatings on contact angle with vegetable oil	135

LIST OF FIGURES

Fig. 1.1. Stages of heat transfer during frying. (A) and (B) Initial heating and- free convection, (C) Flashing of surface moisture and boiling heat transfer, (D) Falling rate period	18
Fig. 1.2. Archimedean method for measurement of liquid density	22
Fig. 1.3. Brookfield viscometer for measurement of oil viscosity; (A) Brookfield LVDV Viscometer, (B) Thermosel (small volume chamber), (C) Programmable temperature controller, (D) Spindle 18.....	23
Fig. 1.4. Schematic of Pendant-drop technique measurement.....	25
Fig. 1.5. Schematic of sessile drop technique.....	26
Fig. 1.6. Schematic diagram of Wilhelmy plate method	26
Fig. 1.7. Schematic of maximum bubble pressure measurement representing stages of bubble formation. Maximum pressure is measured at stage C	27
Fig. 2.1. Density values of five vegetable oils from room temperature to the smoke point of each oil	47
Fig. 2.2. Surface tension values of five vegetable oils from room temperature to each oil's smoke point determined using a KRÜSS goniometer.....	49
Fig. 2.3. Viscosity values determined for five vegetable oils from room temperature to the smoke point of each oil	51
Fig. 2.4. Comparison between density experimental values of A) Canola oil, and B) Soybean oil and their corresponding predicted values by the modified Racket equation	54
Fig. 2.5. Comparison between surface tension experimental values obtained by KRÜSS goniometer of A) Canola oil, and B) Soybean oil and their corresponding predicted values by the Eötvös equation and the modified Racket- Eötvös equation	57
Fig. 2.6. Comparison between viscosity experimental values of A) Canola oil, and B) Soybean oil and their corresponding predicted values by the modified Andrade equation	60
Fig. 3.1. Assembly for steam delivery for steam-oil and oil-air IFT measurements with the Ramé-Hart Goniometer.....	69
Fig. 3.2. Viscosity as a function of temperature averaged over 3 runs as oil quality is degraded with frying. Samples analyzed were fresh oil (Δ), and used oils collected on day 2 (\times), day 4 (\diamond), day 7 (\square), day 10 (\circ), day 13 ($*$) of the frying cycle	72
Fig. 3.4. Surface tension as a function of time at 22°C for fresh (Δ) and used oil (TPM 12) (\square) averaged over 3 runs in the rising bubble configuration using the Teclis drop-profile device. Air was used for the gas phase.	74
Fig. 3.5. Illustration of stages of drop behavior during measurement of advancing (adding liquid) and receding (withdrawing) contact angles using volume of liquid method adapted from.....	75

- Fig. 3.6.** Contact angle (\diamond) and base diameter (-) of fresh oil at room temperature as a function of step number. Each step denotes increase in drop volume at the rate of $0.25 \mu\text{L}/\text{step}$ for advancing contact angle measurement and decrease in volume at the rate of $0.08 \mu\text{L}/\text{step}$ for receding contact angle measurement. s_m corresponds to the step the when the there is no change in drop base diameter, s_n corresponds to the step change when the base of the drop begins to decrease..... 77
- Fig. 3.7.** Contact angles of fresh (\triangle) and used (TPM 17) ($*$) oil averaged over 3 runs as a function of step number measured at room temperature. 78
- Fig. 4.1.** Submerged orifice assembly to measure bubble dynamics..... 87
- Fig. 4.2.** Stages for image processing to calculate dynamic angle during bubble formation; a) original video, b) axisymmetric binary image, c) cropped bubble region, d) fitting lines to orifice plate and bubble boundaries, e) calculation of included angle 89
- Fig. 4.3.** a) Bubble formation stages represented using fresh oil at room temperature on a 0.75 mm steel orifice, b) Change in bubble height with time and dynamic angle corresponding to bubble formation stages: Stage 1 (S1) - nucleation stage, stage 2 (S2) - growth/ elongation stage, stage 3 (S3) - detachment/ pinch-off stage 93
- Fig. 4.4.** Effect of temperature on a) bubble volume b) bubble formation time, c) bubble frequency and d) formation (t_f) and lag periods (t_l) of subsequent bubbles represented using data for fresh oil on steel surface..... 95
- Fig. 4.5.** Effect of surface wettability on bubble characteristics as demonstrated by a) video clipping of bubble formation on steel and Teflon surfaces, b) formation time and contact angle of oil on steel and Teflon orifices, c) formation and lag periods of subsequent bubbles, d) microscopy image of 0.75 mm steel orifice, e) microscopy image of 0.75 mm Teflon orifice.... 97
- Fig. 4.6.** Effect of oil quality on a) bubble volume b) bubble formation time, c) bubble frequency, and d) formation and lag periods of subsequent bubbles..... 99
- Fig. 4.7.** Effect of orifice size represented using fresh oil on a steel surface a) video snips at the time of bubble pinch-off, b) formation and lag periods of subsequent bubbles, c) bubble formation time using bubble height and change in dynamic angle 101
- Fig. 4.8.** Effect of oil quality on bubble frequency per pore. Represented at $170 \text{ }^\circ\text{C}$ on steel surface for $0.5 \text{ mm} - 1 \text{ mm}$ orifice diameter 103
- Fig. 5.1.** Force balance for a bubble formation from a submerged liquid 108
- Fig. 5.2.** Bubble formation, variation of bubble radius r and pressure within bubble P_b and measuring system P_s during the bubble lifetime (t_b) and deadtime (t_d) for a downward facing capillary. Stages t_{11} , t_{12} , and t_{13} represent stages of meniscus motion during bubble formation time 112
- Fig. 5.3.** Submerged orifice assembly to measure bubble dynamics..... 116
- Fig. 5.4.** Change in pressure during bubble formation and detachment for an upward facing capillary: a) 1 mm capillary b) 3 mm capillary..... 120

- Fig. 5.6.** Video snip of bubble formation in a) water from a 3mm glass capillary, b) 80 % glycerol from a 3 mm glass capillary..... 125
- Fig. 5.7.** Combined effect of surface tension and contact angle ($F_\gamma = \gamma \sin\theta$) on Δ Pressure for 1 mm, 3 mm and 4 mm (\circ , Δ , \square) capillary diameters respectively for bubbles from glass and silanized capillaries..... 126
- Fig. 5.8.** Meniscus entry pattern during bubble formation from 1 mm capillary in a) 8 mM SDS solution from glass capillary, b) 8 mM SDS solution from silanized capillary, c) water from glass capillary, d) water from silanized capillary. Solid arrows (\blackrightarrow) indicate the capillary surface. Dashed arrows (\Rightarrow) indicate the meniscus surface..... 127
- Fig. 5.9.** Necking during bubble pinch-off from 4 mm capillary in a) 8 mM SDS solution from glass capillary, b) 8 mM SDS solution from silanized capillary, c) water from glass capillary, d) water from silanized capillary..... 128
- Fig. 5.10.** Necking during bubble pinch-off from 3mm capillary in a) 8 mM SDS solution from glass capillary, b) 8 mM SDS solution from silanized capillary, c) water from glass capillary, d) water from silanized capillary..... 129
- Fig. 5.11.** Representative image for calculation radii of curvature during necking. R_a is the axial radius. R_r is the radial radius..... 130

LIST OF ABBREVIATIONS

ST- surface tension

IFT- interfacial tension

TPM- total polar materials

CMC- carboxymethyl cellulose

HPMC- hydroxypropylmethyl cellulose

MC- methyl cellulose

Oh- Ohnesorge number

Bo- Bond number

Ca- Capillary number

We- Weber number

Re- Reynolds number

ABSTRACT

Author: Sahasrabudhe, Shreya. PhD

Institution: Purdue University

Degree Received: May 2019

Title: Physical Properties of Food Oils and Factors Affecting Bubble Dynamics During Frying

Committee Chair: Dr. Brian Farkas

Deep fat frying is one of the most complex transport problems in the food industry. According to the US Department of Agriculture, world vegetable oil consumption has increased from 151.68 to 177.16 million metric tons from 2011/12 to 2015/16. Out of the total production, 73.4 % of the oil is used for food purposes; 20 % of which is for shallow and deep fat frying. Frying oil degrades via exposure to heat, oxygen and water, forming volatile and non-volatile products which reduce oil interfacial tension (IFT). The rate of heat transfer, and oil uptake are affected, in part, by physical properties of oil such as density, viscosity and interfacial tension. There is a significant gap in knowledge on the effect of physical properties of oil on heat and mass transfer, especially at high temperatures relevant to the frying process. Hence, the aim of the present research is to understand and mathematically model the effect of temperature and oil quality on oil's physical properties and develop hypotheses to describe the impact on heat and mass transfer during frying.

Oil physical properties including density, viscosity, surface tension and contact angle were measured, and mathematical models were developed to understand the effect of temperature on the physical properties of vegetable oils before and after degradation due to frying. Density and surface tension decreased linearly with temperature; viscosity decreased exponentially. There was no effect of oil quality on viscosity at frying temperatures. Surface tension also remained unaffected by change in oil quality. Contact angle decreased as oil quality degraded with frying indicating increased wettability. When compared with their corresponding experimental values, predicted density values had < 2.0 % error, while predicted surface tension values had < 10.1 % error, and predicted viscosity values had < 12 % error. The error was within the equipment's accuracy range. Thus, the mathematical models presented in this work can be used as a tool to predict the behavior of oils at high temperatures. This will help to gain a better understanding of

oil absorption, as the properties affecting heat and mass transfer rates during frying may be accurately predicted at frying temperatures.

Heat is transferred by convection from the hot oil to the food surface and by conduction from the surface of food to the core. The food material acts as a vapor generating matrix resulting in the formation of bubbles in hot oil at the food's surface. The heat transfer coefficient during frying shows a bell-shaped curve; reaching its peak value at a high rate of moisture loss when bubbling is observed. Thus, the rate of heat transfer is dependent on bubbling characteristics. Hence, a customized assembly was built to understand how oil physical properties as well as process parameters such as oil temperature affect bubble formation during frying with an aim of understanding the effect of oil quality on heat transfer. A separate assembly was built to understand oil absorption during the immersion frying stage by understanding the effect of liquid properties and liquid-solid interaction on meniscus formation between consecutive bubbles when the orifice is submerged in the fluid. The research found that oil wettability increased due to degradation during frying. Increased wettability resulted in the formation of smaller bubbles at a higher frequency with used oil and is proposed as a mechanism for increased heat transfer with degraded oil reported in literature. The study also was found that oil enters capillaries during the lag time between bubbles and adheres to the pore walls when liquid surface tension is low and for liquids that wet the capillary surface. The depth of entry and the pattern of meniscus oscillation is dependent on the capillary diameter, wettability of the capillary and liquid surface tension. Thus, the rate of heat transfer as well as oil absorption during immersion frying stage are dependent on fluid surface tension and wettability between the oil and the food surface.

1. INTRODUCTION

1.1. Frying process

Deep-fat frying imparts a unique flavor and texture to foods and is one of the most important methods of food preparation widely used by both the food industry and consumers (Orthoefer and List, 2007a). Frying involves submerging a food in extremely hot oil at a temperature above the boiling point of water for a given period until the food reaches a safe minimum internal temperature resulting in a product with a crisp exterior (crust) and moist interior (core) (Bouchon, 2009; Farkas et al., 1996a; USDA/FSIS, 2013). Frying involves simultaneous heat and mass transfer at the surface of the food resulting in oil uptake by the food and loss of water and some soluble material from the product. The presence of heat and moisture are responsible for the organoleptic properties of food such as flavor, texture, and characteristic golden-brown color (Bouchon and Pyle, 2005). As per USDA/FSIS (2013) guidelines, when the food is deep-fried properly, it is hot and crispy on the outside and cooked safely at the center.

1.1.1. Physical and chemical changes during frying

The main chemical reactions involved in this process are change in color, taste, and flavor due to Maillard reactions and caramelization, starch gelatinization, protein denaturation, inactivation of enzymes, and flavor development (Bordin et al., 2013; Choe and Min, 2007; Ziaifar et al., 2008). The physical changes occurring in the process are softening of tissue, decrease in moisture content, increase in oil content, formation of crust and shrinkage/swelling of the product resulting in texture development (Patterson et al., 2004). The presence of heat and moisture during frying also impacts oil quality due to hydrolysis, oxidation and polymerization of oil (Choe and Min, 2007). Factors affecting heat and mass transfer during frying can be divided in three main categories (Bouchon, 2009; Dana and Saguy, 2006; Moreira et al., 1997) as listed below and described in section 1.3:

- Process parameters- oil temperature and frying time
- Oil properties- viscosity, density, heat transfer coefficient, surface/ interfacial tension, oxidation, polymerization, hydrolysis
- Product characteristics- Moisture content (water loss), porosity (pore development and pore size distribution), surface roughness, shape, size, orientation of product

1.1.2. Frying and health impact

Fried foods comprise of a wide variety of products such as potato, tortilla, and banana chips; french fries, donuts, and battered products such as fried chicken and fish fingers. The oil content in these products varies from 15 – 40 % of product weight depending on the type of food (Bouchon, 2009; Dana and Saguy, 2006). Studies have shown that consumption of high amounts of fat is a contributor to coronary heart diseases, diabetes, cancer and hypertension. The current consumer trends are towards consumption of healthier snacking options, without compromising the flavor and taste of food (Mintel Survey, 2017). Hence it is important to develop techniques to reduce oil absorption during frying while maintaining the texture and flavor of the product.

1.2. Mechanisms for heat and mass transfer during deep-fat frying

Frying is a complex process due to the coupled heat and mass transfer phenomena. During frying, moisture leaves the product in the form of vapor and oil enters the food.

1.2.1. Heat transfer during immersion frying

Heat is transferred from the oil to the food surface (crust) by convection, and from the crust to the interior (core) of food by conduction (Costa et al., 1999; Farkas et al., 1996a; Farkas and Hubbard, 2000; Hubbard and Farkas, 1999). These two regions are defined by the liquid vapor interface formed in the food product due to evaporation (Farkas et al., 1996b; Hubbard and Farkas, 1999). During frying, initially the food surface temperature rises to the boiling point of water resulting in water evaporation. The food surface remains at this temperature until all surface water is evaporated and a crust is formed (Farkas and Hubbard, 2000; Hubbard and Farkas, 1999). As frying progresses, surface temperature approaches oil temperature, and the core temperature approaches water boiling temperature (Hubbard and Farkas, 1999). According to Farkas et al. (1996) and Farid and Chen (1998), heat transfer during frying can be broken down into four stages (Fig. 1.1), (A) Sensible heating period: During this stage, the surface of the product is heated up to the boiling temperature of water and negligible water evaporation occurs. At this stage, heat is transferred from oil to the food material by convection at the surface and conduction through the solid. (B) Initial water evaporation period: During this stage, the heat transfer mechanism changes from natural convection to boiling heat transfer due to the vigorous escape of water vapor, and a thin layer of crust is formed. (C) Evaporation period: During this period, bulk of the water is lost,

the evaporation front propagates towards the interior causing the core temperatures to rise to the boiling point of water. This is the falling rate stage during which crust thickens and there is steady decrease in the rate of mass transfer from the sample. (D) Bubble end point: It is the final stage of frying and describes the apparent cessation of water loss from the food. A major part of heat transfer process is marked by vaporization of water, resulting in bubble formation and detachment at the food surface (Costa et al., 1999; Hubbard and Farkas, 1999; Safari et al., 2018). Thus, the characteristic properties associated with a fried product are a result of the high temperature and heat flux found during the boiling phase of frying (Sandhu et al., 2013).

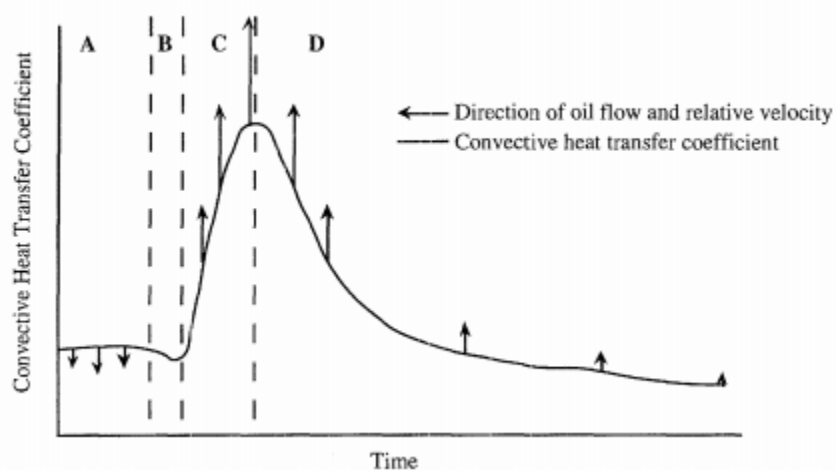


Fig. 1.1. Stages of heat transfer during frying. (A) and (B) Initial heating and- free convection, (C) Flashing of surface moisture and boiling heat transfer, (D) Falling rate period (Farkas and Hubbard, 2000)

1.2.2. Oil absorption during immersion frying and post-frying cooling

During frying, the water in the crust evaporates first. The liquid then migrates from the core to the crust so that frying process continues. This removal of water when combined with associated puffing due to vapor formation creates voids which are then replaced by fat (Mellema, 2003). The absorption of oil into the product during frying can be characterized into three classes depending on the stage in which it enters the product (Bouchon et al., 2003): (1) structural oil is absorbed during frying, a very small portion of the oil enters food at this stage because water evaporation from the porous structure prevents oil uptake, (2) penetrated surface oil is suctioned in during the cooling stage of frying. Most of the oil absorption occurs during this stage, and (3) surface oil is the fraction which remains on the surface of the product after frying and can enter

the product depending on drainage characteristics of the oil (Bouchon and Pyle, 2005). Studies by Bouchon and Pyle (2005) and Mellema (2003) have found that about 20 % of total oil content is absorbed during immersion stage, 51.2 % is absorbed during post-frying cooling and about 28 % remains as surface oil on the food product.

Bouchon and Pyle (2005); Dana and Saguy (2006); and Mellema (2003) proposed two main mechanisms for oil uptake during frying: due to loss of moisture from the food and capillary pressure and due to vapor condensation in the cooling stage.

1.2.2.1. Capillary mechanism

Dana and Saguy (2006) proposed that oil replaces the water that has evaporated during frying. Moisture escape in the form of steam when the product temperature reaches above 100° C, creating a positive pressure gradient and forming cracks, crevices and voids which can be considered as capillary pathways through which oil can enter (Dana and Saguy, 2006; Ziaifar et al., 2008). Oil that enters helps maintain structural integrity by preventing shrinkage and collapse. Uptake of oil by capillary mechanism depends on the surface tension at the oil/vapor and oil/food interface (Mellema, 2003). Moreira et al. (1997) also proposed that oil uptake is caused by capillary forces created due to steam escape (Eq. 1.1).

$$P_g - P_{atm} = \frac{(2\gamma\cos\theta)}{r} \quad \text{Eq. 1.1}$$

where P is the pressure (Pa), γ is surface tension (N/m), θ is the angle (rad), ρ is density (kg/m³), g is gravity in x-direction (m²/s), h is penetration distance (m).

1.2.2.2. Condensation mechanism

About 20 % of oil is absorbed during frying, however about 80 % remains on the product when the food is taken out of the fryer (Moreira et al., 1997). Oil can then drain off, be absorbed into the porous crust or remain on the surface of the product (Bouchon and Pyle, 2005). Condensation mechanism is the most important for short frying times and large food samples (Mellema, 2003). The viscosity of the oil, porosity and surface of the product are the main mechanisms that control the rate of this process. During frying, moisture continuously escapes from food, creating overpressure inside the food. When the product is taken out of the fryer, the temperature drops and the vapor in the crust condensates. Thus, the pressure inside the crust is

lower than surrounding. This causes oil to enter the food due to a ‘vacuum effect’ as described by Dana and Saguy (2006).

Thus, most of the oil is absorbed by fried food after the product is taken out of the fryer and cooled. Condensation mechanism is responsible for most of the oil absorbed in frying. Bouchon et al., 2005 proposed a pressure-based model (Eq. 1.2) for oil uptake in food during the post-frying cooling stage. Thus, oil enters the food if the vapor pressure is low enough to create a positive pressure driving force.

$$Q = \frac{\pi r^4 (P_{\text{atm}} - P_v + \frac{2\gamma \cos\theta}{r}) \pm \rho g h \cos\alpha}{8\mu h} \quad \text{Eq. 1.2}$$

where Q is the volumetric flow rate (m³/s), r is radius (m), P is pressure (Pa), γ is the surface tension (N/m), θ is the contact angle (rad), ρ is the density (kg/m³), h is the height of oil film, α angle (rad), μ is the viscosity (Pa. s).

1.3. Factors affecting oil absorption during deep-fat frying

Oil uptake is a major concern due to its negative health impact. However, oil in the product is necessary to obtain the desired crispiness of fried food. Oil enters the food material from the surface to the core. Oil absorption mainly occurs during the cooling stage and is a balance between adhesion forces (capillarity due to vapor condensation) and drainage of oil from the product surface (Ufheil and Escher, 1996). Several factors have been reported to affect oil uptake during frying including: oil type and quality (composition and degradation), surface tension and interfacial tension, temperature and time of frying, initial and final moisture content of the product, crust structure (porosity and surface roughness), product shape, product orientation, and pre- and post-frying treatments (Bouchon and Pyle, 2005; Bouchon, 2009; Moreira et al., 1997).

1.3.1. Effect of oil quality (properties) on oil absorption

Frying oil quality affects oil absorption and the types of by-products and residues absorbed by food (Orthoefer and List, 2007b). Vegetable oils such as soybean, canola, corn, palm, peanut, olive, sunflower and safflower are commonly used for frying (USDA/FSIS, 2013). Selection of oil for frying depends on product to be fried, desired texture, flavor and eating characteristics for the product, design of fryer, rate of oil turnover, cost, shelf life requirements, and historical usage (Orthoefer and List, 2007b). During initial stages of frying, the oil has a bland flavor, hence it can

dilute the taste of the fried food. As frying progresses, the oil carries and supports the full, rich flavor and aroma of the product and thus enhances the sensory appeal of the food (Banks, 2007). Frying oil also imparts other important eating characteristics, including lubricity, mouth feel, flavor release, and a rich-eating quality to the food (Banks, 2007). Hence, understanding the impact of oil quality on fried food characteristics is very important. Change in oil quality during frying is responsible for increased heat transfer and change in rate of oil absorption as oil degrades. Oil undergoes chemical changes such as oxidation, hydrolysis and polymerization during the frying process. The main physical parameters of oil that are affected are the density, viscosity, surface tension and wettability with the food surface. It is important to understand the impact of these physical parameters on oil quality and how they are measured to develop a deeper knowledge of the effect of these parameters on heat and mass transfer during frying.

1.3.1.1. Density

Kalogianni et al. (2011); Nouredini et al. (1992) and Tseng et al. (1996) have reported increase in oil density with decrease in oil quality due to usage for frying. Formation of polymers due to oil oxidation, polymerization, hydrolysis and isomerization are responsible for increase in oil density (Tseng et al., 1996). Density decreases linearly with increase in temperature. Hence it is important to measure density at frying temperatures to understand impact of oil quality on density.

Oil density at high temperatures can be determined using the Archimedean method (Fig. 1.2) which has been traditionally used to determine the volume of irregularly shaped objects (White, 1959). For measurement of liquid density, a container with test liquid is placed on an electronic balance and a probe is suspended in the liquid. If the volume of the probe is known, the density of liquid is given by the difference between the balance reading before and after immersion of the probe divided by the volume of the probe (Eq. 1.3) (Hughes, 2006).

$$\rho = \frac{\beta + s}{V^0 + v'} \quad \text{Eq. 1.3}$$

where β is buoyancy, V^0 is volume of the reference object, s is surface tension between the liquid and the wire, v' is volume of immersed wire.

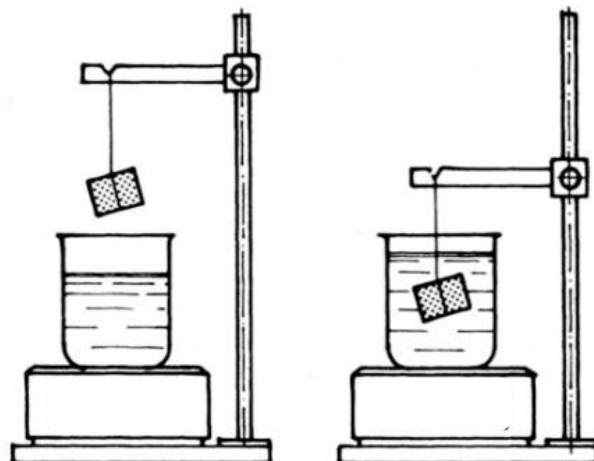


Fig. 1.2. Archimedean method for measurement of liquid density

1.3.1.2. Viscosity

Studies have shown that viscosity of oil increases due to formation of high molecular weight compounds such as dimers and trimers as oil degrades with continuous use in frying (Abidi and Warner, 2001; Kalogianni et al., 2011; Miller et al., 1994). Food fried in oil with a high viscosity tends to absorb more oil making it soggy, greasy, and less appetizing (Orthofer and List, 2007b). However, viscosity of oil is dependent on temperature, hence measurements should be made at frying temperatures to obtain an accurate estimate of the effect of oil quality on viscosity. Ziaifar et al., 2008 reported that viscosity of the oil is the main factor which governs drainage during post-frying cooling. When the food material is removed from frying oil, it drags a film of oil which can be modelled using Landau-Levich-Derjaguin relation (Eq. 1.4), which is dependent on liquid viscosity.

$$H = 0.94 \frac{\mu U^{2/3}}{\gamma^{1/6}(\rho g)^{1/2}} \quad \text{Eq 1.4}$$

where H is the oil film thickness, μ is the oil viscosity (Pa·s), γ its surface tension (N/m), U the speed of removal (m/s), ρ the oil density (kg/m^3), and g the gravity acceleration (m/s^2).

Viscometer is used to measure the dynamic viscosity (μ) of liquids (Fig. 1.3). Viscometer measures the torque required to rotate a spindle inside the fluid which is directly proportional to fluid viscosity (Rao, 2007). To measure the viscosity at high temperatures, a temperature ramp profile can be created using a thermosel and attached temperature controller.



Fig. 1.3. Brookfield viscometer for measurement of oil viscosity; (A) Brookfield LVDV Viscometer, (B) Thermosel (small volume chamber), (C) Programmable temperature controller, (D) Spindle 18

1.3.1.3. Surface tension

Surface and interfacial tension govern heat transfer during frying and oil uptake by capillary mechanism as the frying oil moves through pores in the food filled with water/ steam. As the frying process progresses, the oil degrades leading to the formation of many monoglycerides, diglycerides, free fatty acids and glycerol. These act as emulsifiers and can increase the foaming capacity of oil, thus forming large steam bubbles which result in increased oil absorption (Dana and Saguy, 2006). They can also reduce the interfacial tension between oil and food (Blumenthal and Stier, 1991), thus affecting heat and mass transfer rates of oil into the product (Farkas and Hubbard, 2000). Formation of these surface-active agents as oil degrades during frying is proposed as a mechanism for increased oil absorption with decrease in oil quality. Wettability is known to influence oil uptake and can be measured by measuring contact angle between the food and oil. Contact angle which is a measure of wettability between a liquid and a solid mainly governs the drainage properties of oil after frying which in-turn affects the oil uptake by the food (Aydar et al., 2016; Bouchon and Pyle, 2005). The relation between contact angle, surface tension of liquid, interfacial tension between liquid and solid and the surface energy of the solid is given by the Young's equation (Eq. 1.5).

$$\gamma^{sv} = \gamma^{sl} + \gamma^{lv} \cos\theta \quad \text{Eq. 1.5}$$

where γ^{sv} is the solid/liquid interfacial free energy (N/m), γ^{sl} is the solid surface free energy (N/m), γ^{lv} is the liquid surface free energy (N/m) and θ is the contact angle (rad).

Surface tension is known to decrease with increase in temperature based on Eötvös equation (Eq. 1.6). Aydar et al. (2016) conducted a study to measure surface tension properties of food oils on PTFE at high temperatures using sessile drop technique in the presence of steam and air as the surrounding media. The study found linear decrease in contact angle with temperature increase, which can be predicted according to the Girifalco-Good-Fowkes-Young equation (Eq. 1.7).

$$\gamma_{LG} V^{2/3} = K_E (T_c - T) \quad \text{Eq. 1.6}$$

$$\cos\theta = -1 + 2 \sqrt{\gamma_{LG} \left(\frac{M}{\rho}\right)^{2/3} / K_E (T_c - T)} \quad \text{Eq. 1.7}$$

where γ_{LG} is the liquid-gas surface tension (N/m), V is the molar volume, K_E is the Eötvös constant, T_c is the liquid critical temperature ($^{\circ}\text{C}$), and T is the sample temperature ($^{\circ}\text{C}$), θ is the contact angle (rad), M is the liquid molar mass (kg), ρ is the liquid density (kg/m^3).

Moreira et al. (1997) stated that surface tension decreases with increasing temperature, resulting in a capillary pressure reduction. This contributes to limiting oil uptake during frying. Kalogianni et al. (2011) found no effect of oil quality on surface tension when measured at 50°C after numerous frying cycles. However, in-order to conclusively predict the effect of surface tension on frying heat and mass transfer, it should be measured at high temperatures of the frying process. Experimental quantification of the impact of surface tension on food characteristics has proved challenging. This is not only because of the complexity of the various processes described above, but also due a surprising dearth of information on surface (lipid-air) tension properties of food lipids. Pendant drop, Rising bubble, Sessile drop, Wilhelmy plate and Maximum bubble pressure are some of the important techniques used to measure surface tension of liquids (Drelich et al., 2002).

1.3.1.3.1. Pendant drop

A measured volume of test fluid is suspended as a drop from a capillary needle of known dimensions (Fig. 1.4). There is an increased pressure inside the drop due to the interfacial tension

between the inner and outer phase. Shape of the drop is thus related to volume, density and surface tension of the liquid. Surface tension is calculated using pressure difference and drop radius based on Young-Laplace equation (Eq. 1.8).

$$\Delta P = \gamma \left(\frac{1}{r_1} + \frac{1}{r_2} \right) \quad \text{Eq. 1.8}$$

where ΔP is the pressure difference between the inner and outer phase (Pa), γ is the liquid surface tension (N/m), r_1 and r_2 are the radii of curvature (m).

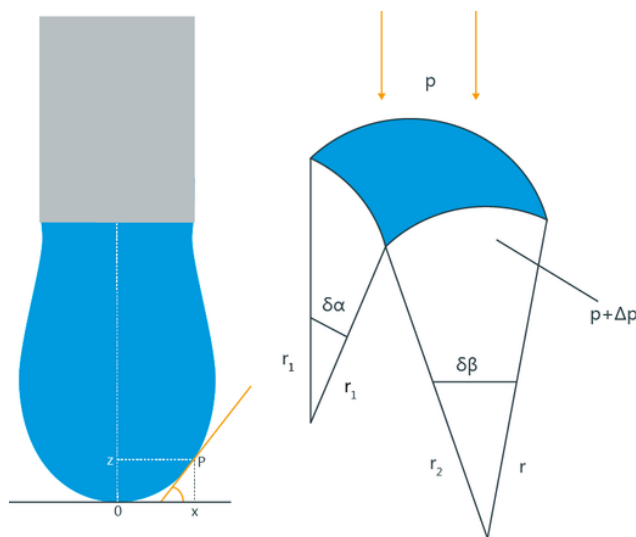


Fig.. 1.4. Schematic of Pendant-drop technique measurement (Pendant drop, 2018)

1.3.1.3.2. Sessile drop

When a drop is dispensed on a solid surface, it forms an angle with the surface based on three forces (solid/liquid interfacial free energy (γ^{sv}), solid surface free energy (γ^{sl}), liquid surface free energy (γ^{lv})) (Fig. 1.5) (Karbowski et al., 2006). When the free energy of solid and liquid are known, the shape of the drop can be used to calculate the solid-liquid interfacial energy. The contact angle value indicates hydrophilicity ($\theta < 90^\circ$) and hydrophobicity ($\theta > 90^\circ$) of the surface. The surface is wettable when $\theta < 90^\circ$ and non-wettable when $\theta > 90^\circ$. Goniometer is typically used to measure the contact angle by sessile drop technique. For this method, a drop of known volume is dispensed on a solid surface, the contact angle is then measured by inscribing tangents at the triple contact point between the liquid, solid and air, and calculating surface tension based on the shape and size of the drop using Young equation (Eq. 1.5).

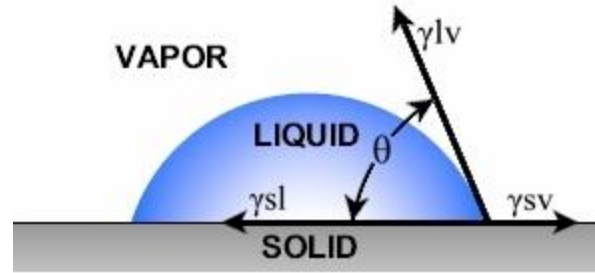


Fig. 1.5. Schematic of sessile drop technique (ramé-hart Contact Angle, 2018)

1.3.1.3.3. Wilhelmy plate

A thin vertical plate made from roughened platinum-iridium alloy or platinum is used for this technique (Drelich et al., 2002). A plate of known perimeter is attached to a balance, and the vertical force acting on the plate due to the liquid meniscus is measured (Fig. 1.6). When plate is in contact with the liquid, this force relates to surface tension and contact angle (Eq. 1.9).

$$\gamma = \frac{F}{2L\cos\theta} \quad \text{Eq. 1.9}$$

where γ is the surface tension (N/m), F is the force acting on the plate (N), L is the wetted length (m), θ is the contact angle between the liquid and the plate (rad).

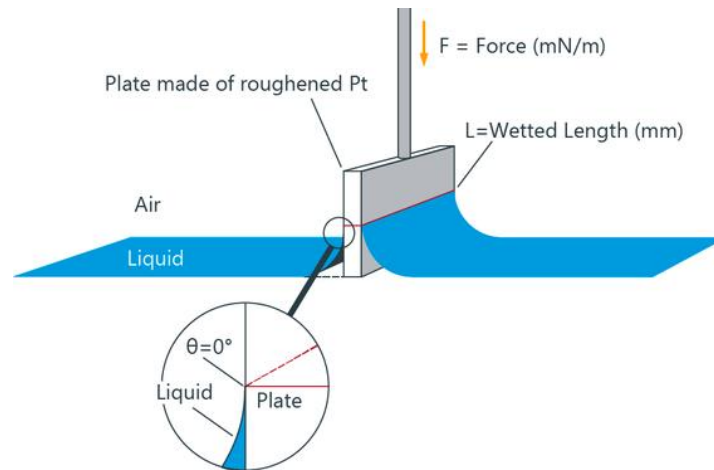


Fig. 1.6. Schematic diagram of Wilhelmy plate method (Wilhelmy plate method, 2018)

1.3.1.3.4. Maximum bubble pressure

A tensiometer is used to create bubbles at a constant rate from a capillary submerged in liquid to calculate the dynamic surface tension of the liquid. Bubble grows due to Laplace pressure across surface. The pressure in the bubble continues to increase until it obtains a hemispherical shape. Pressure inside the bubble attains maximum value when the bubble radius equals the capillary radius (Fig. 1.7) (Dukhin et al., 1996). The maximum pressure can be related to the liquid surface tension using Laplace equation (Eq. 1.10).

$$\gamma = \frac{\Delta P_{max} r}{2} \quad \text{Eq. 1.10}$$

where γ is the liquid surface tension (N/m), ΔP_{max} is the maximum bubble pressure (Pa), and r is the capillary radius (m).

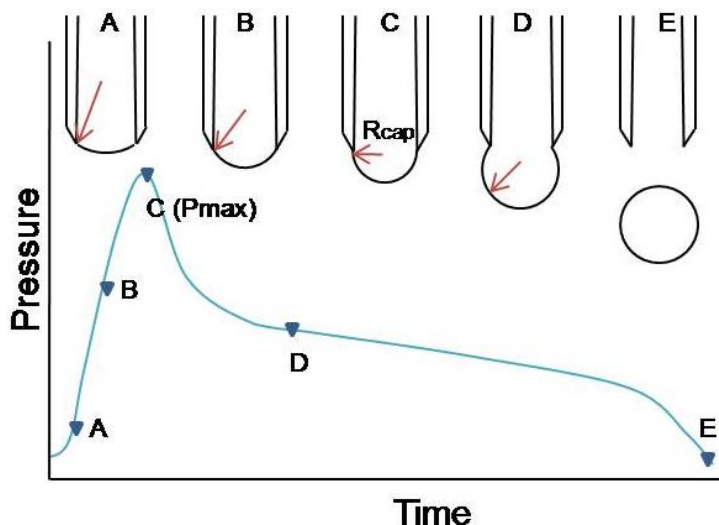


Fig.. 1.7. Schematic of maximum bubble pressure measurement representing stages of bubble formation. Maximum pressure is measured at stage C (Dukhin et al., 1996)

1.3.2. Effect of product properties on oil absorption

1.3.2.1. Moisture content

Oil uptake during frying is directly proportional to the amount of water lost during frying as oil fills the voids created by escaping steam (Bouchon, 2009). Hence, the water vapor transport rate as well as oil uptake rate can be expressed in terms of diffusion. Higher moisture content in

the food leads to higher pressure buildup during the immersion frying stage and correspondingly a higher pressure drop, thus increasing the driving force for oil absorption (Sandhu et al., 2013).

1.3.2.2. Product shape, size, porosity and roughness

Majority of oil absorption occurs during the post-frying cooling stage. Thus, oil uptake is a surface phenomenon which involves a competition between oil drainage and suction into food pores (Cortés et al., 2016). Studies by Gamble and Rice (1988) have shown linear relationship between surface area and oil uptake. Increase in surface area due to cutting of products increases the surface roughness of the product thus increasing oil uptake (Ziaififar et al., 2008). Cortés et al. (2016) found higher porosity and larger pore sizes facilitate faster removal of moisture from the food in the immersion stage and a higher rate of oil absorption during the cooling stage. Thanatuksorn et al. (2007) found that pore structure and pore size distribution are directly proportional to oil uptake. Small pores cause higher capillary pressures, resulting a higher oil content (Moreira et al., 1997). Moreno et al. (2010) conducted a study with potato flakes and gluten-based products and found that there was a linear relationship between roughness and amount of oil absorbed when products of the same composition were compared. The study concluded that surface roughness is an important factor affecting oil absorption, but the total amount of oil absorbed is a function of product microstructure, surface wetting and food composition.

1.3.3. Effect of process parameters: Frying oil temperature and frying time

Frying time and temperature are inversely related to each other. Higher temperature for frying products results in lower time for which frying is conducted. However, no direct correlation has been found between time and temperature for frying and oil uptake (Gamble et al., 1987). Bouchon et al. (2003) and Bansal et al. (2014) found that oil absorption during frying is a temperature-independent function for shorter frying times. For longer frying times, they found that oil content of potato cylinders fried at 155 °C was significantly lower than those fried at 170 and 185 °C, but no difference was found between the two higher temperatures. However, the study concluded that lower oil uptake observed at lower temperatures was related to lower moisture loss. Higher temperatures result in higher moisture loss when a product is fried for the same amount of time. Thus, temperature does not directly impact the amount of oil absorbed but influences the moisture content in the food (Krokida et al., 2000; Moreira et al., 1997; Sandhu et al., 2013). For

thin products such as crackers and chips, most of the water evaporates by 20-40 s. Frying the product beyond this time results in increased oil uptake as oil starts entering the product once the water content is low (Bansal et al., 2014; Moreira et al., 1997).

To develop strategies for reduction of oil absorption, it is important to understand the mechanism of oil uptake and the factors governing it. Previous work by Farkas et al. (1996a) and Bouchon and Pyle (2005) have modelled the frying process and explained that most of the oil uptake occurs during the cooling period after frying. Drainage of oil from the surface, viscosity, interfacial tension during cooling and the porosity of the surface are thus some of the most important factors that control oil absorption.

1.4. Studies on techniques for oil absorption reduction

Oil uptake reduction methods can be divided into pre and post frying treatments, modification of the frying medium and modified frying methods (Thanatuksorn et al., 2007).

1.4.1. Pre-frying treatment techniques

Pre-frying treatments aim to reduce oil absorption by reduction of surface permeability. Dehydration using freeze drying, hot-air drying, or osmotic drying are the most common pre-treatments proposed for oil uptake reduction. Studies on pre-treatments have aimed at reducing the oil absorption by reduction in moisture content of product before frying. Osmotic dehydration using sucrose, salt or maltodextrin solutions have reported a decrease in oil content up to 60 % depending on the type of solution used (Krokida et al., 2001). Pedreschi and Moyano (2005) studied the effect of blanching and predrying potato slices prior to frying on oil uptake during frying. The study observed that blanched and blanched-dried potato slices had less oil uptake when the product moisture content was <10 g/100 g (wet basis). When the product moisture content was < 20 g/100 g (wet basis), only blanching led to increase in final oil uptake. Blanched-dried slices however, had a lower oil uptake compared to the slices with no pre-treatment. The study proposed gelatinization of surface starch as a mechanism of oil reduction when the product was blanched, and reduction of initial moisture as the mechanism of oil reduction when the product was pre-dried. Moreno and Bouchon (2008) studied the effect of pre-drying (freeze drying, air drying and osmotic treatment) on frying of potato chips and found that freeze drying increased oil absorption mainly due to increase in porosity of the surface whereas air drying caused shrinkage of the external pores

leading to decrease in oil absorption. The study found no effect of osmotic treatment on oil absorption or increased oil uptake with osmosis in some cases. Thus, the study concluded that effect of pre-treatments on oil uptake is associated with structural changes occurring at the surface of the piece which reduce surface permeability rather than with reduction in moisture before frying.

1.4.2. Modification of frying methods

Dueik and Bouchon (2011) studied the use of vacuum frying for novel snacks vacuum frying led to 51, 57 and 22 % decrease in oil absorption for carrots, potatoes and apple chips respectively when the same thermal driving force ($\Delta T = T_{oil} - T_{water}$) of 60 °C was used. For vacuum frying, $\Delta T = 60$ °C was achieved at oil temperature of 98 °C since the vessel was pressurized. For atmospheric frying, the oil temperature was 160 °C. The study attributed decrease in oil content in vacuum frying to the lower vapor pressure of water during vacuum frying and lower temperatures reached during the process. Maity et al. (2014) used vacuum frying to study quality attributes of jackfruit and found that low boiling temperature of water due to vacuum helped to retain all the sensory attributes and bio-actives in jackfruit and resulted in a product with less oil content and higher quality.

Radiation frying is another technique proposed to reduce oil uptake and it eliminates the immersion of product in oil. In radiant frying systems, powerful halogen emitters are positioned to generate a heat flux which is comparable to the frying process (Thanatuksorn et al., 2007). Nelson et al. (2013) studied the effect of use of radiant frying for frozen chicken patties and potato cakes. Use of radiant frying showed 37-38 % reduction in oil uptake compared to immersion frying. Kaczay (2016) found 52.3 % reduction in oil content of hash-browns when fried using radiation frying compared to immersion frying. Sensory evaluation of the two techniques showed that the immersion fried product scored significantly higher on appearance, aroma, flavor, and texture attributes, while radiant fried product scored higher on the oiliness attribute.

Janositz et al. (2011) studied the effect of Pulsed electric field (PEF) processing on potato slices and found that PEF pre-treated samples had 39 % less oil uptake due to diffusion. PEF process caused permeabilization of cell membranes within the potato, which allowed for greater diffusion of water from the core to the surface, resulting in a thicker water vapor layer at the surface which prevented oil penetration. Ignat et al. (2015) also reported decrease in oil absorption for potatoes treated with 18.9kJ/kg PEF compared to blanched and water-dipped samples. The effect

of PEF was attributed to the structural modification of potato tissue due to electroporation. However, increased permeability with PEF could lead to increased porosity of the crust layer thus increasing oil absorption after frying, as proposed by Bouchon et al. (2003).

1.4.3. Use of barrier layers/ coatings

Edible films are used in fried products to provide protection during cold storage before frying, control of water losses during frying, and stability against wilting and/or loss of crispness under infrared lamps between frying and serving (Ajo, 2017). Use of edible coatings to reduce oil uptake during frying has been studied extensively for a variety of food products. Properties of coatings in relation to fat uptake are low moisture content, low moisture permeability, thermogelling or crosslinking (Moreira et al., 1997). The principal factor considered to have a major impact on oil uptake is moisture loss. The outer layer of the food needs to have low moisture content, which can be achieved by applying a low-moisture level coating. Hydrophilic biopolymers mainly from polysaccharides can be used as water binders in a coating to reduce water loss from the coat, thus reducing oil uptake (Pinthus et al., 1993). However, the exact mechanism behind these coatings has not yet been explained.

García et al. (2002) studied the use of methyl cellulose (MC) and hydroxypropylmethyl cellulose (HPMC) with or without plasticizer to reduce oil uptake in fried products. The mechanism proposed in this study was that cellulose derivatives reduce oil absorption through film formation at temperatures above their gelation temperature of around 60° C. Use of plasticizer was necessary to retain the integrity of the coating. They observed that in potato strips coated with MC and 0.5 % sorbitol, oil absorption decreased by 40.6 % and moisture retention increased by 6.3 % compared to control samples. Also, sensory analysis showed non-significant differences between samples coated with MC and sorbitol and the uncoated controls. Mallikarjunan et al. (1997) studied the use of corn zein (CZ), HPMC or MC film-forming solutions on mashed potato balls as food model systems. They observed a reduction of 14.9 %, 21.9 % and 31.1 % in moisture loss and a reduction of 59.0 %, 61.4 % and 83.6 % in fat uptake for samples coated with CZ, HPMC and MC films, respectively. The study proposed that MC and HPMC form a coating due to thermal gelation above 60°C which is responsible for controlling the transfer of moisture and oil between the product and the frying medium. Zein on the other hand, forms a film using the moisture on the product surface. The hydrophobic amino acids in zein are responsible for creating a moisture barrier. The study concluded that irrespective of the type of coating, the edible films reduce

moisture loss and fat uptake during frying. Dragich and Krochta (2010) studied the use of whey protein as a coating for fat-uptake reduction in fried chicken. The experiments showed that coating chicken with a wheat flour/batter/wheat flour/10 % denatured whey protein isolate (DWPI) film combination resulted in 27-37 % fat reduction in the product. The authors proposed DWPI film modifies the surface structure of the product by filling pores in the surface of the product which would otherwise provide a route for oil absorption. Also, the high moisture content of DWPI films increases surface tension of oil, thus reducing fat uptake. Usawakesmanee et al. (2005) studied the effect of incorporation of HPMC, MC and wheat gluten in the pre-dusting mix of fried breaded potato batter so that they form edible coatings. They found that HPMC and MC reduced the fat absorption more than gluten. Sensory evaluation showed no difference in acceptability for products with coating when compared to the control. However, no mechanisms for the reduction of fat absorption by the coatings were proposed.

Thus, different studies on use of coatings for reduction of oil absorption are product specific. Some studies suggest the use of proteins like zein and gluten to be superior as coating matrices whereas others suggest cellulose derivatives to be superior. The studies propose that the mechanism of oil reduction for the coatings is based on altering the water-holding capacity of a variety of fried foods by trapping moisture inside and preventing the replacement of water by oil. However, during frying, the product continuously loses moisture during the immersion stage. Furthermore, the reduction in moisture loss is not comparable with the oil absorption reduction observed with the use of coatings. Hence, to understand the mechanism of oil reduction for these coatings further studies need to be conducted.

Several studies have hypothesized on the mechanisms of fat reduction, but ambiguities remain, and more research needs to be done, particularly in understanding surface phenomena. From their effect on emulsion stability and associated sensorial attributes, to control of droplet/bubble size and attendant heat transfer rates, surface and interfacial tension play an active role in determining physical attributes, chemical interactions, microbial presence and activity in foods (Bouchon, 2009). Immersion frying is one of the most complex transport problems in the food industry. Heat transfer to the food surface and oil migration into the food both depend on the time-dependent movement of interfaces either oil-vapor or oil-water at very high temperatures (Farkas et al., 1996a). Heat transfer coefficient is largely determined by the rate of growth of steam bubbles that form at the food/oil surface (Farkas and Hubbard, 2000). The rate of bubble growth

is controlled by the oil-vapor surface tension at the bubble interface. A decrease in surface tension, by making it energetically easier to form each bubble, therefore causes an increase in heat flux at the surface. At the same time, oil viscosity increases as oils degrade, and an increase in viscosity will decrease heat flux at the surface. Bouchon et al. (2005) proposed to quantify oil uptake due to steam condensation by recognizing that it involves two mechanisms. One is adherence of the oil to the food as the oil drains gravitationally, giving a surface film which depends inversely on surface tension. The second mechanism is the imbibing of oil by the food, in which the flow rate into the food is driven by capillary action, which is proportional to surface tension, and by the pressure differential created via condensing steam. Understanding what drives this oil transport such that it may be reduced is a prime goal in fried foods research, with an aim to improve the healthfulness of fried products. Investigation of surface and interfacial tensions at high temperature is a key needed element in meeting this goal. From this analysis it can be seen that relative to heat flux during frying, viscosity and interfacial tension work against one another as oils degrade. While the effect of oil quality on density and viscosity at high temperature has received considerable attention, the tension of oils at frying temperatures in pure or mixed systems has not been studied extensively (O'Meara, 2012). How these properties interplay in heat and mass transfer as oil degrades with use in frying needs to be quantified. The current proposal study to address this gap.

1.5. References

- Abidi, S.L., Warner, K. (2001). Molecular-weight distributions of degradation products in selected frying oils. *Journal of American Oil Chemists' Society*, 78, 763–769.
- Ajo, R. Y. (2017). Application of hydrocolloids as coating films to reduce oil absorption in fried potato chip-based pellets. *Pakistan Journal of Nutrition*, 16 (10), 805-812.
- Aydar, A., Rodriguez-Martinez, V., Farkas, B. (2016). Determination and modeling of contact angle of Canola oil and olive oil on a PTFE surface at elevated temperatures using air or steam as surrounding media. *LWT- Food Science and Technology*, 65, 304–310.
- Banks, D. (2007). 14 - Industrial frying, in: Erickson, M.D. (Ed.), *Deep Frying (Second Edition)*. AOCS Press, pp. 291–304.
- Bansal, H.S., Takhar, P.S., Maneerote, J. (2014). Modeling multiscale transport mechanisms, phase changes and thermomechanics during frying. *Food Research International*, 62, 709–717.

- Blumenthal, M.M., Stier, R.F. (1991). Optimization of deep-fat frying operations. *Trends Food Science Technology*, 2, 144–148.
- Bordin, K., Kunitake, M.T., Aracava, K.K., Trindade, C.S.F. (2013). Changes in food caused by deep fat frying—a review. *Arch. Latinoam. Nutrition* 63.
- Bouchon, P. (2009). Understanding oil absorption during deep-fat frying. *Advances Food Nutrition Research*, 57, 209–234.
- Bouchon, P., M. Aguilera, J., L. Pyle, D. (2003). Structure oil-absorption relationships during deep-fat frying. *Journal of Food Science*, 68(9), 2711–2716.
- Bouchon, P., Pyle, D.L. (2005). Modelling oil absorption during post-frying cooling: I: model development. *Food Bioproduction Processing*, 83, 253–260.
- Choe, E., Min, D.B. (2007). Chemistry of deep-fat frying oils. *Journal of Food Science*, 72, R77-86.
- Cortés, P., Badillo, G., Segura, L., Bouchon, P. (2016). The effect of different porous media on moisture loss and oil absorption profiles during frying using glass micromodels. *AIChE Journal*, 62, 629–638.
- Costa, R.M., Oliveira, F.A., Delaney, O., Gekas, V. (1999). Analysis of the heat transfer coefficient during potato frying. *Journal of Food Engineering*, 39, 293–299.
- Dana, D., Saguy, I.S. (2006). Mechanism of oil uptake during deep-fat frying and the surfactant effect-theory and myth. *Advances Colloid Interface Science*, 128–130, 267–272.
- Dragich, A.M., Krochta, J.M. (2010). Whey protein solution coating for fat-uptake reduction in deep-fried chicken breast strips. *Journal of Food Science*, 75, S43–S47.
- Drelich, J., Fang, C., and White, C. L. (2002). Measurement of interfacial tension in fluid-fluid systems. *Encyclopedia of Surface and Colloid Science*, 3, 3158-3163.
- Dueik, V., Bouchon, P. (2011). Vacuum frying as a route to produce novel snacks with desired quality attributes according to new health trends. *Journal of Food Science* 76, E188–E195.
- Dukhin, S.S., Fainerman, V.B., Miller, R. (1996). Hydrodynamic processes in dynamic bubble pressure experiments 1. A general analysis. *Colloids Surface Physicochemical Engineering Aspects*, 114, 61–73.
- Farkas, B.E., Hubbard, L.J. (2000). Analysis of convective heat transfer during immersion frying. *Dry. Technology*, 18, 1269–1285.
- Farkas, B.E., Singh, R.P., Rumsey, T.R. (1996a). Modeling heat and mass transfer in immersion frying. I, model development. *Journal of Food Engineering*, 29, 211–226.
- Farkas, B.E., Singh, R.P., Rumsey, T.R. (1996b). Modeling heat and mass transfer in immersion frying. II, model solution and verification. *Journal of Food Engineering*, 29, 227–248.
- Farid, M. M., and Chen, X. D. (1998). The analysis of heat and mass transfer during frying of food using a moving boundary solution procedure. *Heat and Mass transfer*, 34(1), 69-77.
- Gamble, M. H., Rice, P., and Selman, J. D. (1987). Relationship between oil uptake and moisture loss during frying of potato slices from tubers. *International Journal of Food Science and Technology*, 22(3), 233–241.

- García, M., Ferrero, C., Bértola, N., Martino, M., Zaritzky, N. (2002). Edible coatings from cellulose derivatives to reduce oil uptake in fried products. *Innovation in Food Science Emerging Technology*, 3, 391–397.
- Hubbard, L.J., Farkas, B.E. (1999). A Method for determining the convective heat transfer coefficient during immersion frying. *Journal of Food Process Engineering* 22, 201–214.
- Hughes, S.W. (2006). Measuring liquid density using archimedes principle. *Physical Education*, 41, 445–447.
- Ignat, A., Manzocco, L., Brunton, N.P., Nicoli, M.C., Lyng, J.G. (2015). The effect of pulsed electric field pre-treatments prior to deep-fat frying on quality aspects of potato fries. *Innov. Food Science Emerging Technology*, 65–69.
- Janositz, A., Noack, A. K., and Knorr, D. (2011). Pulsed electric fields and their impact on the diffusion characteristics of potato slices. *LWT - Food Science and Technology*, 44(9), 1939–1945.
- Kaczay, K. R. (2016). A comparison of the efficacy of radiant and immersion frying using hash brown patties as a model food matrix (Master of Science thesis). Retrieved from Purdue library repository. https://docs.lib.purdue.edu/open_access_theses/860/
- Kalogianni, E.P., Karapantsios, T.D., Miller, R. (2011). Effect of repeated frying on the viscosity, density and dynamic interfacial tension of palm and olive oil. *Journal of Food Engineering*, 105, 169–179.
- Karbowiak, T., Debeaufort, F., Voilley, A. (2006). Importance of Surface Tension Char. for Food, Pharmaceutical and Packaging Products: A Review. *Critical Reviews in Food Science and Nutrition*, 46, 391–407.
- Krokida, M., Oreopoulou, V., Maroulis, Z. (2000). Water loss and oil uptake as a function of frying time. *Journal of Food Engineering*, 44, 39–46.
- Krokida, M.K., Oreopoulou, V., Maroulis, Z.B., Marinos-Kouris, D. (2001). Effect of osmotic dedydration pretreatment on quality of french fries. *Journal of Food Engineering*, 49, 339–345.
- Maity, T., Bawa, A.S., Raju, P.S. (2014). Effect of vacuum frying on changes in quality attributes of jackfruit (*Artocarpus heterophyllus*) bulb slices. *International Journal of Food Science*, 2014.
- Mallikarjunan, P., Chinnan, M.S., Balasubramaniam, V.M., Phillips, R.D. (1997). Edible coatings for deep-fat frying of starchy products. *LWT- Food Science and Technology*, 30, 709–714.
- Mellema, M. (2003). Mechanism and reduction of fat uptake in deep-fat fried foods. *Trends Food Science Technology*, 14, 364–373.
- Miller, K.S., Singh, R.P., Farkas, B.E. (1994). Viscosity and heat transfer coefficients for canola, corn, palm, and soybean oil. *Journal of Food Processing and Preservation*, 18, 461–472.
- Moreira, R.G., Sun, X., Chen, Y. (1997). Factors affecting oil uptake in tortilla chips in deep-fat frying. *Journal of Food Engineering*, 31, 485–498.

- Moreno, M.C., Bouchon, P. (2008). A different perspective to study the effect of freeze, air, and osmotic drying on oil absorption during potato frying. *Journal of Food Science*, 73, E122-128.
- Moreno, M.C., Brown, C.A., Bouchon, P. (2010). Effect of food surface roughness on oil uptake by deep-fat fried products. *Journal of Food Engineering*, 101, 179–186.
- Nelson, L.V., Keener, K.M., Kaczay, K.R., Banerjee, P., Jensen, J.L., Liceaga, A. (2013). Comparison of the FryLess 100 K Radiant Fryer to oil immersion frying. *LWT - Food Science Technology*, 53, 473–479.
- Noureddini, H., Teoh, B.C., Davis Clements, L. (1992). Densities of vegetable oils and fatty acids. *Journal of American Oil Chemists' Society*, 69, 1184–1188.
- O'Meara, Meghan (2012). Determination of the Interfacial Tension between Oil-Steam and Oil-Air at Elevated Temperatures (Master's thesis). Retrieved from NCSU library repository. <https://repository.lib.ncsu.edu/handle/1840.16/8150>
- Orthofer, F.T., List, G.R. (2007a). 12 - Dynamics of Frying, in: Erickson, M.D. (Ed.), *Deep Frying (Second Edition)*. AOCS Press, pp. 253–275.
- Orthofer, F.T., List, G.R. (2007b). 18 - Evaluation of Used Frying Oil, in: Erickson, M.D. (Ed.), *Deep Frying (Second Edition)*. AOCS Press, pp. 329–342.
- Patterson, S.P., Phillips, R.D., McWatters, K.H., Hung, Y.C., Chinnan, M.S. (2004). Fat reduction affects quality of akara (fried cowpea paste). *International Journal of Food Science*, 39, 681–689.
- Pedreschi, F., Moyano, P. (2005). Effect of pre-drying on texture and oil uptake of potato chips. *LWT- Food Science and Technology*, 38, 599–604.
- Pendant drop (2018). KRÜSS - Advances Your Surf. Science URL <https://www.kruss-scientific.com/services/education-theory/glossary/pendant-drop/> (accessed 2.12.19).
- Pinthus, E. J., Weinberg, P., and Saguy, I. S. (1993). Criterion for Oil Uptake during Deep-fat Frying. *Journal of Food Science*, 58(1), 204–205.
- ramé-hart Contact Angle (2018). Ramé-Hart Instrum. Co Mon. Newsl. URL <http://www.ramehart.com/contactangle.htm> (accessed 2.12.19).
- Rao, M.A. (2007). Measurement of Flow and Viscoelastic Properties, in: *Rheology of Fluid and Semisolid Foods: Principles and Applications*. Springer, 59–151.
- Safari, A., Salamat, R., Baik, O. D. (2018). A review on heat and mass transfer coefficients during deep-fat frying: Determination methods and influencing factors. *Journal of Food Engineering*, 230, 114–123.
- Sandhu, J., Bansal, H., Takhar, P.S. (2013). Experimental measurement of physical pressure in foods during frying. *Journal of Food Engineering*, 115, 272–277.
- Snacking Motivations and Attitudes - US - 2017: Consumer market research report | Mintel.com. (2018). Retrieved February 6, 2019, from <https://store.mintel.com/snacking-motivations-and-attitudes-us-may-2017>.
- Thanatukorn, P., Kajiwara, K., Suzuki, T. (2007). Characterization of deep-fat frying in a wheat flour–water mixture model using a state diagram. *Journal of Science Food Agriculture*, 87, 2648–2656.

- Tseng, Y., Moreira, R., Sun, X. (1996). Total frying-use time effects on soybean-oil deterioration and on tortilla chip quality. *International Journal of Food Science Technology*, 31, 287–294.
- Ufheil, G., Escher, F. (1996). Dynamics of oil uptake during deep-fat frying of potato slices. *LWT- Food Science and Technology*, 29, 640–644.
- Usawakesmanee, W., Wuttijumnong, P., Chinnan, M. S., Jangchud, R. N., & Raksakulthai, N. (2005). The effects of edible coating ingredient as a barrier to moisture and fat of fried breaded potato. *Kasetsart Journal National Science*, 39(1), 98-108
- USDA/FSIS (2013). Deep Fat Frying and Food Safety.
- White, J.L. (1959). Liquid densitometry, in: Bockris, J.O.M., White, J.L., Mackenzie, J.D. (Eds.), *Physicochemical measurements at high temperature*. Research Academic Press, Inc., pp. 193-213.
- Wilhelmy plate method (2018). KRÜSS - Advances Your Surf. Science URL <https://www.kruss-scientific.com/services/education-theory/glossary/wilhelmy-plate-method/> (accessed 2.12.19).
- Ziaifar, A.M., Achir, N., Courtois, F., Trezzani, I., Trystram, G. (2008). Review of mechanisms, conditions, and factors involved in the oil uptake phenomenon during the deep-fat frying process. *International Journal of Food Science Technology*, 43, 1410–1423.

2. DETERMINATION AND MODELING OF DENSITY, VISCOSITY AND SURFACE TENSION OF FIVE VEGETABLE OILS AT ELEVATED TEMPERATURES ¹

Density, surface tension and viscosity of five food oils were experimentally measured using a Brookfield viscometer, Archimedean method and Pendant drop method respectively. Measurements were performed from 23 ± 1 °C to the oils' smoke point at intervals of every 20 °C. Density and surface tension decreased linearly with increasing temperature, whereas the viscosity decreased exponentially. Density was modelled using Modified Rackett equation, surface tension using the Eötvös equation and viscosity by Modified Andrade equation. Oil type influenced the density and viscosity of oil but was not shown to affect surface tension.

Keywords: vegetable oils, high temperature, density, viscosity, surface tension, modeling

2.1. Introduction

Deep fat frying is one of the oldest and the most commonly used technique to process foods, which involves submerging a food in hot oil (150-200 °C) for a short period of time until it reaches a safe minimum internal temperature (Farkas et al., 1996). It is a relatively low cost process in which the combination of temperature and heat affect the organoleptic properties of food such as flavor, texture and color (Bouchon and Pyle, 2005a; Saguy and Dana, 2003). Frying is a simultaneous heat and mass transfer process which causes dehydration of the product due to high oil temperature, thus, resulting in a product which has a porous and crispy exterior and a soft and moist interior (Dana and Saguy, 2006). The main reactions involved in this process are starch gelatinization, protein denaturation, aromatizing and coloring via Maillard reactions, rapid cooking, and texture and flavor development (Chang et al., 1978; Choe and Min, 2007; Ziaifar et al., 2008). Frying also causes changes in the flavor and stability of oils by hydrolysis, oxidation, and polymerization (Choe and Min, 2007).

¹ Reprinted from Shreya N. Sahasrabudhe, Veronica Rodriguez-Martinez, Meghan. O'Meara and Brian E. Farkas (2017) Density, viscosity, and surface tension of five vegetable oils at elevated temperatures: Measurement and modeling, International Journal of Food Properties, 20:sup2, 1965-1981, DOI: [10.1080/10942912.2017.1360905](https://doi.org/10.1080/10942912.2017.1360905)

According to the US Department of Agriculture (2015), world vegetable oil consumption has increased from 151.68 to 177.16 million metric tons from 2011/12 to 2015/16. Out of the total production, 73.4 % of the oil is used for food purposes (USDA-FAS, 2015); 20 % of which is for shallow and deep fat frying (Aydar et al., 2016). Fat plays an important role in enhancing the flavor of foods. Frying of food gives it a unique-flavor and texture combination which is very desirable to the consumers, making fried foods one of the most popular products (Bouchon, 2009). However, oil consumption poses significant health problems such as coronary heart diseases, cancer, diabetes, and hypertension, and is irreconcilable with consumer's awareness towards the consumption of healthier and low fat food products (Kim et al., 2010). There is an increasing consumer trend for less greasy and healthier products (Ziaifar et al., 2008). Considering the health impact and the popularity of fried foods, it is important to gain a better understanding of the principles and factors governing oil absorption so that they can be better controlled.

Deep fat frying is one of the most complex transport problems in the food industry. The main mechanisms proposed to govern the oil absorption during frying are water escape and oil uptake; capillary pressure; vapor pressure and vacuum effect; diffusion, adherence and drainage of oil on food surface (Mellema, 2003; Ziaifar et al., 2008). Heat is transferred by convection from the oil to the product surface followed by conduction from the surface to the interior of the product (Hubbard and Farkas, 2000). Mass transfer during frying is characterized by the simultaneous movement of water in the form of vapor from the food into the oil, and the movement of oil into the food (Farkas et al., 1996). Several factors such as moisture content, crust microstructure, product geometry, frying temperature and time, oil type, oil aging and pre and post frying treatments have shown to affect oil absorption during frying (Bouchon, 2009; Moreira et al., 1997; Ziaifar et al., 2008). Frying is known to affect the physical properties of oil such as density, viscosity and surface tension which can in turn affect the transport rate of oil, and thus the rate of oil absorption. Hence, the focus of this study is to understand the change in the oil physical properties at high temperatures, to predict the effect of the parameters affecting oil absorption at the frying temperature itself.

Density is an important factor which influences oil absorption as it affects the drainage rate after frying and also the mass transfer rate during the cooling stage of frying (Bouchon and Pyle, 2005b; Yilmaz, 2011). Density has been experimentally shown to be linearly dependent on temperature (Esteban et al., 2012; Nouredini et al., 1992a). However, there is no mathematical

equation to predict the effect of temperature on density, especially at high temperatures at which frying is conducted. Frying occurs at temperatures around 180 °C; however the densities of commonly used oils are known till around 110-140 °C (Esteban et al., 2012; Nouredini et al., 1992a). Hence to accurately determine transport rates, density needs to be determined and modelled at frying temperatures. A liquid pycnometer (Nouredini et al., 1992a), hydrometer with temperature controller (Esteban et al., 2012) are the most commonly used methods to determine density of a liquid at temperatures above room temperature. Both the methods involve use of glass apparatus, hence glass expansion coefficient needs to be accounted for. Also, the assembly of the apparatus is complex. Archimedean method has been successfully used to determine density of liquids at high temperatures (molten igneous rocks) (White, 1959); however it has not been used to measure densities of food oils.

Ziaifar et al. (2008) reported that viscosity of oil is one of the main factors which governs oil absorption and drainage. The higher is the oil viscosity, the slower is the oil drainage. Oil viscosity depends on oil type as well as frying temperature and oil quality. Esteban et al. (2012); Kim et al. (2010); and Nouredini et al. (1992b); Yilmaz (2011) measured viscosities of vegetable oils from room temperature up to maximum of 130°C using a glass capillary viscometer. Correlations were developed for viscosity with temperatures using empirical equations as well as relating fatty acid composition to the viscosity change. These studies give valuable information on the effect of temperature on oil degradation but fail to develop models which can be used as predictors of oil viscosity, especially at the frying temperatures. Viscometer and Rheometer are the most commonly used equipment's to measure oil viscosity at high temperatures (Esteban et al., 2012; Kalogianni et al., 2011; Yilmaz, 2011; Ziaifar et al., 2008). Modelling viscosity at frying temperatures can give a better understanding of the flow behavior of the oil during drainage, and thus help to characterize oil absorption better.

Surface and interfacial tension (IFT) play a key role in mechanisms of oil uptake, as frying oil moves into the food's pores, which are filled with water and/or steam (Dana and Saguy, 2006; Moreno and Bouchon, 2008). Surface tension of oils is measured at room temperature, however, frying process is conducted at temperatures between 150 - 180 °C. For many pure liquids, an increase in temperature causes a linear decrease in the surface tension. Investigation of surface and interfacial tensions at high temperature is thus a key element required to characterize and predict the oil absorption. Kalogianni et al. (2011) measured the interfacial tension of olive oil and palm

oil at room temperature after repeated frying cycles using the pendant drop technique and found a dynamic decrease in interfacial tension values for both oil types. Thus, frying has a significant effect on surface tension of oil and the effect needs to be predicted at high temperatures to gain a better understanding of oil absorption. Surface tension can be measured by many methods including: Pendant drop, Du Nouy ring, Wilhelmy plate, Maximum bubble pressure, and Contact angle (Adamson and Gast, 1967). The Pendant drop technique is commonly used to measure the IFT of hydrocarbons and crude oils at high temperature (Flock et al., 1986; Huygens et al., 1995) but has not been used to measure the surface tension of food oils at high temperatures.

While oil viscosity and density as affected by temperature and oil composition have received some attention, the surface tension of oils at frying temperatures in pure or mixed systems has not been studied to a great extent (Miller et al., 1994). The current study seeks to address this gap. The objective of this study is to determine and mathematically model surface tension, density and viscosity of commonly used food oils at high temperatures. This will help to gain a better understanding of oil absorption, as the factors affecting heat and mass transfer rates during frying can be predicted more accurately, at the frying temperature itself.

2.2. Materials and Methods

2.2.1. Materials

Canola oil (Wesson, ConAgra Foods Inc.; Omaha NE, USA), extra virgin olive oil (Filippo Berio, SALOV North America Corp.; Lyndhurst NJ, USA), soybean oil (Crisco, The J.M. Smucker Co.; Orrville OH, USA), peanut oil (LouAna, Ventura Foods, LLC; Brea CA, USA) and corn oil (Mazola, ACH Food Companies, Inc; Memphis TN, USA) were purchased from a local market. Decane was purchased from TCI America (Portland OR, USA). Acetone was purchased from VWR (Radnor, PA, USA). Stainless steel wire (diameter: 0.76 mm) was bought from Hobart Welders (NorthernToold; Raleigh NC, USA). A stainless-steel ball (diameter: 25.4 mm) was obtained from the Precision Instrument Machine Shop (North Carolina State University Raleigh, NC, USA).

2.2.2. Density measurements

Oil density was determined by the Archimedean method as described by White (1959). This method uses a solid object of known volume and mass suspended in the test liquid by a wire

hanging from a scale. A stainless-steel ball welded to a stainless-steel wire was used as the reference material for this study. The density (ρ) was calculated using Eq. 2.1.

$$\rho = \frac{\beta+s}{V^0+v'} \quad \text{Eq. 2.1}$$

where β is the buoyancy (Eq. 2.2), V^0 is the volume of the reference object, s is the surface tension between the liquid and the wire, and v' is the volume of immersed wire. For the purpose of this study, s was assumed negligible, V^0 was determined to be 8.58 cm^3 , and v' equal to 0.01 cm^3 .

$$\beta = m_v - m_f \quad \text{Eq. 2.2}$$

where m_v and m_f are the mass of the reference object plus immersed wire suspended *in vacuo*, and in the test fluid respectively. The value determined for m_v was 69.67 g .

Measurements were performed at room temperature ($22 \pm 1 \text{ }^\circ\text{C}$), $40 \text{ }^\circ\text{C}$ and at increasing intervals of $20 \text{ }^\circ\text{C}$ until the smoke point of each oil was reached ($200 \text{ }^\circ\text{C}$; except for olive oil, $180 \text{ }^\circ\text{C}$). Prior to each measurement, the oil was placed inside a beaker and heated under constant agitation until the desired temperature was reached. To maintain a uniform temperature, the wire/ball was also heated along with the oil in the beaker. Measurements were performed in triplicate.

2.2.3. Surface tension measurements

The surface tension of the five vegetable oils in air was determined by pendant drop method using a KRÜSS (Model- DSA30B, KRÜSS GmbH, Hamburg, Germany) as well as ramé-hart goniometer (ramé-hart, Advanced Goniometer, model 300, Succasunna, NJ). The surface tension was measured using Drop Shape Analysis software and DropImage software respectively. An elevated temperature syringe with a 22-gauge stainless steel needle was used to form the drops inside an environmental chamber equipped with a temperature control system (P/N 100-11, P/N 100-10-20, P/N 100-10-12-22, and P/N 100-07 respectively; ramé-hart instrument co.; Succasunna NJ, USA) with air as the surrounding medium. The environmental chamber and the high temperature syringe, both equipped with a temperature control system (P/N 100-50; ramé-hart instrument co.; Succasunna NJ, USA) and SOLO Temperature Controller Configuration software (AutomationDirect; Cumming GA, USA) were used. Additionally, temperature was monitored at the vicinity of the needle where the drop was generated, using a thermocouple (P/N KMQSS-062U,

OMEGA Engineering, Inc; Stamford CT, USA) attached to a data logger with Logger Lite software (LabQuest Mini, Vernier Software and Technology, LLC.; Beaverton OR, USA). Acetone was used to clean all surfaces before and after each experiment to avoid contamination; surfaces were allowed to dry for one minute before starting a new measurement.

Similar to density experiments, measurements were performed at room temperature (22 ± 1 °C), 40 °C and at increasing intervals of 20 °C until the smoke point of each oil was reached (200 °C; except for olive oil, 180 °C). Three measurements were performed at each temperature.

2.2.4. Viscosity measurements

The viscosity (μ) of the vegetable oils was determined by a Brookfield viscometer equipped with a thermo-container and programmable temperature controller (LV-DVIII, HT-60, HT-110FR respectively; Brookfield Engineering Laboratories, Inc.; Middleboro MA, USA). The thermo-container was equipped with a sample chamber, and a spindle (HT-2 and SC4-18 respectively; Brookfield Engineering Laboratories, Inc.; Middleboro MA, USA). The system was cooled using a cooling plug assembly (HT-26Y, Brookfield Engineering Laboratories, Inc.; Middleboro MA, USA) attached to a pressurized air nozzle. The heating profile for the temperature controller was set up as: heat from 23 °C until the smoke point of each oil (200 °C, except olive oil 180 °C) in increments of 20 °C and holding at each temperature for 5 min. The measurements were performed at different RPM setting to confirm the Newtonian behavior of the five oils studied (data not shown).

2.2.5. Mathematical modeling

2.2.5.1. Density

Density as a function of temperature was predicted based on the modified Racket equation (Eq. 2.3) developed by Spencer and Danner (1972) which estimates the molar volume of a saturated pure liquid (V_s):

$$V_s = \left(\frac{RT_c}{P_c} \right) Z_{RA} [1 + (T_r)^{2/7}] \quad \text{Eq. 2.3}$$

where V_s is in cm^3/mol , T_c is the critical temperature (K), P_c is the critical pressure (bar), R is the ideal gas constant ($\text{cm}^3\text{bar}/\text{mol K}$), Z_{RA} is the Rackett parameter which is unique to each compound, and T_r is the reduced temperature (K).

Halvorsen et al., 1993) presented a variation of Eq. 2.3. to estimate the density of vegetable oils (Eq. 2.4), which considers the mixture of fatty acids and a correction factor to account for triglycerides.

$$\rho = \frac{(\sum x_i MW_i)}{R \left(\sum \frac{x_i T_{C_i}}{P_{C_i}} \right) (\sum x_i Z_{RA_i}) [1 + (T_r)^{2/7}]} + F_c \quad \text{Eq. 2.4}$$

where x_i is the mole fraction of each component, MW_i the molecular weight (g/mol) of each component, and F_c is the correction factor. Values of MW_i , T_c , P_c , and Z_{RA} corresponding to each fatty acid present in the composition of each oil used in this study are reported in Table 2.1. The reduced temperature (T_r) was obtained using the temperature (T) at which the estimation was done and a molar average of the critical temperatures as pseudocritical temperature (Eq. 2.5) (Halvorsen et al., 1993).

$$T_r = \frac{T}{(\sum x_i T_{C_i})} \quad \text{Eq. 2.5}$$

The correction factor (F_c) ranges from 0.02 to 0.04 and only depends on oil type, more specifically the molecular weight. When the molecular weight of the oil (MW_{oil}) was lower than 875 g/mol, F_c was calculated using Eq. 2.6; however, when it was higher, Eq. 2.7 was used. MW_{oil} was calculated based on the fatty acid composition using Eq. 2.8 (Halvorsen et al., 1993).

$$F_c = 0.0236 + 0.000082 |875 - MW_{oil}| \quad \text{Eq. 2.6}$$

$$F_c = 0.0236 + 0.000098 |875 - MW_{oil}| \quad \text{Eq. 2.7}$$

$$MW_{oil} = 3 \sum x_i MW_i + 38.0488 \quad \text{Eq. 2.8}$$

Table 2.1. Molecular weight, critical properties and Racket parameters of fatty acids

Fatty acid	MW_i (g/mol)	T_{Ci} (K)*	P_{Ci} (bar)*	Z_{RAi}*
C16:0	256.43	799.89	14.08	0.2267
C16:1	254.43	800.34	14.71	0.2290
C18:0	284.49	819.00	12.25	0.2205
C18:1	282.49	819.41	12.76	0.2230
C18:2	280.49	819.82	13.31	0.2255
C18:3	278.49	820.23	13.89	0.2284
C20:0	312.54	836.65	10.76	0.2149
C20:1	310.54	837.03	11.18	0.2172
C22:0	340.59	853.06	9.52	0.2095
C24:0	368.65	868.38	8.49	0.2040
C26:0	396.70	882.76	7.61	0.1990

*Obtained from Halvorsen *et al.* (1993)

2.2.5.2. Surface Tension

Surface tension was predicted by the Eötvös equation (Eq. 2.9) as a direct function of temperature for data obtained from both the goniometers:

$$\gamma_{LG}(MW_{oil}/\rho_{oil})^{2/3} = K_E(T_{C,oil} - T) \quad \text{Eq. 2.9}$$

where γ_{LG} is the liquid-gas surface tension (mN/m), MW_{oil} is the oil's molar mass (g/mol), ρ_{oil} is the oil's density (g/cm^3), K_E is the Eötvös constant ($dynes\ cm/mol^{2/3}\ K$), T_C is the oil's critical temperature (K), and T is the temperature (K) at which γ_{LG} is estimated. K_E is the measure of entropy of the surface and was adjusted for each of the systems. It is known that geometrically complex molecules have higher K_E values (e.g. tripalmitine, $K_E = 5.4$), than those almost spherical molecules (e.g. mercury, $K_E \approx 1$) (Palit, 1956). Hence, K_E values were determined for each oil type. The surface tension data was also modelled using the predicted density values obtained from the Rackett equation and fitting them in the Eötvös equation.

2.2.5.3. Viscosity

Viscosity as a function of temperature was modelled using the modified Andrade equation (Eq. 2.10) which is derived from the Arrhenius equation and was used by Esteban *et al.* (2012), Nouredini *et al.* (1992b), and Yilmaz (2011) to understand the viscosities of vegetable oils and fatty acids.

$$\nu = e^{(a+b/T+c/T^2)} \quad \text{Eq. 2.10}$$

where ν is the oil kinematic viscosity (mm^2/s), T is the temperature (K), a , b and c are correlation constants which are calculated using the method of least squares.

2.1.1. Percentage error

The percentage errors ($E \%$) were calculated using Eq. 2.11:

$$E \% = \frac{\text{abs}(\text{experimental value} - \text{predicted value})}{\text{experimental value}} \times 100 \quad \text{Eq. 2.11}$$

2.2.6. Statistical Analysis

Measurements were performed in triplicate and data was analyzed using Minitab 17 (Minitab Inc., State College PA, USA). Regression (REG) analysis were performed on measured viscosity, density and surface tension for all five oils. Tukey's test ($\alpha = 0.05$) was used to determine differences among measured physical properties with temperature for each oil.

2.3. Results and Discussion

2.3.1. Effect of temperature and oil type on physical properties of oils

2.3.1.1. Density

Density of soybean, canola, corn, peanut and olive oil was measured by the Archimedean method from room temperature to 200°C (except olive oil, 180°C) (Table 2.2). The density values obtained were similar to those previously reported in literature (Noureddini et al., 1992a). Regression analysis showed that there was a linear decrease in density with temperature for all oils (Fig. 2.1). The intercept and slopes for each oil are reported in Table 2.3. Statistical analysis using General linear model (GLM) showed significant effect ($p < 0.05$) of temperature and oil type on density.

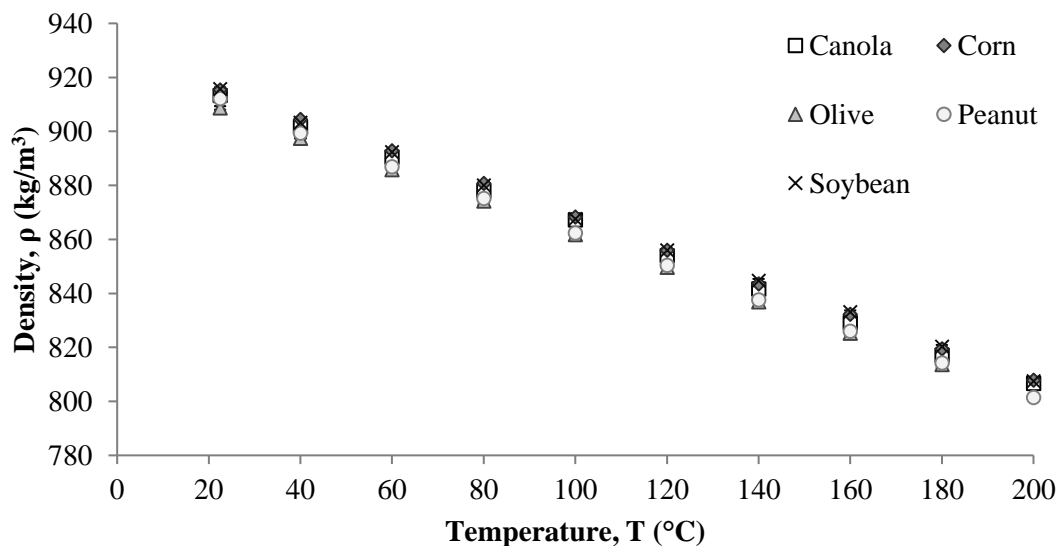


Fig. 2.1. Density values of five vegetable oils from room temperature to the smoke point of each oil

Table 2.2. Comparison of the average density values between five vegetable oils at different temperatures

T (°C)	Canola oil	Corn oil	Olive oil	Peanut oil	Soybean oil
ρ_{oil} (kg/m ³)					
22 ± 1	913.3 ± 0.7 ^{b,c}	915.3 ± 0.7 ^{a,b}	908.7 ± 0.7 ^d	912.1 ± 0.7 ^c	915.7 ± 0.7 ^a
40	901.7 ± 0.7 ^f	904.4 ± 0.0 ^e	897.4 ± 0.0 ^g	899.3 ± 0.7 ^g	903.3 ± 0.0 ^{e,f}
60	890.4 ± 0.0 ⁱ	892.8 ± 0.0 ^h	885.8 ± 0.0 ^j	886.8 ± 0.7 ^j	892.4 ± 0.7 ^{h,i}
80	878.0 ± 0.7 ^l	880.7 ± 0.7 ^k	874.2 ± 1.2 ^m	875.2 ± 0.7 ^m	880.0 ± 0.0 ^{k,l}
100	867.2 ± 1.2 ⁿ	868.3 ± 0.0 ⁿ	861.7 ± 0.7 ^o	862.4 ± 0.7 ^o	867.6 ± 0.7 ⁿ
120	854.0 ± 0.7 ^p	855.9 ± 0.7 ^p	849.7 ± 0.0 ^q	850.4 ± 0.7 ^q	855.9 ± 0.7 ^p
140	841.6 ± 0.0 ^s	843.5 ± 0.7 ^{r,s}	836.9 ± 0.0 ^t	837.6 ± 0.7 ^t	844.7 ± 0.7 ^r
160	829.1 ± 0.7 ^v	832.2 ± 0.0 ^u	825.3 ± 0.0 ^w	825.9 ± 0.7 ^w	833.0 ± 0.7 ^u
180	817.1 ± 0.0 ^y	819.4 ± 0.0 ^x	813.6 ± 1.2 ^z	814.3 ± 0.7 ^z	820.2 ± 0.7 ^x
200	806.6 ± 0.0 ^{aa}	807.8 ± 0.0 ^{aa}	—	801.5 ± 0.7 ^{ab}	807.4 ± 0.7 ^{aa}

± : corresponds to the standard deviation, n=3.

^{a-aa} : Tukey mean comparison per parameter (95 % Confidence)- no significant difference between values sharing same letter.

Table 2.3. Intercept (ρ_0), slope (ρ_1) and correlation coefficient (r^2) values corresponding to the empirical equation to predict density of each vegetable oil

Oil type	ρ_0	ρ_1	r^2	Temp range (°C)
Canola	926.7	-0.606	0.999	22-200
Corn	928.9	-0.606	1.000	22-200
Olive	922.2	-0.606	1.000	22-180
Peanut	924.2	-0.615	1.000	22-200
Soybean	928.2	-0.600	0.999	22-200

2.3.1.2. Surface tension

Surface tension of soybean, canola, corn, peanut and olive oil was measured using a KRÜSS and ramé-hart goniometer from room temperature to 200 °C (except olive oil 180 °C) (Table 2.5). Regardless of the oil type or the equipment used, there was a significant decrease ($p < 0.05$) in surface tension as the temperature increased; Fig. 2.2 shows data obtained using the KRÜSS goniometer. The results obtained agree with data previously reported in literature (Xu et al., 2017). Regression analysis showed that there was a linear decrease in surface tension with temperature for all oils. The intercept and slopes for each oil are reported in Table 2.4. There was a difference in values for the surface tension measured with KRÜSS vs ramé-hart equipment mainly because of the numerical method used by each equipment in calculating surface tension from the Young's equation.

Statistical analysis showed significant effect ($p < 0.05$) of temperature and oil type on the surface tension values. However, the difference in surface tension values for different oil types is within the range of accuracy of each equipment and the effect can be ignored. Thus, temperature was the only significant factor affecting surface tension. This finding agrees with the result from Xu et al., 2017 where no effect of type of oil on surface tension was observed, and could be attributed to the presence of long-acyl chains in all oils whose surface tensions are not very different from each other.

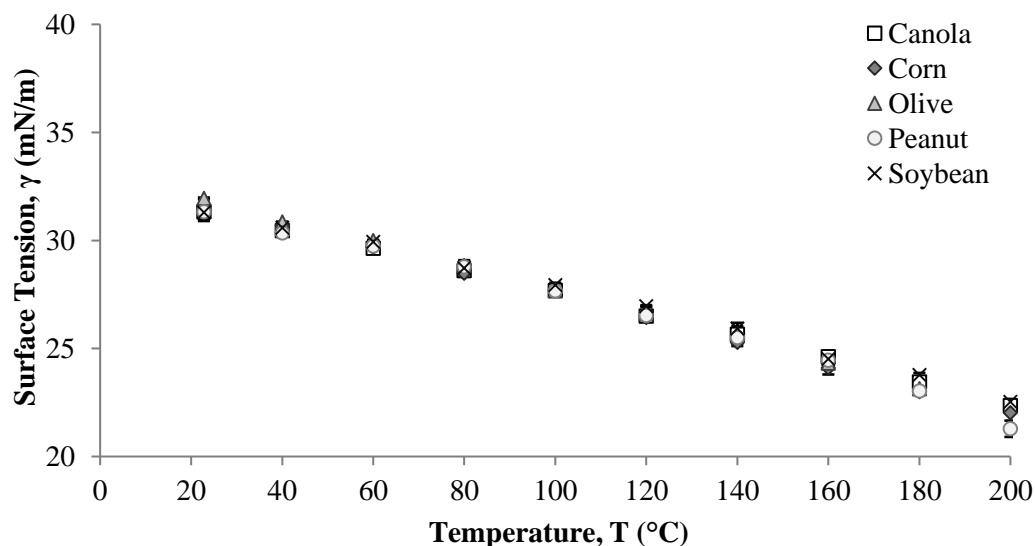


Fig. 2.2. Surface tension values of five vegetable oils from room temperature to each oil's smoke point determined using a KRÜSS goniometer

Table 2.4. Intercept (γ_0), slope (γ_1) and correlation coefficient (r^2) values corresponding to the empirical equation to predict surface tension of each vegetable oil

Oil type	γ_0	γ_1	r^2	Temp range (°C)
For values determined using KRÜSS goniometer				
Canola	32.58	-0.050	0.996	23 - 200
Corn	32.92	-0.055	0.997	23 - 200
Olive	33.20	-0.055	0.994	23 - 180
Peanut	32.90	-0.055	0.988	23 - 200
Soybean	32.72	-0.050	0.991	23 - 200
For values determined using ramé-hart goniometer				
Canola	33.94	-0.071	0.999	23 - 200
Corn	33.41	-0.069	0.997	23 - 200
Olive	33.65	-0.070	0.999	23 - 180
Peanut	33.38	-0.067	0.995	23 - 200
Soybean	30.74	-0.062	0.993	23 - 200

Table 2.5. Comparison of the average surface tension values between five vegetable oils at different temperatures measured using KRÜSS and ramé-hart goniometers

T (°C)	Canola oil		Corn oil		Olive oil γ (mN/m)		Peanut oil		Soybean oil	
Determined using KRÜSS goniometer										
23±0	31.3 ± 0.3	b,c	31.6 ± 0.1	a,b	31.9 ± 0.0	a	31.3 ± 0.1	b,c	31.3 ± 0.4	b,c,d
40	30.5 ± 0.2	e,f	30.7 ± 0.1	d,e	30.9 ± 0.0	c,d,e	30.3 ± 0.2	e,f	30.6 ± 0.3	e
60	29.6 ± 0.2	g	29.7 ± 0.1	g	30.0 ± 0.0	f,g	29.7 ± 0.0	g	29.9 ± 0.0	f,g
80	28.6 ± 0.2	h	28.5 ± 0.1	h,i	28.8 ± 0.2	h	28.8 ± 0.1	h	28.7 ± 0.4	h
100	27.7 ± 0.1	j	27.7 ± 0.1	j	27.7 ± 0.0	j	27.7 ± 0.1	j	27.9 ± 0.1	i,j
120	26.5 ± 0.1	k	26.4 ± 0.2	k,l	26.6 ± 0.1	k	26.5 ± 0.0	k	27.0 ± 0.0	k
140	25.6 ± 0.2	m,n	25.3 ± 0.2	n	25.7 ± 0.5	m,n	25.5 ± 0.1	m,n	25.9 ± 0.1	l,m
160	24.6 ± 0.1	o	24.1 ± 0.1	o,p	24.3 ± 0.0	o,p	24.5 ± 0.0	o	24.5 ± 0.3	o
180	23.5 ± 0.0	q,r	23.0 ± 0.3	r,s	23.1 ± 0.1	r	23.0 ± 0.1	r,s	23.8 ± 0.1	p,q
200	22.4 ± 0.1	t	22.0 ± 0.2	t	–	–	21.3 ± 0.4	u	22.5 ± 0.1	s,t
Determined using ramé-hart goniometer										
23 ± 1	32.4 ± 0.1	a	32.2 ± 0.1	b	32.0 ± 0.1	b	32.2 ± 0.1	a,b	29.4 ± 0.0	g
40	31.3 ± 0.1	c	30.6 ± 0.1	e	30.9 ± 0.1	d	30.9 ± 0.0	d	28.4 ± 0.1	i
60	29.7 ± 0.0	f	29.3 ± 0.0	g,h	29.5 ± 0.1	f,g	29.2 ± 0.0	h	27.2 ± 0.1	l
80	28.2 ± 0.1	j	27.8 ± 0.0	k	28.1 ± 0.1	j	27.6 ± 0.0	k	25.9 ± 0.1	p
100	26.7 ± 0.1	m	26.3 ± 0.0	n,o	26.5 ± 0.1	m,n	26.2 ± 0.1	o	24.2 ± 0.1	s
120	25.3 ± 0.1	q	25.0 ± 0.1	r	25.1 ± 0.0	q,r	25.3 ± 0.1	q	23.0 ± 0.1	v
140	24.0 ± 0.1	s,t	23.7 ± 0.0	u	23.7 ± 0.1	u	23.9 ± 0.0	t	21.8 ± 0.1	z
160	22.7 ± 0.0	w,x	22.2 ± 0.0	y	22.5 ± 0.1	x	22.7 ± 0.0	w	20.9 ± 0.1	ac
180	21.2 ± 0.1	ab	21.1 ± 0.0	ab	21.1 ± 0.1	ab	21.5 ± 0.1	aa	19.5 ± 0.1	ae
200	20.1 ± 0.1	ad	20.0 ± 0.1	ad	–	–	20.0 ± 0.0	ad	19.0 ± 0.1	af

± : corresponds to the standard deviation, n≥3.

^{a-t} : Tukey mean comparison per parameter (95 % Confidence)- no significant difference between values sharing same letter.
Tukey mean analysis conducted separately for each equipment.

2.3.1.3. Viscosity

Viscosity of soybean, canola, corn, peanut and olive oil was measured using a viscometer from room temperature to 200 °C (Table 2.6). All the oils used in the study showed Newtonian behavior at the range of temperatures studied. Regardless of the oil type, there was a significant decrease ($p < 0.05$) in viscosity as the temperature increased (Fig. 2.3).

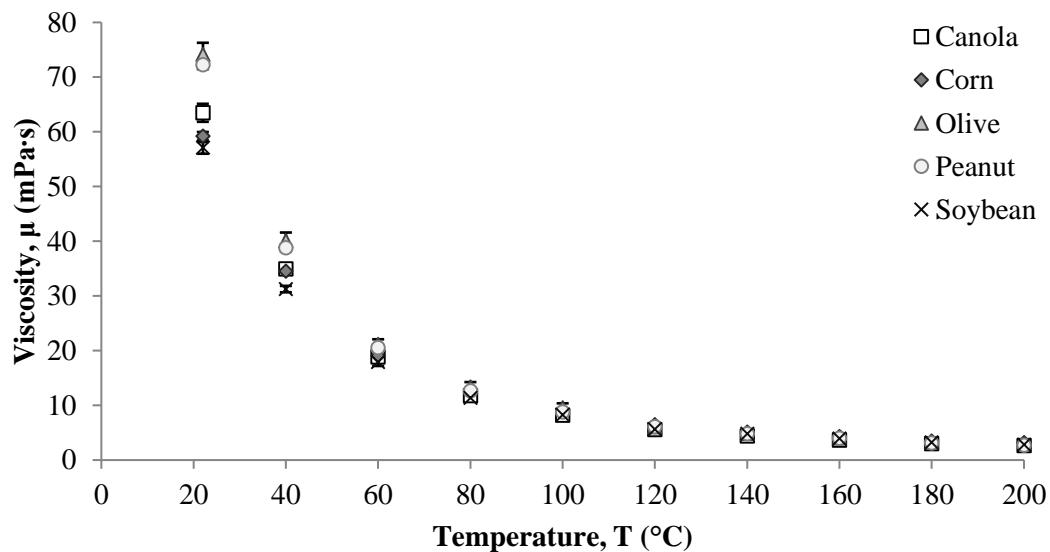


Fig. 2.3. Viscosity values determined for five vegetable oils from room temperature to the smoke point of each oil

Table 2.6. Comparison of the average viscosity values between five vegetable oils over a range of temperatures

T (°C)	Canola oil		Corn oil		Olive oil		Peanut oil		Soybean oil	
	μ (mPa·s)									
22±1	63.5 ± 1.6	c	59.2 ± 0.8	d	74.1 ± 2.2	a	72.2 ± 0.8	b	57.1 ± 1.1	e
40	34.9 ± 0.9	h	34.5 ± 0.6	h	40.1 ± 1.5	f	38.8 ± 0.7	g	31.3 ± 0.6	i
60	18.8 ± 0.3	k	19.1 ± 0.3	k	21.1 ± 0.9	j	20.5 ± 0.4	j	17.9 ± 0.7	k
80	11.8 ± 0.4	m,n	12.5 ± 0.2	l,m,n	13.4 ± 0.9	l	12.6 ± 0.4	l,m	11.4 ± 0.6	n
100	8.2 ± 0.4	o,p	9.0 ± 0.2	o,p	9.6 ± 0.8	o	8.8 ± 0.5	o,p	8.3 ± 0.6	p
120	5.5 ± 0.2	q,r,s,t	6.4 ± 0.3	q	6.1 ± 0.2	q,r	6.1 ± 0.5	q,r	5.6 ± 0.4	q,r,s
140	4.4 ± 0.1	s,t,u,v,w	5.1 ± 0.2	r,s,t,u	4.8 ± 0.2	s,t,u,v	4.8 ± 0.5	s,t,u,v	4.8 ± 0.7	s,t,u,v
160	3.7 ± 0.2	v,w,x,y,z	4.3 ± 0.2	t,u,v,w	4.0 ± 0.1	u,v,w,x	4.0 ± 0.5	u,v,w,x	3.9 ± 0.3	u,v,w,x,y
180	3.0 ± 0.2	x,y,z	3.5 ± 0.1	w,x,y,z	3.3 ± 0.1	w,x,y,z	3.1 ± 0.2	w,x,y,z	3.2 ± 0.3	w,x,y,z
200	2.6 ± 0.3	z	3.1 ± 0.2	w,x,y,z			2.7 ± 0.1	y,z	2.8 ± 0.3	x,y,z

± : corresponds to the standard deviation, $n \geq 3$.

^{a-z} : Tukey mean comparison per parameter (95 % Confidence) no significant difference between values sharing same letter.

In the current study, viscosity was found to have a power law relation with temperature (Eq. 2.12) irrespective of the type of oil used.

$$\mu = aT^b \quad \text{Eq. 2.12}$$

where μ is the dynamic viscosity ($mPa \cdot s$), T is the temperature ($^{\circ}C$), a is the coefficient, and b is the power of the equation obtained by regression analysis (Table 2.7).

The viscosity values are similar to those obtained by Nouredini et al. (1992b), Miller et al. (1994) and Ziiaifar et al. (2008). It was observed that the viscosity was quadratic function of temperature for all the oils. Statistical analysis using showed significant effect ($p < 0.05$) of temperature and oil type on the viscosity values; differences between oils were more noticeable at temperatures below $100^{\circ}C$.

Table 2.7. Parameters a and b , and correlation coefficient (r^2) values corresponding to the empirical equation to predict viscosity for each vegetable oil

Oil type	a	b	r^2	Temp range (°C)
Canola	8299.80	-1.52	0.99	22 - 200
Corn	5188.03	-1.39	0.99	22 - 200
Olive	10358.12	-1.54	0.99	22 - 180
Peanut	10463.01	-1.55	0.99	22 - 200
Soybean	5332.41	-1.42	0.99	22 - 200

2.3.2. Mathematical modeling of physical properties of oils at high temperatures

2.3.2.1. Density

Density was modelled as a function of temperature using the modified Rackett equation (Eq. 2.4). In order to predict the density of a vegetable oil using this equation, it is necessary to know the critical temperature, critical pressure, molecular weight, and Rackett parameter of each fatty present in the oil (Table 2.1), as well as the molar ratios at which the fatty acids are present. Rackett parameter is estimated using these values and is a measure of the molar volume of a saturated pure liquid (Yamada and Gunn, 1973). The T_c , P_c and Z_{RA} were calculated as the sum of the corresponding property for each fatty acid present in the oil weighted with its correspondent molar fraction; MW_{oil} was calculated using Eq. 2.8 (Table 2.8). Similar trends were observed between experimental and predicted data with increasing temperature (Fig. 2.4). The predicted values and error (E %) at the temperatures at which experiments were conducted for all five oils used in the study are reported in Table 2.9. The error increased with increasing temperature, but the overall error was not higher than two percent for the temperature range used in the study.

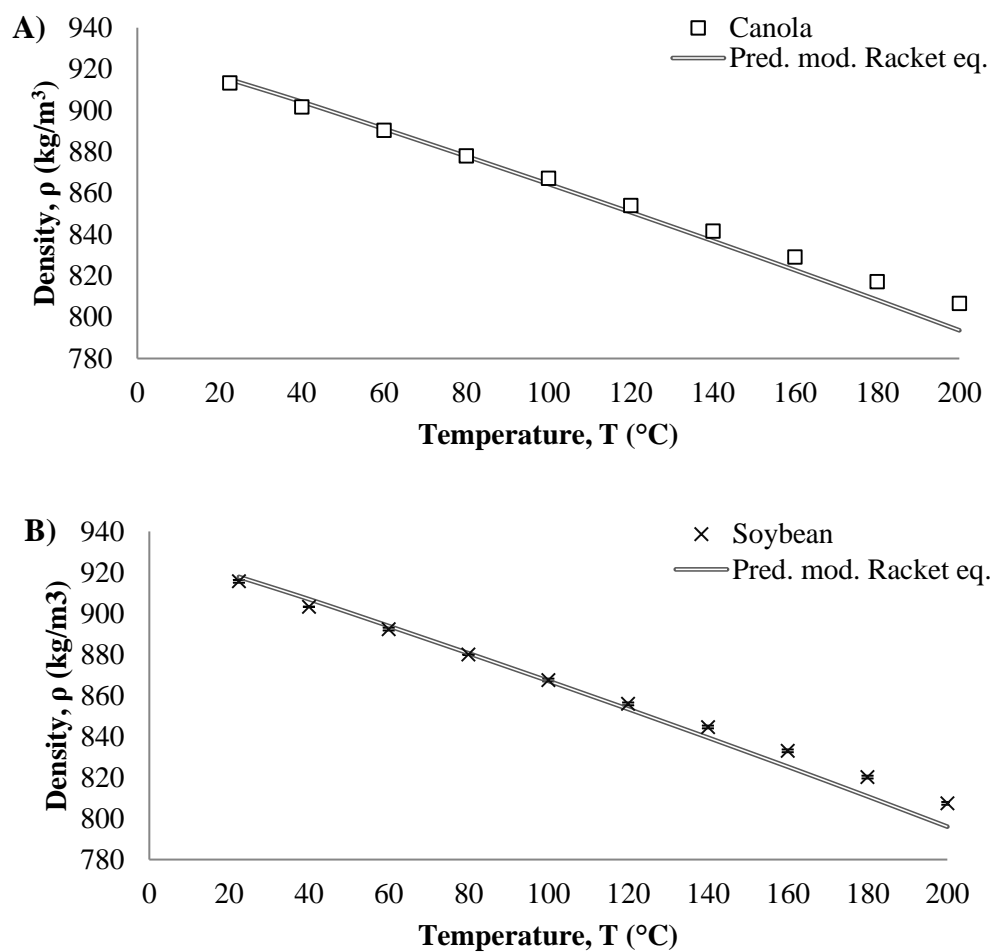


Fig. 2.4. Comparison between density experimental values of A) Canola oil, and B) Soybean oil and their corresponding predicted values by the modified Racket equation

Table 2.8. Molecular weight, critical temperature, and critical pressure of five vegetable oils

Oil type	MW _{oil} (g/mol)	T _{C oil} (K)	P _{C oil} (bar)	Z _{RA oil}
Canola	881.8 ± 0.0	819.1 ± 0.0	13.0 ± 0.0	0.224 ± 0.000
Corn	873.2 ± 0.0	817.3 ± 0.0	13.2 ± 0.0	0.225 ± 0.000
Olive	874.5 ± 0.5	816.8 ± 0.1	13.0 ± 0.0	0.224 ± 0.000
Peanut	887.5 ± 0.1	819.7 ± 0.0	12.8 ± 0.0	0.223 ± 0.000
Soybean	873.8 ± 0.0	817.7 ± 0.0	13.3 ± 0.0	0.225 ± 0.000

Table 2.9. Predicted density values for each vegetable oil by the modified Rackett equation and their corresponding percentage error

T (°C)	Canola oil			Corn oil			Olive oil			Peanut oil			Soybean oil		
	ρ _{oil} (kg/m ³)		E %	ρ _{oil} (kg/m ³)		E %	ρ _{oil} (kg/m ³)		E %	ρ _{oil} (kg/m ³)		E %	ρ _{oil} (kg/m ³)		E %
	EXP	PRED		EXP	PRED		EXP	PRED		EXP	PRED		EXP	PRED	
22															
± 1	913.3 ^b	915.0 ^a	0.2	915.3 ^b	917.0 ^a	0.2	908.7 ^b	910.9 ^a	0.2	912.1 ^a	910.2 ^a	0.2	915.7 ^b	917.8 ^a	0.2
40	901.7 ^d	904.2 ^c	0.3	904.4 ^d	906.1 ^c	0.2	897.4 ^d	900.1 ^c	0.3	899.3 ^b	899.5 ^b	0.0	903.3 ^d	907.0 ^c	0.4
60	890.4 ^e	891.1 ^e	0.1	892.8 ^e	893.0 ^e	0.0	885.8 ^e	887.0 ^e	0.1	886.8 ^c	886.5 ^c	0.0	892.4 ^e	893.9 ^e	0.2
80	878.0 ^f	877.9 ^f	0.0	880.7 ^f	879.7 ^g	0.1	874.2 ^f	873.8 ^f	0.0	875.2 ^d	873.3 ^e	0.2	880.0 ^f	880.6 ^f	0.1
100	867.2 ^g	864.4 ^h	0.3	868.3 ^h	866.2 ⁱ	0.2	861.7 ^g	860.3 ^h	0.2	862.4 ^f	859.9 ^g	0.3	867.6 ^g	867.1 ^g	0.0
120	854.0 ⁱ	850.8 ^j	0.4	855.9 ^j	852.5 ^k	0.4	849.7 ⁱ	846.6 ^j	0.4	850.4 ^h	846.3 ⁱ	0.5	855.9 ^h	853.4 ⁱ	0.3
140	841.6 ^k	836.9 ^l	0.6	843.5 ^l	838.6 ^m	0.6	836.9 ^k	832.7 ^l	0.5	837.6 ^j	832.5 ^k	0.6	844.7 ^j	839.5 ^k	0.6
160	829.1 ^m	822.8 ⁿ	0.8	832.2 ⁿ	824.4 ^o	0.9	825.3 ^m	818.6 ⁿ	0.8	825.9 ^l	818.4 ^m	0.9	833.0 ^l	825.3 ^m	0.9
180	817.1 ^o	808.4 ^p	1.1	819.4 ^p	810.0 ^q	1.2	813.6 ^o	804.2 ^p	1.2	814.3 ⁿ	804.1 ^o	1.3	820.2 ⁿ	810.8 ^o	1.1
200	806.6 ^q	793.6 ^r	1.6	807.8 ^r	795.2 ^s	1.6	—	—	—	801.5 ^p	789.4 ^q	1.5	807.4 ^p	796.1 ^q	1.4

^{a-s} : Tukey mean comparison within each oil type over temperature range (95 % Confidence) no significant difference between values sharing same letter.

2.3.2.2. Surface tension

Surface tension was modelled as a function of temperature using the semi-empirical Eötvös equation (Eq. 2.9) (Palit, 1956; Restolho et al., 2009). It is necessary to know the value of critical temperature of oil and the molecular weight to make predictions using Eötvös equation. Eötvös constant (K_E) is the measure of entropy of the surface and its value was calculated using the method of least squares. The experimental and predicted data were observed to follow a similar trend with increase in temperature (Fig. 2.5). For all the oils used in the study, K_E of 6.2 dynes·cm/mol^{2/3}·K fit the data using the KRÜSS goniometer and K_E of 5.9 dynes·cm/mol^{2/3}·K fit the data using the ramé-hart goniometer. Same Eötvös constant values could be used to fit the data for all oils studied with one equipment. The Eötvös constant depends on the geometry of the molecule and the similarity in values irrespective of oil type was as expected. The difference in Eötvös constant with respect to equipment was mainly because of the differences in numerical method used for surface tension calculation by the equipment, which affected the fit of the model. Models presented in the manuscript are from the data obtained using the KRÜSS goniometer.

The predicted values and error (E %) at the temperatures at which experiments were conducted for all five oils used in the study are reported in Table 2.10. The error was less than ten percent for all five oils at the temperature range studied; this was true for predicted values compared with data obtained from both equipment when using their corresponding K_E . According to the data, the Eötvös equation has a higher accuracy of prediction of surface tension between 60 - 100 °C, as the error was less than five percent in this temperature range for all five oils. Overall, the Eötvös equation overestimates the surface tension value at lower temperatures (23 and 40 °C) and underestimates the surface tension at higher temperatures (140 - 200 °C). Surface tension was also modeled using a combination of Eötvös and modified Rackett equation (Fig. 2.5). The model can help to predict the values of surface tension of oils at high temperature if the free fatty acid composition, density and critical parameters of the oil are known.

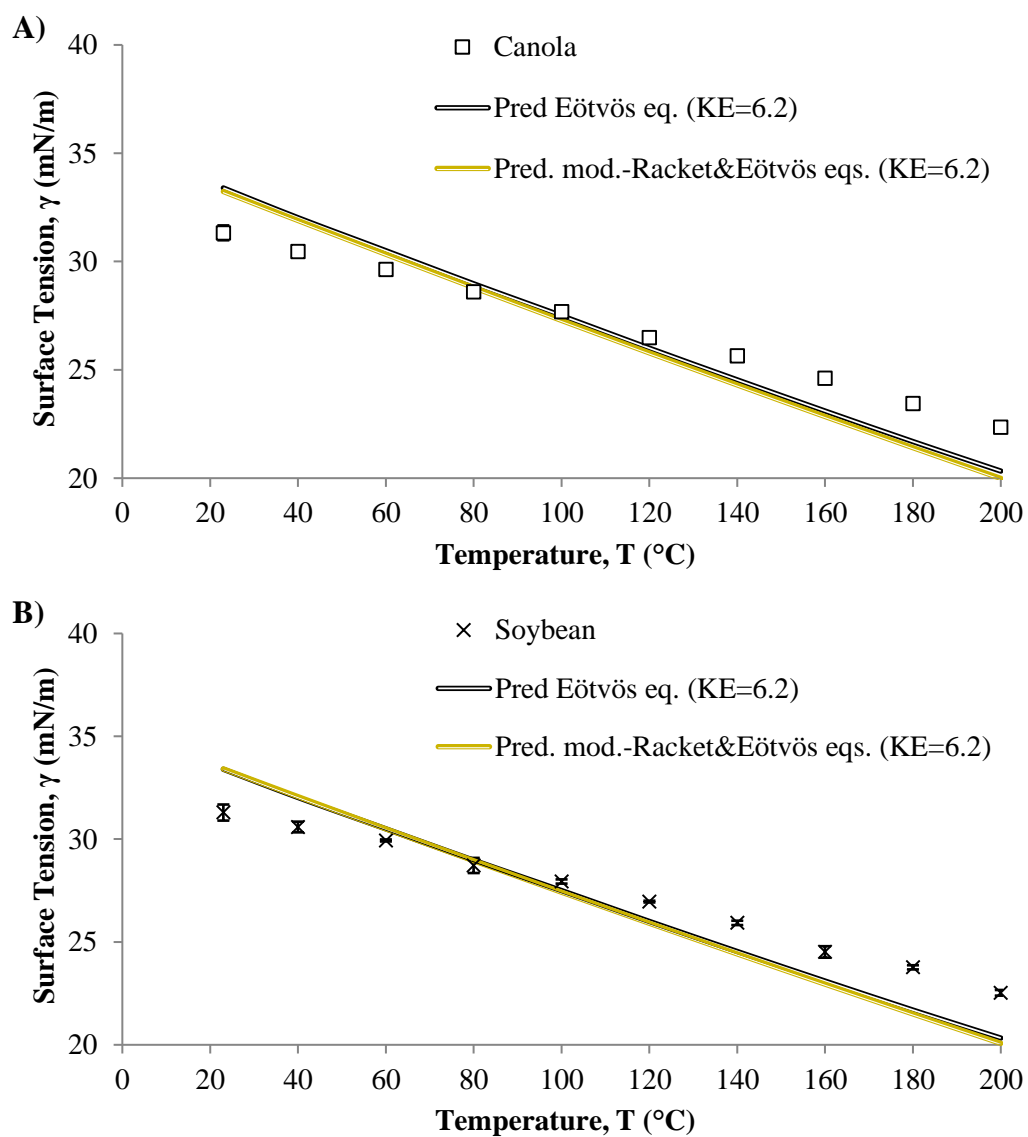


Fig. 2.5. Comparison between surface tension experimental values obtained by KRÜSS goniometer of A) Canola oil, and B) Soybean oil and their corresponding predicted values by the Eötvös equation and the modified Racket- Eötvös equation

Table 2.10. Predicted surface tension values for each vegetable oil by the Eötvös equation ($KE = 6.2 \text{ dynes}\cdot\text{cm}/\text{mol}^{2/3}\cdot\text{K}$) and their corresponding percentage error comparing with experimental data obtained using KRÜSS goniometer

T (°C)	Canola oil			Corn oil			Olive oil			Peanut oil			Soybean oil		
	γ_{oil} (mN/m)		E %												
	EXP	PRED		EXP	PRE D		EXP	PRED		EXP	PRED		EXP	D	
23															
± 1	31.3 ^b	33.4 ^a	6.6	31.6 ^c	33.6 ^a	6.3	31.9 ^b	33.3 ^a	4.3	31.3 ^c	33.3 ^a	6.2	31.3 ^c	33.6 ^a	7.3
40	30.5 ^c	32.0 ^b	5.1	30.7 ^d	32.2 ^b	4.8	30.9 ^c	32.0 ^b	3.6	30.3 ^d	31.9 ^b	5.0	30.6 ^d	32.2 ^b	5.2
60	29.6 ^d	30.5 ^c	2.9	29.7 ^e	30.6 ^d	3.3	30.0 ^d	30.4 ^d	1.4	29.7 ^e	30.3 ^d	2.0	29.9 ^e	30.6 ^d	2.4
80	28.6 ^e	29.0 ^e	1.3	28.5 ^g	29.1 ^f	2.2	28.8 ^e	28.9 ^e	0.2	28.8 ^f	28.8 ^f	0.1	28.7 ^f	29.1 ^f	1.3
100	27.7 ^f	27.5 ^f	0.7	27.7 ^h	27.6 ^h	0.4	27.7 ^f	27.4 ^f	1.0	27.7 ^g	27.3 ^h	1.3	27.9 ^g	27.6 ^g	1.3
120	26.5 ^g	26.0 ^h	1.9	26.4 ⁱ	26.1 ^j	1.3	26.6 ^g	25.9 ^h	2.6	26.5 ⁱ	25.9 ^j	2.6	27.0 ^h	26.1 ⁱ	3.2
140	25.6 ^h	24.5 ⁱ	4.3	25.3 ^k	24.6 ^l	2.6	25.7 ^h	24.4 ⁱ	4.7	25.5 ^h	24.4 ^k	4.4	25.9 ⁱ	24.7 ^j	4.9
160	24.6 ⁱ	23.1 ^j	6.1	24.1 ^m	23.2 ⁿ	3.7	24.3 ⁱ	23.0 ^j	5.3	24.5 ^k	23.0 ^l	6.0	24.5 ^j	23.2 ^l	5.2
180	23.5 ^j	21.7 ^l	7.5	23.0 ⁿ	21.8 ^p	5.4	23.1 ^j	21.6 ^k	6.6	23.0 ^l	21.6 ^m	6.3	23.8 ^k	21.8 ⁿ	8.3
200	22.4 ^k	20.3 ^m	9.0	22.0 ^o	20.4 ^q	7.5	—	—		21.3 ^m	20.2 ⁿ	5.1	22.5 ^m	20.4 ^o	9.5

^{a-p}: Tukey mean comparison within each oil type over temperature range (95 % Confidence) no significant difference between values sharing same letter.

2.3.2.3. Viscosity

Viscosity of the oils was modelled up to 200 °C using the modified Andrade equation (Eq. 2.10). The coefficients a , b and c were obtained using regression analysis. The Andrade equation is a form of the Arrhenius equation and uses kinematic viscosity values to establish relation between viscosity and temperature. Conversions between dynamic and kinematic viscosities is given by Eq. 2.13.

$$\mu = \nu\rho \quad \text{Eq. 2.13}$$

where ν is the kinematic viscosity (mm^2/s), μ is the kinematic viscosity ($mPa \cdot s$), and ρ the density (g/cm^3) at the selected temperature.

The values of a , b and c were obtained using method of least squares (Table 2.11). Similar trends to previous studies (Esteban et al., 2012; Noureddini et al., 1992b; Yilmaz, 2011) were observed in the current study using a different assembly. According to the data, there is a high degree of accuracy between the experimental and the predicted data as the error was less than ten percent for all the temperatures used in the study (Table 2.12). The error percentage increased with increasing temperature, however the experimental and predicted data had similar trends for change in viscosity with temperature (Fig. 2.6).

Table 2.1. Parameters a , b and c corresponding to the modified Andrade equation used to predict the viscosity of each vegetable oil

Oil type	a	b	c	Temp range (°C)
Canola	-0.40	-478.44	545692.29	23 - 200
Corn	0.46	-804.36	560589.98	23 - 200
Olive	0.09	-771.31	603521.93	23 - 180
Peanut	0.47	-1065.63	654506.48	23 - 200
Soybean	1.23	-1466.38	686086.16	23 - 200

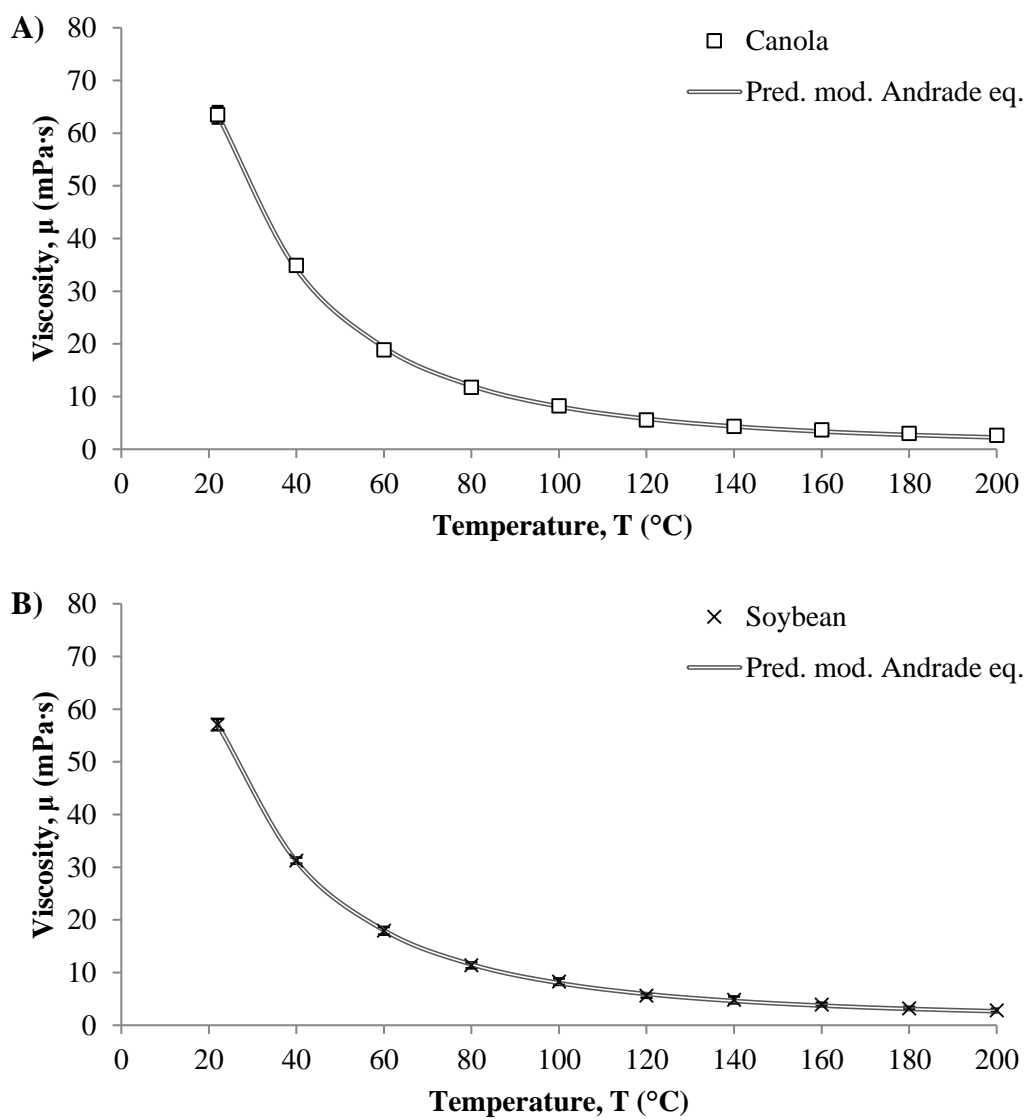


Fig. 2.6. Comparison between viscosity experimental values of A) Canola oil, and B) Soybean oil and their corresponding predicted values by the modified Andrade equation

Table 2.11. Predicted dynamic viscosity values for each vegetable oil by the modified Andrade equation and their corresponding percentage error

T (°C)	Canola oil			Corn oil			Olive oil			Peanut oil			Soybean oil			E %				
	μ_{oil} (mPa·s)		E %	μ_{oil} (mPa·s)		E %	μ_{oil} (mPa·s)		E %	μ_{oil} (mPa·s) PRE		E %	μ_{oil} (mPa·s)		E %					
	EXP	PRED		EXP	PRED		EXP	PRED		EXP	D		EXP	PRED						
23 ±																				
1	63.5 ^a	63.5 ^a	0.0	59.2 ^a	59.5 ^a	0.5	74.1 ^a	74.3 ^a	0.2	72.2 ^a	72.4 ^a	0.3	57.1 ^a	57.1 ^a	0.1					
40	34.9 ^b	34.2 ^b	2.1	34.5 ^b	33.5 ^c	3.0	40.1 ^b	39.3 ^b	1.9	38.8 ^b	38.0 ^c	2.1	31.3 ^b	31.1 ^b	0.5					
60	18.8 ^c	19.4 ^c	2.7	19.1 ^e	19.8 ^d	3.8	21.1 ^c	22.0 ^c	3.9	20.5 ^e	21.1 ^d	3.0	17.9 ^c	18.0 ^c	0.5					
80	11.8 ^d	12.0 ^d	2.3	12.5 ^f	12.9 ^f	3.0	13.4 ^d	13.6 ^d	1.8	12.6 ^f	13.1 ^f	3.2	11.4 ^d	11.5 ^d	1.6					
100	8.2 ^e	8.1 ^e	1.3	9.0 ^g	9.0 ^g	0.3	9.6 ^e	9.1 ^e	4.9	8.8 ^g	8.7 ^g	0.6	8.3 ^e	8.0 ^e	3.2					
120	5.5 ^f	5.8 ^f	4.2	6.4 ^h	6.6 ^h	2.7	6.1 ^f	6.5 ^f	6.2	6.1 ^h	6.3 ^h	2.9	5.6 ^f	5.9 ^f	5.2					
140	4.4 ^g	4.3 ^g	0.9	5.1 ⁱ	5.1 ⁱ	0.2	4.8 ^g	4.9 ^g	0.4	4.8 ⁱ	4.7 ⁱ	1.4	4.8 ^g	4.6 ^{g,h}	4.2					
160	3.7 ^{g,h}	3.4 ^{h,i}	7.8	4.3 ^j	4.1 ^j	4.4	4.0 ^{g,h}	3.8 ^{g,h}	5.8	4.0 ^j	3.7 ^j	7.6	3.9 ^{h,i}	3.7 ^{ij}	4.9					
180	3.0 ^{h,i,j}	2.7 ^{ij}	9.6	3.5 ^k	3.4 ^k	2.7	3.3 ^h	3.1 ^h	7.1	3.1 ^k	3.0 ^k	2.7	3.2 ^{ij,k}	3.1 ^{jk}	3.4					
200	2.6 ^{ij}	2.2 ^j	14.7	3.1 ^{k,l}	2.9 ^l	8.8	—	—	—	2.7 ^k	2.5 ^k	7.0	2.8 ^k	2.7 ^k	5.2					

^{a-l}: Tukey mean comparison within each oil type over temperature range (95 % Confidence) no significant difference between values sharing same letter.

2.4. Conclusions

Based on the results, temperature had a significant effect on all three physical properties of oil measured. Oil type was shown to have a significant effect on viscosity and density but did not influence surface-tension. Surface tension and density decreased linearly with increasing temperature, whereas the decrease in viscosity followed a power law model. The trends for all the three physical properties were similar to those reported in literature and thus results could be corroborated. Mathematical models built to predict the change in surface tension (the Eötvös equation and modified Rackett- Eötvös equations), density (the modified Rackett equation), and viscosity (the modified Andrade equation) seemed to agree well with the experimental data. The error percentage for mathematical models increased with increasing temperature, however the error was less than 15 % for all the three mathematical models developed. The mathematical models developed can thus be used to predict the change in physical properties of oil at high temperatures; specially for controlling process parameters during frying, spray drying, dairy processing or atomization during biodiesel production. Understanding of transport rate of oil at high temperatures (up to 200 °C) when different types oils are used can be used for varied applications such as a better/more accurate prediction of the oil absorption rates during frying and understanding of drying rate during spray drying.

2.5. Acknowledgement

We would like to thank the center for Advanced Processing and Packaging studies (CAPPS) for providing funding for this research. We would also like to thank Dr. Owen Jones, Dr. Oswaldo Campanella and Dr. Cordelia Running for granting us access to use the equipment and facilities in their lab.

2.6. References

- Adamson, A. W., and Gast, A. P. (1967). Physical chemistry of surfaces, 150, p. 180.
- Aydar, A.Y., Rodriguez-Martinez, V., Farkas, B.E. (2016). Determination and modeling of contact angle of canola oil and olive oil on a PTFE surface at elevated temperatures using air or steam as surrounding media. LWT - Food Science and Technology, 65, 304-310.
- Bouchon, P. (2009). Understanding oil absorption during deep-fat frying, in: Steve, L.T. (Ed.), Advances in food and nutrition research, pp. 209-234.

- Bouchon, P., Pyle, D.L. (2005a). Modelling oil absorption during post-frying cooling: I: Model development. *Food and Bioproducts Processing*, 83(4), 253-260.
- Bouchon, P., Pyle, D.L. (2005b). Modelling oil absorption during post-frying cooling: II: Solution of the mathematical model, model testing and simulations. *Food and Bioproducts Processing*, 83(4), 261-272.
- Chang, S.S., Peterson, R.J., Ho, C.-T. (1978). Chemical reactions involved in the deep-fat frying of foods. *Journal of American Oil Chemists' Society*, 55(10), 718-727.
- Choe, E., Min, D.B. (2007). Chemistry of deep-fat frying oils. *Journal of Food Science*, 72(5), R77-R86.
- Dana, D., Saguy, I.S. (2006). Review: Mechanism of oil uptake during deep-fat frying and the surfactant effect-theory and myth. *Advances in Colloid and Interface Science*, 128-130, 267-272.
- Esteban, B., Riba, J.-R., Baquero, G., Rius, A., Puig, R. (2012). Temperature dependence of density and viscosity of vegetable oils. *Biomass and Bioenergy*, 42, 164-171.
- Farkas, B.E., Singh, R.P., Rumsey, T.R. (1996). Modeling heat and mass transfer in immersion frying. I, model development. *Journal of Food Engineering*, 29(2), 211-226.
- Flock, D.L., Le, T.H., Gibeau, J.P. (1986). The effect of temperature on the interfacial tension of heavy crude oils using the pendant drop apparatus. *Journal of Canadian Petroleum Technology*, 25(02).
- Halvorsen, J.D., Mammel, W.C., Jr., Clements, L.D. (1993). Density estimation for fatty acids and vegetable oils based on their fatty acid composition. *Journal of American Oil Chemists' Society*, 70(9), 875-880.
- Hubbard, L.J., Farkas, B.E. (2000). Influence of oil temperature on convective heat transfer during immersion frying. *Journal of Food Processing and Preservation*, 24(2), 143-162.
- Huygens, R.J.M., Boersma, D.M., Ronde, H., Hagoort, J. (1995). Interfacial tension measurement of oil-water-steam systems using image processing techniques. *SPE Advances Technology Series*, 3(01), 129-138.
- Kalogianni, E.P., Karapantsios, T.D., Miller, R. (2011). Effect of repeated frying on the viscosity, density and dynamic interfacial tension of palm and olive oil. *Journal of Food Engineering*, 105(1), 169-179.
- Kim, J., Kim, D.N., Lee, S.H., Yoo, S.-H., Lee, S. (2010). Correlation of fatty acid composition of vegetable oils with rheological behaviour and oil uptake. *Food Chemical*, 118(2), 398-402.
- Kochhar, S.P. (2000). Stabilisation of frying oils with natural antioxidative components. *European Journal of Lipid Science and Technology*, 102(8-9), 552-559.
- Mellema, M. (2003). Mechanism and reduction of fat uptake in deep-fat fried foods. *Trends in Food Sci and Technology*, 14(9), 364-373.
- Miller, K.S., Singh, R.P., Farkas, B.E. (1994). Viscosity and heat transfer coefficients for canola, corn, palm, and soybean oil. *Journal of Food Processing and Preservation*, 18(6), 461-472.

- Moreira, R.G., Sun, X., Chen, Y. (1997). Factors affecting oil uptake in tortilla chips in deep-fat frying. *Journal of Food Engineering*, 31(4), 485-498.
- Moreno, M.C., Bouchon, P. (2008). A different perspective to study the effect of freeze, air, and osmotic drying on oil absorption during potato frying. *Journal of Food Science*, 73(3), E122- E128.
- Noureddini, H., Teoh, B.C., Davis Clements, L. (1992a). Densities of vegetable oils and fatty acids. *Journal of American Oil Chemists' Society*, 69(12), 1184-1188.
- Noureddini, H., Teoh, B.C., Davis Clements, L. (1992b). Viscosities of vegetable oils and fatty acids. *Journal of American Oil Chemists' Society*, 69(12), 1189-1191.
- Palit, S.R. (1956). Thermodynamic interpretation of the Eötvös constant. *Nature*, 177(4521), 1180-1180.
- Restolho, J., Mata, J.L., Saramago, B. (2009). On the interfacial behavior of ionic liquids: Surface tensions and contact angles. *Journal of Colloid and Interface Science*, 340(1), 82-86.
- Saguy, I.S., Dana, D. (2003). Integrated approach to deep fat frying: Engineering, nutrition, health and consumer aspects. *Journal of Food Engineering*, 56(2-3), 143-152.
- Spencer, C.F., Danner, R.P. (1972). Improved equation for prediction of saturated liquid density. *Journal of Chem and Engineering. Data*, 17(2), 236-241.
- USDA-FAS (2015). Oilseeds: World markets and trade, in: *Analysis, O.o.G. (Ed.)*.
- White, J.L. (1959). Liquid densitometry, in: Bockris, J.O.M., White, J.L., Mackenzie, J.D. (Eds.), *Physicochemical measurements at high temperatures*. Academic Press, Inc., pp. 193-213.
- Xu, T., Rodriguez-Martinez, V., Sahasrabudhe, S.N., Farkas, B.E., Dungan, S.R. (2017). Effects of temperature, time and composition on food oil surface tension. *Food Biophysics*, 12(1), 88-96.
- Yamada, T., Gunn, R.D. (1973). Saturated liquid molar volumes. Rackett equation. *Journal of Chem and Engineering Data*, 18(2), 234-236.
- Yilmaz, N. (2011). Temperature-dependent viscosity correlations of vegetable oils and biofuel-diesel mixtures. *Biomass and Bioenergy*, 35(7), 2936-2938.
- Ziaifar, A.M., Achir, N., Courtois, F., Trezzani, I., Trystram, G. (2008). Review of mechanisms, conditions, and factors involved in the oil uptake phenomenon during the deep-fat frying process. *International Journal of Food Science and Technology*, 43(8), 1410-1423.

3. EFFECT OF FRYING OIL DEGRADATION ON SURFACE TENSION AND WETTABILITY ²

Frying oil degrades via exposure to heat, oxygen and water resulting in the formation of volatile and non-volatile products, which act as surface active substances and change heat and mass transfer rates. Effects of oil degradation during frying were quantified by measuring viscosity, surface tension, and static and dynamic contact angles of fresh oil (Total polar materials, TPM 3 - 4 %) and used oils (TPM 10 - 20 %). Oil viscosity decreased exponentially with increasing temperature (40 - 200°C). Used oil viscosity was higher than fresh oil at room temperature; no significant difference was recorded above 60°C. Pendant drop technique was used to measure air-oil (24 - 200°C) and steam-oil (100 - 200°C) surface tension of all oil samples. Surface tension decreased linearly as temperature increased. There was no effect of surrounding medium (air or steam) or oil quality on surface tension. Surface tension was time independent for both oils, as observed with a 5 h. measurement using rising-bubble technique. Static contact angles of all used oils were lower than fresh oil, indicating increased wettability of used oil, which can affect amount of oil absorbed during frying and post-fry cooling. Hysteresis of used oil (13° - 15°) was lower than fresh oil (18°), which can impact drainage during post-fry cooling.

Keywords: High temperature, properties, absorption, heat transfer, drainage

3.1. Introduction

Frying is the process of cooking food by immersing it in hot oil around 180°C (Bouchon, 2009; Farkas et al., 1996). Frying causes changes in the flavor, color, texture, and nutritional quality of foods (Dana and Saguy, 2006), yielding products which have a porous and crispy outer layer with a soft interior (Oreopoulou, et al., 2006). During frying, there are three main types of chemical reactions which cause oil degradation; hydrolysis, oxidation, and thermal degradation (Paul and Mittal, 1996; White, 1991). These reactions result in the formation of volatile and non-volatile degradation products such as free fatty acids, aldehydes, ketones, diglycerides,

² Reprinted from Shreya N. Sahasrabudhe, Jennifer A. Staton, Brian E. Farkas, Effect of frying oil degradation on surface tension and wettability, LWT, Volume 99, 2019, Pages 519-524, ISSN 0023-6438, <https://doi.org/10.1016/j.lwt.2018.10.026>.

monoglycerides, monomers, dimers and oligomers (Ziaifar et al., 2008). Some of the degradation products are surface active substances, which can potentially lower the surface tension of frying oil (Kalogianni et al., 2009). Changes in physical properties of oil can be used as indicators of chemical degradation. Hence, it is important to understand the changes in oil physical properties at frying temperatures to predict their effect on heat and mass transfer. Past studies have shown that viscosity decreases exponentially with increasing temperature (Coupland and McClements, 1997; Esteban et al., 2012; Kalogianni et al., 2009; Nouredini et al., 1992; Sahasrabudhe et al., 2017). Kalogianni et al. (2009) and Silva and Singh (1995) found an increase in oil viscosity with repeated frying at high potato to oil ratios. However, these studies were conducted at temperatures lower than the frying process. Differences in oil viscosity need to be studied at high temperatures to make accurate predictions on the effect of oil quality during frying.

Surface tension (ST) plays a key role in mechanisms of oil uptake (Dana and Saguy, 2006; Moreno and Bouchon, 2008; Sahasrabudhe et al., 2017). According to the surfactant theory of frying, surface active substances formed during frying are responsible for changes in rate of heat and mass transfer due to changes in water-oil ST (Blumenthal and Stier, 1991; Farkas and Hubbard, 2000; Kalogianni et al., 2009). Xu et al. (2017) found that air-oil ST is not affected by changes in oil composition when measured at room temperature. Kalogianni et al. (2011) found no difference in air-oil ST between fresh and used oil, when measured from room temperature to 50°C. However, the water-oil ST of used oil is significantly lower than fresh oil (Dana and Saguy, 2006; Kalogianni et al., 2011). During frying, oil is in continuous contact with steam, making it necessary to understand the change in ST of oil in contact with saturated and superheated steam. Nevertheless, there has been little published work on understanding the effect of oil degradation on steam-oil and air-oil tensions at frying temperatures. Formation of surfactants during frying affects the wettability between oil and food surfaces (Dana and Saguy, 2006), which in turn impacts the rate of heat and mass transfer during frying and post-fry cooling. The contact angle between oil and polystyrene surface decreases from 17.5 to 13.1° when measured against degraded oil (Silva and Singh, 1995). The contact angle of sunflower oil on glass surface decreases from 23.6 to 22.8° with oil use (Rossi et al., 2009). Dana and Saguy (2006) however, did not find a change in contact angle on a Teflon surface with oil use. These results have contradictory findings on the effect of oil quality on wettability but are not comparable since they use non-standard

techniques. Furthermore, the principles governing changes in surface wettability are not explained in the aforementioned studies. Hence, further studies are necessary to quantify the effect of oil degradation during frying on food-oil wettability.

In addition to the effect of oil degradation on static contact angle, it is also important to understand the effect on contact angle hysteresis. Liquids can interact with solids resulting in liquid adsorption or retention on the surface, leading to contact angle hysteresis (Lam et al., 2001). Timmons and Zisman (1966) concluded that hysteresis occurs mainly because the advancing drop moves over a hydrophobic surface free of water; the receding drop, on the other hand, moves over a composite hydrophobic-hydrophilic surface in which the intermolecular pores are saturated with water. Besides surface activity (Chaudhuri and Paria, 2009), liquid molecular weight (Lam et al., 2001) is also known to affect the degree of hysteresis. Thus, contact angle hysteresis is a function of both liquid and solid properties (Eral et al., 2013), and the change in hysteresis with oil degradation needs to be understood. Droplet motion on an inclined surface is a balance between the gravitational driving force and the resisting force (Eral et al., 2013), and is related to the contact angle hysteresis. Drainage of oil from a food surface during post frying cooling is a function of rolling or pinning ability of a droplet on a surface. However, very few studies explain the dynamics of three-phase contact line motion with oil degradation.

There is a significant gap in knowledge on the effect of oil degradation on physical properties of oil, especially at frying temperatures. Most studies are conducted at room temperatures or use non-standard techniques rendering them non-comparable. Furthermore, the physiochemical mechanisms that govern changes in oil properties are not explained. Understanding effects of oil properties on the rate of heat and mass transfer during frying and post-fry cooling requires measuring oil properties with standard techniques at temperatures of interest. Hence, the aim of the current study is to understand the effect of oil quality on viscosity and ST at high temperatures, and surface wettability at room temperature.

3.2. Materials and Methods

Clear liquid canola frying oil (Bunge, NY, USA) was obtained from Purdue dining court for the study. Fresh oil was collected at day 0 directly from the oil container. Used frying oils were collected at day 2, 4, 7, 10 and 13 of the frying cycles. Oil was used to fry potato products for 12 h. per day at $170 \pm 3^\circ\text{C}$ with a total load of 900 kg per week. The capacity of the fryer was 20 kg

of oil and was used to fry 2.5 kg potato products/ batch. Fresh oil was added to the fryer at the end of each day to maintain the oil level. The results obtained are from triplicates of the oils collected from the same batch. The oil was stored at room temperature in amber bottles to minimize oxidation.

3.2.1. Total polar materials (TPM) measurement

Degradation of oil during frying was quantified by measuring the total polar content of fresh and used oils with Testo 270 (Testo Inc., Sparta, USA). The Testo 270 measures TPM content in frying oil based on dielectric constant of polar materials, and displays it as a percentage (Stier, 2004). The equipment was calibrated using reference oil provided by the manufacturer.

3.2.2. Viscosity measurement

Dynamic viscosity (μ) of fresh and used oils collected at different time points was measured from 40°C to 200°C using a Brookfield viscometer equipped with a thermo-container and programmable temperature controller (LV-DVIII, HT-60, HT-110FR respectively, Brookfield Engineering Laboratories, Inc., Middleboro, USA) as described by Sahasrabudhe et al. (2017). The heating profile for the temperature controller attached to the viscometer was set up as: heat from 20°C until 200°C in increments of 20°C and holding at each temperature for 5 min.

3.2.3. Measurement of air-oil surface tension (ST)

The surface tension of fresh and used canola oils was determined by the pendant drop method using a ramé-hart goniometer (Model 590, Succasunna, USA). An elevated temperature 1 ml syringe with a 22-gauge stainless steel needle (0.43 mm internal diameter) was used to form the drops inside an environmental chamber equipped with a temperature control system (P/N 100-11, P/N 100-10-20, P/N 100-10-12-22, and P/N 100-07 respectively; ramé-hart Instrument Co., Succasunna, USA), with air as the surrounding medium. The surface tension was measured using DropImage software as described by Sahasrabudhe et al. (2017).

3.2.4. Measurement of steam-oil surface tension

Controlled temperature steam was added to the environmental chamber through a pipe connected to a steam source (Erlenmeyer flask with boiling water). The pipe was wrapped with proportional–integral–derivative (PID) controlled heating tape and thermal insulation to increase the temperature beyond 100 °C and to prevent heat loss, respectively (Fig. 3.1). Continuous steam

supply to the chamber was ensured by monitoring the condensate coming out of the chamber through a tube. For saturated steam experiments, windows of the environmental chamber were heated using heat guns with temperature maintained $\geq 100^{\circ}\text{C}$, to prevent condensation (Fig. 3.1). Steam-oil surface tension was measured with saturated and superheated steam (10°C to 200°C), using the method described in section 3.2.3.

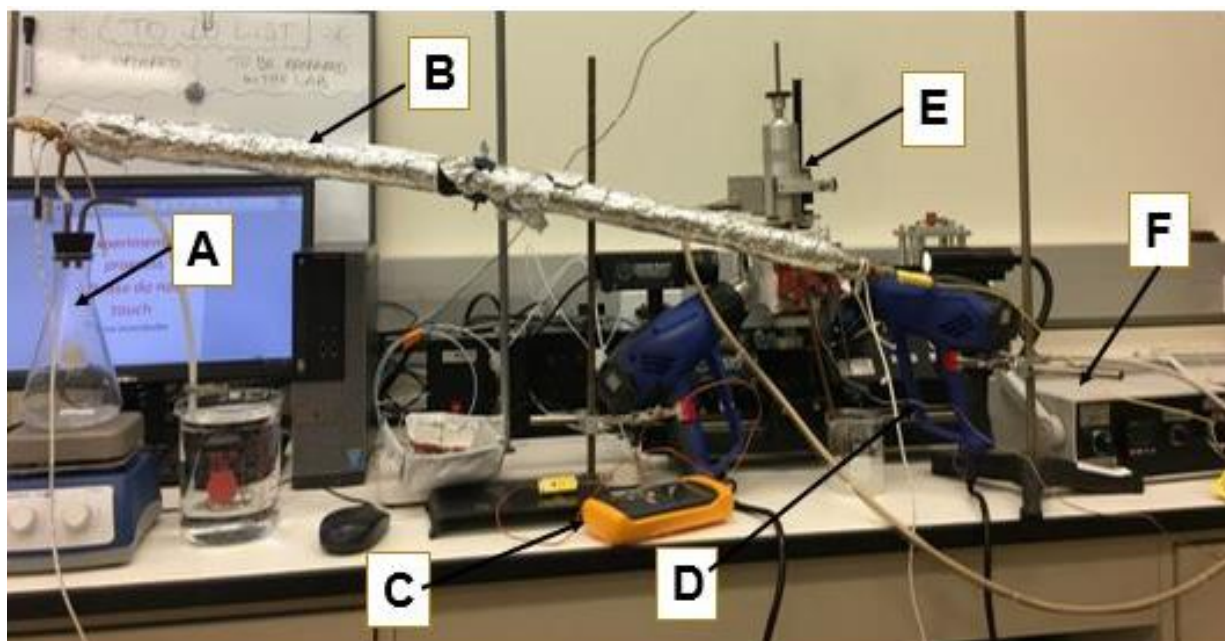


Fig. 3.1. Assembly for steam delivery for steam-oil and oil-air IFT measurements with the Ramé-Hart Goniometer

- A. Erlenmeyer flask
- B. Insulated copper pipe for steam delivery
- C. Probe for steam temperature monitoring
- D. Heat guns
- E. Insulated environmental chamber and elevated temperature syringe
- F. Temperature controller for chamber and syringe

3.2.5. Measurement of dynamic air-oil surface tension

Dynamic surface tension measurements for used and fresh oil samples were obtained with Teclis drop-profile tensiometer (Model Tracker S; Longessaigne, France). For each experiment, the sample was dispensed into a quartz cuvette and placed in the path of a collimated light beam that was positioned opposite a CCD camera. A rising air bubble was quickly formed in oil using a stainless-steel J-shaped needle; volume of the bubble ($4\ \mu\text{L}$) was maintained with the aid of the

WDROP software provided by Teclis. Silhouette images of the rising air bubble were captured with the CCD camera and shape of the interface was used to determine ST over time by comparison with Young-Laplace equation. All measurements were performed in triplicate with an accuracy of 0.1 mN/m and the average of the three trials is shown.

3.2.6. Contact angle measurements

Static, advancing and receding contact angles of fresh and used oils were measured on a Teflon surface at room temperature using a ramé-hart goniometer, equipped with an automated dispensing system (P/N 100-22, ramé-hart Instrument Co., Succasunna, USA). Measurements were made using volume of liquid method (Fig. 3.5) on DropImage Advanced software. Teflon was chosen as it is a relatively non-wetting surface with oil, making the dynamic angle measurements feasible. The Teflon sheet was cut into pieces (26 x 7 mm) and placed on the goniometer stand as described by Aydar et al. (2016). Disposable tips were used while changing liquids, and the volume (recorded as step numbers) was controlled using contact angle tools on the software. A drop of 3 μL was initially dispensed, and the baseline was adjusted to measure the static contact angle. For advancing angles, 0.25 μL oil was dispensed at each step. When constant values were obtained for the advancing angles, the mode was switched to receding and liquid was drawn back into the syringe at 0.08 $\mu\text{L}/\text{step}$ and 0.25 $\mu\text{L}/\text{step}$ (data not shown). The receding speed was adjusted to the lowest value possible to eliminate any viscous effects during the measurement. Parameters measured were drop height, base diameter, and contact angle (left, right, and mean). Contact angle hysteresis was calculated based on the difference between the mean advancing angle and the receding angle (measured when the contact line begins to retract- Fig. 3.6), similar to the procedure discussed by Grundke et al., 2015.

3.2.7. Statistical analysis

Measurements were performed in triplicate and data was analyzed using Minitab 17 (Minitab Inc., State College, USA). ANOVA of means with Tukey's HSD at $\alpha=0.05$ was performed on measured viscosity, surface tension and contact angle for the all the oil samples studied.

3.3. Results and Discussion

3.3.1. Total polar materials

For viscosity measurements, oil samples were collected on day 0 (fresh oil), 2, 4, 7, 10 and 13. The corresponding TPM value of fresh oil was 4 %, and that of the used oils were 10.5 %, 13.5 %, 13 %, 17 % and 20.5 % respectively. For tension measurements, oil samples were collected on day 0 (fresh oil), 2, 7, and 13. The corresponding TPM value of fresh oil was 4 %, and that of the used oils were 10.5 %, 12 % and 17 % respectively. For contact angle measurements, oil samples were collected on day 0 (fresh oil), 2, 4, 7, and 13. The corresponding TPM value of fresh oil was 3 %, and that of the used oils were 10.5 %, 13.5 %, 14.5 %, and 17 % respectively.

According to FDA regulations, the maximum percentage of polar compounds in used oil should be less than 25 % (Lalas, 2008). High TPM values in used oil indicate the presence of surface-active degradation products, formed as oil degrades during heating and cooling cycles. These polar materials are amphiphilic molecular structures which may affect oil ST. Total polar materials (TPM) are used by industry as an indicator of oil quality. Bansal et al. (2010) showed strong correlation (0.88-0.99) between TPM as measured by Testo 265 and analytical total polar compound measurement based on 95 % confidence interval. In the current study, TPM values of oil samples were used as indicators of oil degradation. These values were then correlated with oil physical properties to understand effect of oil degradation on physical properties.

3.3.2. Dynamic Viscosity

Viscosity of fresh and used oils showed Newtonian behavior over the range of temperatures studied. Regardless of the oil type, there was an exponential decrease in viscosity as temperature increased (Fig. 3.2), which agrees well with results from literature (Coupland and McClements, 1997; Esteban et al., 2012; Kalogianni et al., 2009; Miller et al., 1994; Sahasrabudhe et al., 2017). Statistical analysis using Tukey's test showed a higher viscosity of used oil from room temperature to 60°C, for all time points collected compared to fresh oil. When the temperatures increased beyond 60°C, there was no significant difference ($p > 0.05$) between viscosities of all oils. Thus, there is no difference in viscosity at frying temperatures. However, high viscosity of used frying oils at lower temperatures may affect rate of oil drainage during post-fry cooling.

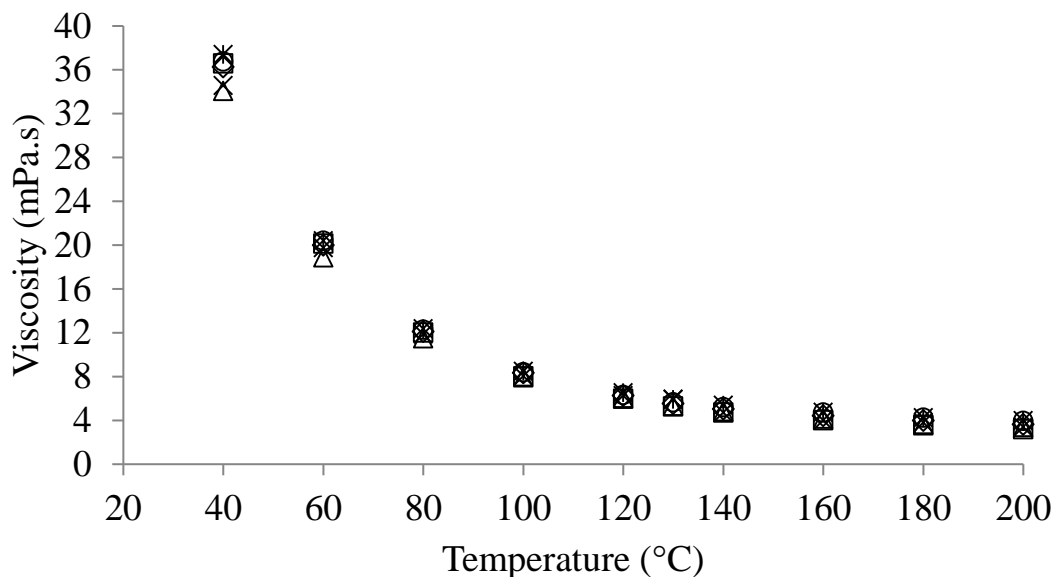


Fig. 3.2. Viscosity as a function of temperature averaged over 3 runs as oil quality is degraded with frying. Samples analyzed were fresh oil (Δ), and used oils collected on day 2 (\times), day 4 (\diamond), day 7 (\square), day 10 (\circ), day 13 ($*$) of the frying cycle

3.3.3. Surface tensions (ST)

Surface tension of each oil decreased linearly as temperature increased, from room temperature to 200°C, regardless of the surrounding medium (Fig. 3.3). Surface tension (γ_{LG}) of fresh oil was similar to vegetable oil values reported in literature (Sahasrabudhe et al., 2017; Xu et al., 2017). There was no significant effect ($p > 0.05$) of the medium on ST (100-200°C), when each oil was tested against air or steam (Fig. 3.3). O'Meara (2012) did not find any effect of the surrounding medium (air or steam) on the surface tension of five vegetable oils when measured from room temperature to 200°C, which supports the data from the present study. There was no difference ($p > 0.05$) in ST between fresh and used oils from room temperature to 160°C which agrees with the findings of Kalogianni et al., 2011 and Xu et al., 2017. When the temperature increased beyond 160°C, ST of used oils (TPM 10-18 %) was lower ($p < 0.05$) than fresh oil (TPM 4 %). To test the time dependency of surface tension, rising bubble data was obtained. Surface tension remained unchanged ($p > 0.05$) for fresh (TPM 4 %) and used oil (TPM 12 %) at room temperature when measured for 5 h (Fig. 3.4). This indicates that the lower ST observed at higher temperatures during the pendant drop measurements, was not a diffusion-controlled phenomenon. Time independency of food oil ST was also reported by Xu et al., 2017. In the current paper, only

the data for used oil (TPM 12 %) compared with fresh oil against air and steam was reported. However, surface tension of used frying oils with TPM 10.5 % and TPM 17 % also followed the same trend (data not shown).

The surface tension of fresh and used oil is similar at room temperature because the amphiphilic molecules lack surface activity at concentrations present in used oils to affect ST for an air-oil interface (Xu et al., 2017). However, at high concentrations (≥ 15 mole % of triglycerides), amphiphilic compounds may lower oil ST (Xu et al., 2017). It is hypothesized that at high temperatures, due to increased molecular mobility and molecular surface coverage of these amphiphiles (Berman et al., 2015), a lower concentration may cause change in ST. Hence, ST differences between fresh and used oil are observed only at high temperatures. It should be noted that although the ST between fresh and used oil is statistically different, the differences are not significant enough to affect the frying process.

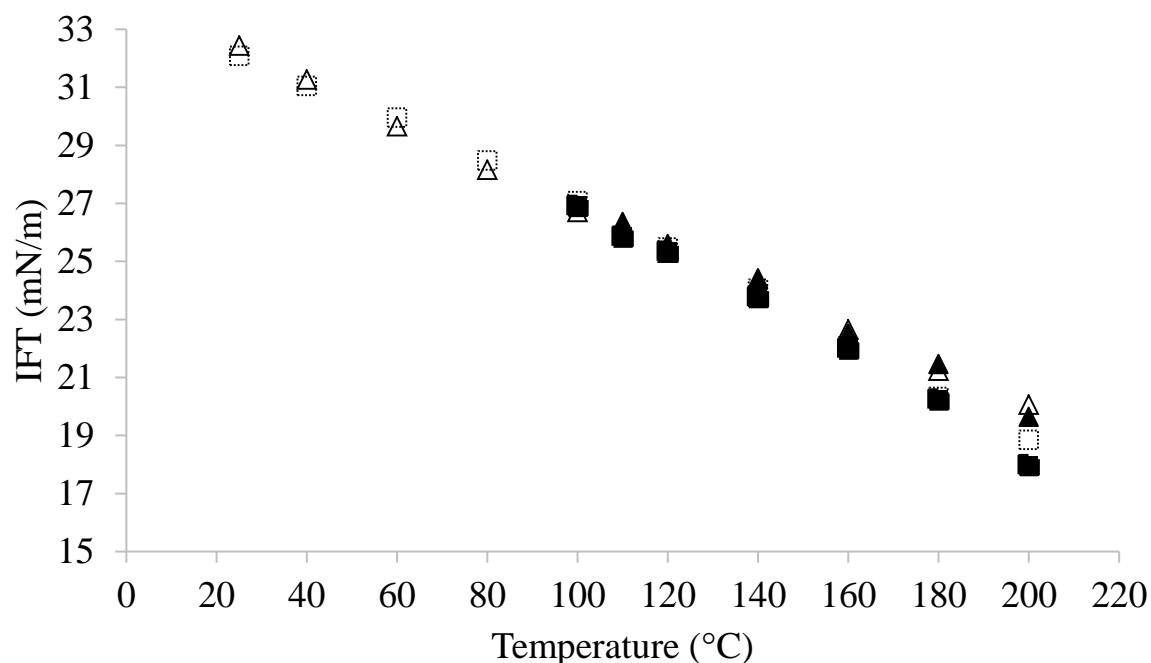


Fig. 3.3. Equilibrium surface or interfacial tension values averaged over 3 runs for fresh (Δ , \blacktriangle) and used oil (TPM 12%) (\square , \blacksquare) oils from room temperature to 200°C with steam (\blacktriangle , Δ) and air (Δ , \square) as the surrounding medium.

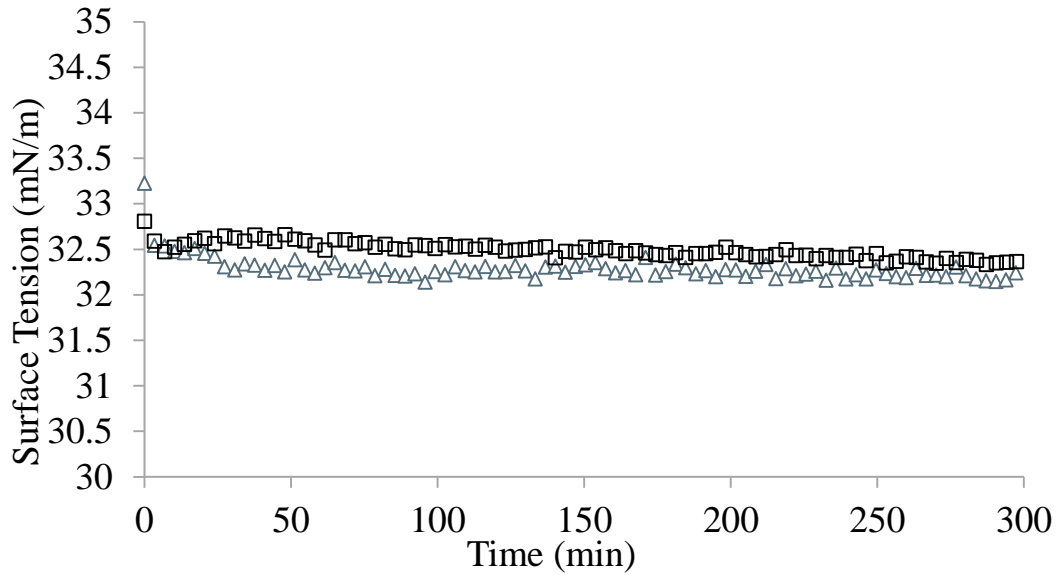


Fig. 3.4. Surface tension as a function of time at 22°C for fresh (\triangle) and used oil (TPM 12) (\square) averaged over 3 runs in the rising bubble configuration using the Teclis drop-profile device. Air was used for the gas phase.

3.3.4. Contact angle

Static contact angle (θ_e) was measured when an oil drop was initially deposited on the Teflon surface (Fig. 3.5a). The static contact angle of fresh oil was $62.0 \pm 0.35^\circ$, and of used oils were $57^\circ - 60^\circ$ (Table 3.1). The results indicate increased surface wettability with used oil compared to fresh oil. The contact angle values progressively decreased with increasing TPM values, indicating increased wettability with increased use of frying oil. Pyter et al., 1982 observed unequal rates of adsorption of surfactants between solid-liquid and liquid-vapor interfaces and attributed the effect to differences in surface polarity. In the current experiment, the presence of polar compounds was indicated by higher TPM of used oil. The solid-liquid interfacial tension (IT) is a combination of London dispersion forces and induced dipole interactions based on Debye interaction energy (Carré, 2007) (Eq. 3.1).

$$\gamma_L(1 + \cos\theta_e) = 2\sqrt{\gamma_S^D\gamma_L^D} + k_s\gamma_L^P \quad \text{Eq. 3.1}$$

where γ_L is the total surface free energy, γ_S^D is the dispersive component of the surface free energy of solid, γ_L^D and γ_L^P are the dispersive and polar components of the surface free energy respectively measured at water-oil interface, k_s is the surface polarizability of the solid.

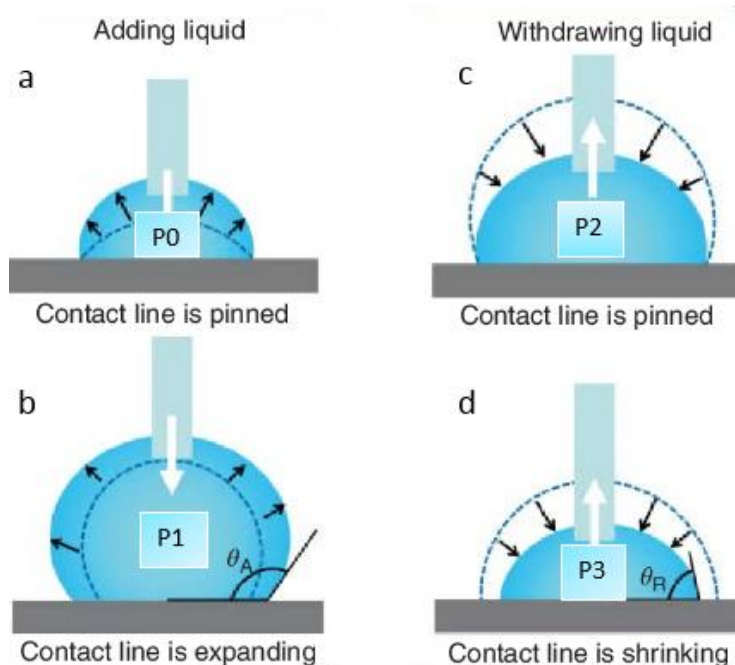


Fig. 3.5. Illustration of stages of drop behavior during measurement of advancing (adding liquid) and receding (withdrawing) contact angles using volume of liquid method adapted from (Ras et al., 2017).

Table 3.1. Comparison of contact angle between used oils (TPM 10-17) and fresh oil (TPM 3) on a PTFE surface at room temperature.

Oil Age	TPM (%)	Angle (°)			
		Static	Advancing	Receding	Hysteresis
Fresh	3	62.0±0.35 ^a	62.6±0.61 ^a	44.2±0.44 ^{ab}	17.7±0.26 ^a
Day 2	10.5	60.5±0.34 ^b	59.9±0.77 ^b	44.9±0.36 ^a	15.2±0.39 ^b
Day 4	13.5	58.9±0.52 ^c	58.0±0.84 ^c	44.7±0.67 ^a	13.5±0.49 ^c
Day 7	14.5	58.4±0.25 ^{cd}	58.2±0.65 ^c	44.6±3.45 ^a	13.4±0.51 ^c
Day 13	17	57.4±0.43 ^d	57.7±0.72 ^c	44.5±0.37 ^a	13.1±0.38 ^c

±: corresponds to the standard deviation, n=3.

^{a-c}: Tukey mean comparison per parameter (95 % Confidence) no significant difference between values sharing same letter.

It is hypothesized that polar compounds in used oil induced polarity to the Teflon surface, thus increasing k_s and reducing the contact angle value. The mechanism of induced polarity can explain the reason for no change in air-oil surface tension, but a decrease in contact angle. The effect is less pronounced on a weak polarizing material such as Teflon (Davis, 1977; Polymer

Dielectric Materials), and increases as polarizability of the material increases (Davis, 1977). The variable polarizability of the contact surface may be the reason for contradictory effects reported in literature on fresh and used oil contact angles. Increased used oil wettability led to increased force of adhesion, as calculated using Young-Duprê equation (Eq. 3.2) (Chaudhuri and Paria, 2009; Schrader, 1995, Malcolm, 1995). This would result in higher adhesion of used oil on a food surface, thus affecting drainage during post-fry cooling.

$$W_A = \gamma_{SG} - \gamma_{SL} + \gamma_{LG} = \gamma_{LG}(1 + \cos\theta_e) \quad \text{Eq. 3.2}$$

where W_A is the work of adhesion, γ_{SL} is the solid-liquid IT, γ_{SG} is the solid-gas ST, approximately zero.

Dynamic contact angle was measured to understand the effect of oil degradation on the motion of an oil film as it wets and de-wets a solid surface (Fig. 3.6). The change of drop base diameter is an indicator of the three-phase contact line motion. Based on the motion of the sessile drop, the dynamic angle data was divided into three domains as described by Lam et al., 2001. In the first domain (period P1, Fig. 3.5b), base diameter increased with increasing drop volume, but contact angle remained constant. This stage lasted from step 0 of the experiment until step s_m (Fig. 3.6). The angle in this domain was denoted as the mean advancing contact angle. The second domain (period P2, Fig. 3.5c) was characterized by transition from advancing to receding contact angle. The contact line remained pinned to the surface, whereas contact angle decreased. This stage lasted from step s_m to step s_n (Fig. 3.6). This was followed by the third domain (period P3, Fig. 3.5d) where contact angle remained relatively constant, but the base diameter decreased continuously. This stage lasted from step s_n to the measurement's end (Fig. 3.6). The receding angle value was obtained at step s_n , when the base began to recede. This practice is adopted because of stick slip effect during receding angle measurements which causes contact-line periphery slips and leads to discrete changes in drop base diameter and contact angle (Lam et al., 2001; Lam et al., 2002). The contact angle hysteresis was calculated from the difference between mean advancing angle (0- s_m) and the angle corresponding to step s_n (Eq. 3.3).

$$H = \sum_0^{s_m} \bar{\theta}_a - \theta_r \quad \left(\frac{dr}{ds} < 0 \right) \quad \text{Eq. 3.3}$$

where H is the contact angle hysteresis, $\bar{\theta}_a$ is the mean advancing angle, dr is the change in drop base diameter, ds is the step change, $dr/ds < 0$ represents the step number corresponding to s_n in Fig. 3.6, where the base diameter of the drop begins to decrease.

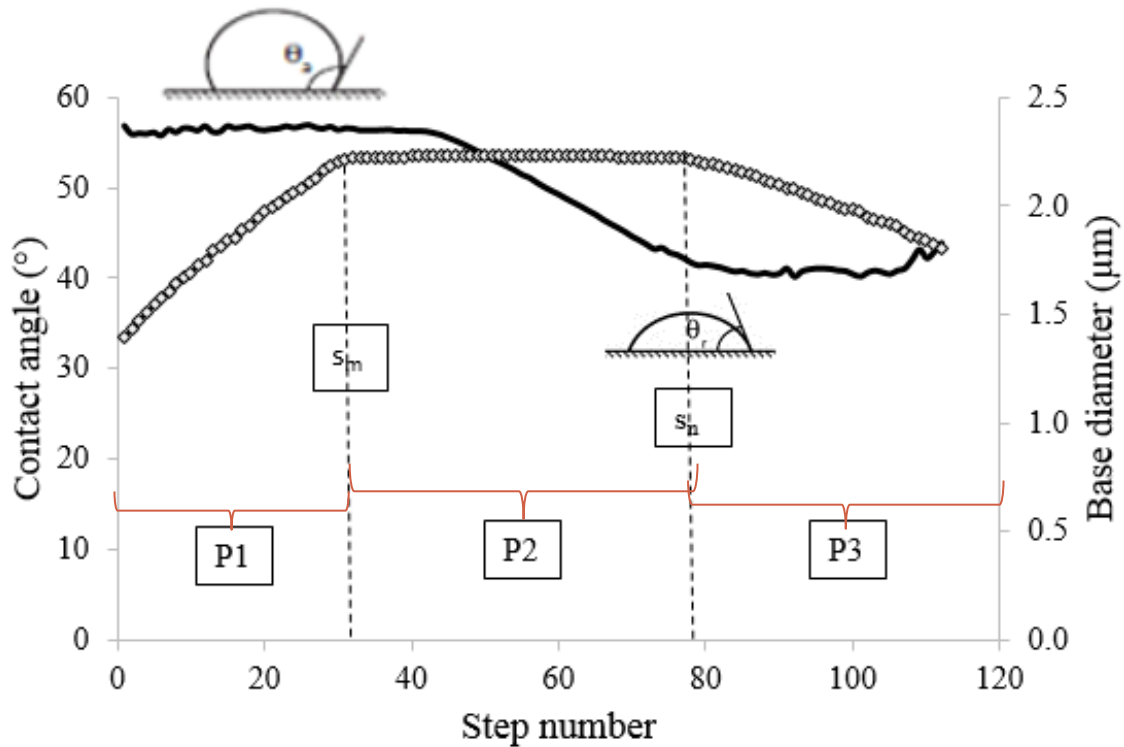


Fig. 3.6. Contact angle (-) and base diameter (\diamond) of fresh oil at room temperature as a function of step number. Each step denotes increase in drop volume at the rate of $0.25 \mu\text{L}/\text{step}$ for advancing contact angle measurement and decrease in volume at the rate of $0.08 \mu\text{L}/\text{step}$ for receding contact angle measurement. s_m corresponds to the step the when the there is no change in drop base diameter, s_n corresponds to the step change when the base of the drop begins to decrease.

The lag period after s_m (when the angle and base diameter are constant) was attributed to differences in the advancing and receding volume changes at each step. During this lag phase, drop height changed while the angle and drop diameter remained constant. When the same rate was used for advancing and receding measurements, the lag phase was not experienced (data not

shown). Pinning of the drop is a result of adhesion forces between liquid and the surface due to surface defects or liquid adsorbed on the surface (Eral et al., 2013; Timmons and Zisman, 1966). When the ST force becomes larger than adhesion, contact line is set in motion again (Eral et al., 2013).

Contact angle hysteresis was $17.7 \pm 0.26^\circ$ for fresh oil and $13^\circ - 15^\circ$ for used oils (Table 3.1). Both oils followed the same path for advancing and receding contact angles (Fig. 3.7). Increased wettability of used oils compared to fresh oil was confirmed by lower values of advancing angle for all used oil samples collected. These observations are similar to previous results for alkanes and alcohols on silicon wafers by Lam et al. (2001), and for water on Teflon by Grundke et al. (2015). The stability in advancing angle values (step 0-40, Fig. 3.7) confirms surface smoothness. The decrease in contact angle (step 45-70, Fig 3.7) with constant drop diameter is an effect of contact line pinning due to liquid retention/penetration in the monolayer cavities of the polymer, and adsorption of the liquid on the surface, as the liquid moves over areas already wet during advancing stages (Lam et al., 2001, 2002; Timmons and Zisman, 1966).

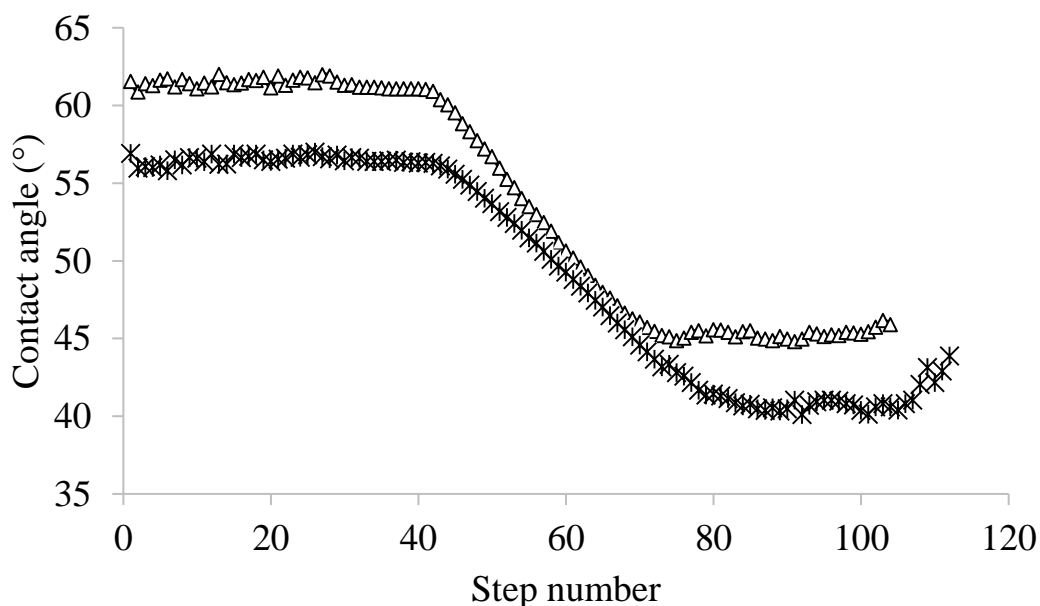


Fig. 3.7. Contact angles of fresh (\triangle) and used (TPM 17) ($*$) oil averaged over 3 runs as a function of step number measured at room temperature.

Lam et al., 2002 found that increase in molecular weight/longer chain length of alkanes led to decreased hysteresis because of decreased penetration in monolayer cavities of polymers. In the

current study, lower hysteresis was observed in used oil compared to fresh oil (Table 3.1). Frying leads to the formation of oil polymers due to thermal polymerization (Choe and Min, 2007) which increase the mean molecular weight of used oil (Abidi and Warner, 2001). Thus, increased oil molecular weight leads to decrease in adsorption capacity and hysteresis. Increased wettability and decreased hysteresis with used oil can impact the amount of oil absorbed by the food during frying and post-fry cooling. As most of the oil absorption occurs during the cooling stage (Bouchon, 2009), it is important to understand the physical principles governing wettability and hysteresis of oil drainage on a food surface and may be a subject of further investigation.

3.4. Conclusion

The aim of the current study was to understand the impact of oil degradation during frying on physical properties of oil. Higher TPM values of used oils compared to fresh oil were indicative of the presence of amphiphilic compounds in used oils. Based on the effect of oil physical properties on heat flux during frying, viscosity and surface tension work against one another as oil is degraded. While oil degradation does not affect viscosity at frying temperatures, increased viscosity was observed at room temperature which may affect drainage during post-fry cooling. Improved wettability and decreased hysteresis may impact heat and mass transfer during frying, the motion of oil into food and the rate of drainage during post-fry cooling; these need to be studied further.

3.5. Acknowledgment

The authors would like to thank Rituraj Borgohain and Dr. Jozef Kokini for letting us access to use equipment's in their lab. The authors also acknowledge the contribution of Oliver David Chamorro Ojeda for assistance in data collection; Dr. Owen Jones and Dr. Stephanie Dungan for their inputs in interpreting the results from the study.

3.6. Funding source

This project was supported by AFRI Grant no. 2014-67017-21831 from the USDA National Institute of Food and Agriculture, Improving Food Quality – A1361

3.7. References

- Abidi, S. L., and Warner, K. (2001). Molecular-weight distributions of degradation products in selected frying oils. *Journal of American Oil Chemists' Society*, 78, 763–769.
- Aydar, A., Rodriguez-Martinez, V., and Farkas, B. (2016). Determination and modeling of contact angle of Canola oil and olive oil on a PTFE surface at elevated temperatures using air or steam as surrounding media. *LWT - Food Science and Technology*, 65, 304–310.
- Bansal, G., Zhou, W., Barlow, P. J., Joshi, P., Neo, F. L., and Lo, H. L. (2010). Evaluation of commercially available rapid test kits for the determination of oil quality in deep-frying operations. *Food Chemical*, 121(2), 621–626.
- Berman, P., Meiri, N., Colnago, L. A., Moraes, T. B., Linder, C., Levi, O., Wiesman, Z. (2015). Study of liquid-phase molecular packing interactions and morphology of fatty acid methyl esters (biodiesel). *Biotechnology for Biofuels*, 8 (1), 12.
- Blumenthal, M. M., and Stier, R. F. (1991). Optimization of deep-fat frying operations. *Trends in Food Science and Technology* 2, 144–148.
- Bouchon, P. (2009). Understanding oil absorption during deep-fat frying. *Advances in Food and Nutrition Research*, 57, 209–234.
- Carré, A. (2007). Polar interactions at liquid/polymer interfaces. *Journal of Adhesion Science and Technology*, 21, 961–981.
- Chaudhuri, R. G., and Paria, S. (2009). Dynamic contact angles on PTFE surface by aqueous surfactant solution in the absence and presence of electrolytes. *Journal of Colloid and Interface Science*, 337, 555–562.
- Choe, E., and Min, D. B. (2007). Chemistry of deep-fat frying oils. *Journal of Food Science*, 72, R77–86.
- Coupland, J. N., and McClements, D. J. (1997). Physical properties of liquid edible oils. *Journal of American Oil Chemists' Society*, 74, 1559–1564.
- Dana, D., and Saguy, I. S. (2006). Mechanism of oil uptake during deep-fat frying and the surfactant effect-theory and myth. *Advances in Colloid and Interface Science*, 128–130, 267–272.
- Davis, B. W. (1977). Estimation of surface free energies of polymeric materials. *Journal of Colloid and Interface Science*, 59, 420–428.
- Eral, H. B., Mannelje, and Oh, J. M. (2013). Contact angle hysteresis: a review of fundamentals and applications. *Colloid and Polymer Science*, 291, 247–260.
- Esteban, B., Riba, J.-R., Baquero, G., Rius, A., and Puig, R. (2012). Temperature dependence of density and viscosity of vegetable oils. *Biomass and Bioenergy*, 42, 164–171.
- Farkas, B. E., and Hubbard, L. J. (2000). Analysis of convective heat transfer during immersion frying. *Drying Technology*, 18, 1269–1285.
- Farkas, B. E., Singh, R. P., and Rumsey, T. R. (1996). Modeling heat and mass transfer in immersion frying. I, model development. *Journal of Food Engineering*, 29, 211–226.

- Grundke, K., Pöschel, K., Synytska, A., Frenzel, R., Drechsler, A., Nitschke, M., Welzel, P. B. (2015). Experimental studies of contact angle hysteresis phenomena on polymer surfaces toward the understanding and control of wettability for different applications. *Advances in Colloid and Interface Science*, 222, 350–376.
- Kalogianni, E. P., Karastogiannidou, C., and Karapantsios, T. D. (2009). Effect of the Presence and Absence of Potatoes under Repeated Frying Conditions on the Composition of Palm Oil. *Journal of American Oil Chemists' Society*, 86, 561–571.
- Kalogianni, E.P., Karapantsios, T. D., and Miller, R. (2011). Effect of repeated frying on the viscosity, density and dynamic interfacial tension of palm and olive oil. *Journal of Food Engineering*, 105, 169–179.
- Lam, C. N. C., Kim, N., Hui, D., Kwok, D. Y., Hair, M. L., and Neumann, A. W. (2001). The effect of liquid properties to contact angle hysteresis. *Colloids and Surfaces A: Physicochemical and Engineering Aspects*, 189, 265–278.
- Lam, C. N. C., Wu, R., Li, D., Hair, M. L., and Neumann, A. W. (2002). Study of the advancing and receding contact angles: liquid sorption as a cause of contact angle hysteresis. *Advances in Colloid and Interface Science*, 96, 169–191.
- Malcolm E. S. (1995). Young-Dupre Revisited, *Langmuir*, 11, 3585–3589.
- Miller, K. S., Singh, R. P., and Farkas, B. E. (1994). Viscosity and heat transfer coefficients for canola, corn, palm, and soybean oil. *Journal of Food Processing and Preservation*, 18(6), 461-472.
- Moreno, M. C., and Bouchon, P. (2008). A different perspective to study the effect of freeze, air, and osmotic drying on oil absorption during potato frying. *Journal of Food Science*, 73, E122-128.
- O'Meara, Meghan (2012). Determination of the Interfacial Tension between Oil-Steam and Oil-Air at Elevated Temperatures (Master's thesis). Retrieved from NCSU library repository. <https://repository.lib.ncsu.edu/handle/1840.16/8150>.
- Oreopoulou, V., Krokida, M., and Marinos-Kouris, D. (2006). Frying of foods In Mujumdar A. S. (Eds.), *Handbook of Industrial Drying* (pp. 1204-1223), CRC Press, Boca Raton.
- Noureddini, H., Teoh, B. C., and Clements, L. D. (1992). Viscosities of vegetable oils and fatty acids. *Journal of American Oil Chemists' Society*, 69, 1189–1191.
- Paul, S., and Mittal, G. S. (1996). Dynamics of fat/oil degradation during frying based on physical properties. *Journal of Food Process Engineering*, 19, 201–221.
- Polymer Dielectric Materials, <https://www.intechopen.com/books/dielectric-material/polymer-dielectric-materials>. Accessed May 20, 2018
- Pyter, R., Zografis, G., and Mukerjee, P. (1982). Wetting of solids by surface-active agents: The effects of unequal adsorption to vapor-liquid and solid-liquid interfaces. *Journal of Colloid and Interface Science*, 89, 144–153.
- Ras, R. H., Tian, X., and Bayer, I. S. (2017). Superhydrophobic and superoleophobic nanostructured cellulose and cellulose composites. *Handbook of Nanocellulose and Cellulose Nanocomposites*, 2, 731-760.

- Rossi, M., Alamprese, C., Ratti, S., and Riva, M. (2009). Suitability of contact angle measurement as an index of overall oil degradation and oil uptake during frying. *Food Chemical*, 112, 448–453.
- Sahasrabudhe, S. N., Rodriguez-Martinez, V., O'Meara, M., and Farkas, B. E. (2017). Density, viscosity, and surface tension of five vegetable oils at elevated temperatures: Measurement and modeling. *International Journal of Food Properties*, 20, sup2, 1965–1981.
- Lalas S. (2008). Quality of Frying Oil in Servet G. S., and Serpil S. (Eds.), *Advances in Deep-Fat Frying of Foods* (pp. 57-81), CRC Press. Boca Raton.
- Silva, M. G. D., and Singh, R. P. (1995). Viscosity and surface tension of corn oil at room temperature. *Journal of Food Processing and Preservation*, 19, 259–270.
- Stier, R. F. (2004). Tests to monitor quality of deep-frying fats and oils. *European Journal of Lipid Science and Technology*, 106, 766–771.
- Timmons, C. O., and Zisman, W. A. (1966). The effect of liquid structure on contact angle hysteresis. *Journal of Colloid and Interface Science*, 22, 165–171.
- White, P. J. (1991). Methods for measuring changes in deep-fat frying oils. *Food Technology*, 45(2), 75.
- Xu, T., Rodriguez-Martinez, V., Sahasrabudhe, S. N., Farkas, B. E., and Dungan, S. R. (2017). Effects of Temperature, Time and Composition on Food Oil Surface Tension. *Food Biophysics*, 12, 88–96.
- Ziaifar, A. M., Achir, N., Courtois, F., Trezzani, I., and Trystram, G. (2008). Review of mechanisms, conditions, and factors involved in the oil uptake phenomenon during the deep-fat frying process. *International Journal of Food Science and Technology*, 43, 1410–1423.

4. EXPERIMENTAL MEASUREMENT OF FACTORS AFFECTING DYNAMICS OF BUBBLE GROWTH FROM A SUBMERGED ORIFICE: APPLICATIONS TO THE FRYING PROCESS³

Frying can be described as a conjugate boiling problem, which involves submersing a food material in oil heated to temperatures above the boiling point of the water within the food material. The food material acts as a vapor generating matrix, where water is lost by evaporation in the form of bubbles formed in hot oil at the food's surface. Change in process variables including oil temperature, and solid and liquid physicochemical properties can affect bubble dynamics during frying. Understanding the effect of these parameters on bubble diameter, frequency and number of nucleation sites can facilitate prediction of overall heat and mass transfer rates during frying. Hence, the aim of the present study was to experimentally examine the impact of oil quality, temperature, orifice diameter and surface wettability on bubble dynamics and develop hypotheses to qualitative describe the impact on heat and mass transfer rates.

Keywords: bubble dynamics, frequency, volume, heat transfer, wettability, temperature

4.1. Introduction

Hydrodynamics of bubble growth and rise through a liquid play an important role in chemical, petrochemical, nuclear, metallurgical and biomedical industries. A submerged bubble assembly (Fig. 4.1) has been used for studying formation, interaction and coalescence of bubbles in gas-liquid contactors, gas-liquid separators, boiling process, bubble columns, fermenters, and cavitation systems (Zhang and Shoji, 2001). Bubble formation is controlled by six major forces: stabilizing forces of surface tension, viscous drag and inertia, and destabilizing forces of pressure, buoyancy, and momentum (Bari and Robinson, 2013; Pioro et al., 2004; Ramakrishnan et al., 1969). Bubble formation is divided into three principle stages: nucleation, growth and detachment (Fig. 4.3a) (Ramakrishnan et al., 1969; Yu et al., 2015). The angle at triple contact point between the gas bubble, liquid and solid surface changes continuously during bubble formation and is

³ Reprinted from Shreya N. Sahasrabudhe, Shreyas S. Chaudhari, Brian E. Farkas, Experimental measurement of factors affecting dynamics of bubble growth from a submerged orifice: Applications to the frying process, Journal of Food Engineering, Volume 251, 2019, Pages 36-44, ISSN 0260-8774, <https://doi.org/10.1016/j.jfoodeng.2019.02.005>.

denoted as dynamic contact angle (Bari and Robinson, 2013). The angle changes from obtuse during the nucleation stage to acute during the elongation stage to 90° during necking, thus marking the three stages of bubble formation (Bari and Robinson, 2013). During nucleation, the bubble dome grows due to continuous gas inflow, but the base remains attached to the orifice. During growth/elongation stage, base of the bubble contracts and the bubble obtains a hemispherical shape. For a wettable surface, elongation stage ends when stabilizing forces are equal to the buoyancy force. For a non-wettable surface, bubble grows as the dynamic contact angle decreases until it reaches the equilibrium contact angle value (Phan et al., 2009). During this mode of behavior, base of the bubble expands, until stabilizing forces balance destabilizing forces (Chesters, 1978; Yuan et al., 2014). This is an additional stage in non-wetting fluids, which occurs due to effect of high equilibrium contact angle. During detachment/pinch-off stage, total destabilizing force is higher than stabilizing force, leading to a neck formation and eventual detachment of the bubble from the orifice (Yuan et al., 2014). For boiling behavior on a superhydrophobic surface, Teodori et al. (2016) observed that there is no interfacial component to cause bubble detachment. Hence the bubble stays attached to the surface and coalesces in the horizontal direction forming an insulating vapor blanket from which a single bubble detaches.

Based on flow rates, bubble dynamics can be divided into three regimes: static, dynamic and turbulent. In the static regime, bubble volume is independent of gas flow rate; formation time increases as flow rate decreases (Ramakrishnan et al., 1969; Simmons et al., 2015). In the dynamic regime, bubble volume increases with increase in flow rate; formation time approaches a limiting value (Simmons et al., 2015). In turbulent regime, there is bubbling chaos and bubbles coalesce above the nucleation site (Simmons et al., 2015).

Bubble volumes and bubble frequency depends on the liquid properties such as density, viscosity and surface tension; surface properties such as wettability and roughness; as well as operating conditions such as flow rate and orifice diameter (Gerlach et al., 2007; Ramakrishnan et al., 1969). At low flow rates, capillary force and buoyancy are main forces acting on the bubble. Hence, effect of viscosity is negligible. As the flow rate of gas increases, there is an increase in inertial and viscous forces which influence the rate of bubble expansion (Bari and Robinson, 2013; Gerlach et al., 2007; Ramakrishnan et al., 1969). The effect of viscosity on bubble volume is especially pronounced when gas is passing at a high flow rate through a small orifice, and fluid surface tension is low (Ramakrishnan et al., 1969). Liquid density does not affect bubble volume

for a highly viscous fluid when the gas is passing through a small diameter orifice at a low flow rate (Gerlach et al., 2007). Thus, the bubble volume and frequency are a function of fluid properties and interaction between the vapor, fluid and solid. Bari and Robinson, 2013; Islam et al., 2015; Simmons et al., 2015 have studied bubble formation characteristics in terms of dimensionless numbers such as Bond number (Bo) (Eq. 4.1) and Ohnesorge number (Oh) (Eq. 4.2) as described below.

$$Bo = \frac{\rho g d^2}{\gamma} \quad \text{Eq. 4.1}$$

$$Oh = \frac{\mu}{\sqrt{\gamma \rho d}} \quad \text{Eq. 4.2}$$

where μ is the dynamic viscosity, γ is the fluid surface tension, ρ is the fluid density, and d is the orifice diameter.

Bari and Robinson, 2013 found an inverse relation between bubble volume and Bond number. Islam et al., 2015 studied the effect of Bo in glycerin solutions on bubble volume and formation time. Bond number in this study was modified by changing the fluid surface tension. Bubble volume and formation time decreased with increase in Bo due to smaller neck elongation. However, at high Bo values (0.47), bubble volume and formation time increased, and was attributed to very low resistance of surrounding fluid to stopping the bubble's neck from rupturing near the orifice. Simmons et al., 2015 characterized the bubbling behavior in terms of Oh (Eq. 4.2). The study found that for a relatively small gas flow rate, change in Oh has very little influence on the formation time and thus on the bubble volume. When the flow rate increases, formation increases with decrease in Oh resulting in increase in bubble volume.

Frying can be described as a conjugate boiling problem, consisting of simultaneous heat and mass transfer between oil and food. During frying, the surrounding liquid phase is the heat source, with aqueous phase embedded in a quasi-porous matrix (Farkas and Hubbard, 2000). The bubble formation from one pore during frying can be approximated using the submerged orifice assembly (Fig. 4.1). Heat is transferred by convection from the hot oil to the food surface and by conduction from the surface of food to the core (Farkas et al., 1996). Thus, the food material acts as a vapor generating matrix; water is lost by evaporation in the form of bubbles formed in hot oil at the food's surface which control the rate of heat transfer during frying (Farkas and Hubbard, 2000; Hubbard and Farkas, 1999; Kalogianni et al., 2009). The convective heat transfer coefficient

shows a bell-shaped curve; reaching its peak value at a high rate of moisture loss when bubbling is observed (Safari et al., 2018). Heat transfer rate is minimum when the bubbling stops (Farinu and Baik, 2007; Mir-Bel et al., 2012; Safari et al., 2018). Thus, rate of heat transfer in frying is dependent on number of nucleation sites, bubble volume, velocity and frequency (Costa et al., 1999; Farinu and Baik, 2007; Farkas and Hubbard, 2000; Mir-Bel et al., 2012; Safari et al., 2018).

Nucleate boiling is a phase change process in which vapor bubbles are formed on a heated surface (Tong and Tang, 1997). The forces acting on the bubbles during boiling are the same as the forces described above. Bubble dynamics comprises of bubble growth and departure, as well as bubble release frequency, and number of nucleation sites (Dhir, 1998; Mikic and Rohsenow, 1969; Mohanty and Das, 2017), and controls heat transfer during nucleate boiling (Eq. 4.3). Factors such as surface roughness, viscosity, surface tension, fluid density, surface wettability, and thermal properties of solid affect bubble diameter and hence heat transfer rate (Eq. 4.4) (Dhir et al., 2007; Kandlikar, 2003; Kim, 2009; Mohanty and Das, 2017; Pioro et al., 2004).

$$q = \frac{K^2}{2} \sqrt{\pi(k\rho c_p)_l f} D_d^2 N_a \Delta T + \left(1 - \frac{K^2}{2} N_a \pi D_d^2\right) h_{nc} \Delta T + h_{ev} \Delta T N_a \frac{\pi}{4} D_d^2 \quad \text{Eq. 4.3}$$

$$D_d = C_{sf} \theta \sqrt{\frac{2\gamma}{g(\rho_l - \rho_g)}} \quad \text{Eq. 4.4}$$

where q is nucleate boiling heat flux, K and C are proportionality constants, k is thermal conductivity, c_p is specific heat at constant pressure, D_d is bubble diameter, ρ is density, f is bubble release frequency, N_a is number density of active sites, ΔT is temperature difference, h_{nc} is average heat transfer coefficients due to natural convection, h_{ev} is average heat transfer coefficients due to microlayer evaporation, C_{sf} is surface-fluid interaction constant, θ is contact angle, γ is surface tension, g is acceleration due to gravity, l and g are liquid and gas respectively.

Thus, the effect of solid and liquid properties on bubble dynamics need to be considered when estimating the overall heat transfer coefficient during boiling (Mohanty and Das, 2017; Pioro et al., 2004; Shekriladze, 2008). Based on the mechanisms and factors affecting heat transfer during boiling; frying is analogues to boiling, where bubbles evolve from food submerged in hot oil (Farkas and Hubbard, 2000).

Repeated use causes changes in frying oil surface tension and contact angle (Blumenthal and Stier, 1991; Dana and Saguy, 2007) due to the formation of free fatty acids, monoglycerides as well as polymers (Dana and Saguy, 2006). This in turn can affect bubble growth and escape.

Food products have different porosity, moisture content, surface roughness and wettability, which affects bubble dynamics (Costa et al., 1999). The increased heat flux with the use of degraded oil in frying can thus be associated with the boiling phenomenon (Costa et al., 1999; Farkas and Hubbard, 2000; Hubbard and Farkas, 1999). However, when oil viscosity becomes very high, heat transfer is shown to decrease (Farkas and Hubbard, 2000). Hence, it is important to experimentally determine the oil properties as well as food parameters affecting bubble formation which impact heat transfer during frying.

Hubbard and Farkas (1999) showed heat transfer due to bubble formation during frying was much greater than the free convection phase. Despite the importance of bubbling and bubble characteristics in frying (Farinu and Baik, 2007), there has been no fundamental study on understanding the impact of fluid and surface properties on bubble dynamics. Hence, the aim of this study was to understand the effect of oil quality, oil temperature, pore diameter and surface wettability on bubble dynamics using a simplified model system consisting of a single pore assembly submerged in oil. Based on the results from the parametric study, hypotheses were developed to qualitatively describe the impact of bubble dynamics on heat transfer rates as applicable to the frying process.

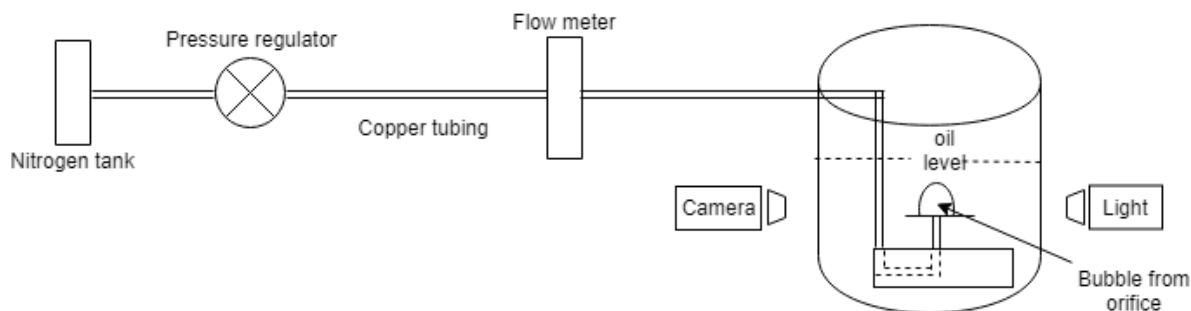


Fig. 4.1. Submerged orifice assembly to measure bubble dynamics

4.2. Materials and Methods

Frying oil (Canola, Bunge, NY, USA) was obtained from Purdue University dining court. Used oil was obtained after frying French fries in the oil for 2 weeks (12 hr. per day) at $170 \pm 3^\circ\text{C}$ with an average load of 1200 pounds of potato products per week. The results obtained are triplicates of the oil collected from the same batch. The oil was stored at room temperature in amber bottles to minimize oxidation.

4.2.1. Total polar materials (TPM) measurement

Degradation of oil by frying was quantified by measuring the total polar content of fresh and used oil (Testo 270, Testo Inc., Sparta, NJ) based on dielectric constant of polar materials (Stier, 2004). The equipment was calibrated using reference oil provided by the manufacturer.

4.2.2. Submerged orifice assembly set-up and image processing

An assembly (Fig. 4.1) was built to mimic the boiling stage of immersion frying. Pressurized nitrogen gas was supplied through an in-line regulator (625-04-04-01-00, Smith Equipment's, IN) to a flow meter (EW-32014-15- 65 MM, Cole-Parmer, IL), connected to an orifice submerged in oil. Flow rate (5 ml/min), was based on calculated flow rate of steam found during frying of potato slices (data not shown).

The orifice was submerged in a 1000 ml Pyrex beaker. The beaker was large enough that the influence of the side walls was negligible. The top of the beaker was covered with a PTFE lid to minimize surface oxidation during the experiment. The beaker was filled with 800 ml oil, to ensure that the liquid level was sufficient to prevent any environmental effects. Bubble growth and departure was studied from a single orifice with diameters between 100 μm -1 mm to understand the effect of pore size on bubble dynamics. Orifice diameters were measured on a microscope (DFC310 FX, Leica Microsystems, IL) at 40x zoom and analyzed using LAS 4.2 software equipped with a scale bar. The orifice sizes were selected to mimic the pore size distribution in a typical food matrix (potato slices) during frying. Stainless-steel and Teflon surfaces were used for testing, to understand the bubble development on a wettable and non-wettable surface, respectively. All experiments were conducted using fresh and used canola oil, to experimentally determine effect of oil quality on bubble formation during frying. Effects of temperature on bubble formation were determined by conducting experiments in oil at room temperature and 170 °C. Oil was heated to 170 °C using a hot plate. K-type thermocouple was inserted near the tip of the capillary. Temperature maintained manually within $170\pm 3^\circ\text{C}$ based on K-type thermocouple readings. The proper functioning and reproducibility of the assembly was tested by conducting experiments with a known fluid (water with and without 0.01M sodium dodecyl sulphate (SDS)).

A high-speed video camera (Photron FastCam) and 4x zoom, was used to record bubble behavior (at least three bubbles in a video), in the formation and ascendance processes. Images of 1024/580 pixel² were recorded at 2000 fps with a spatial resolution of 0.264 mm/pixel. A MATLAB code was written to determine the relevant bubble characteristics; bubble volume,

coordinates of the bubble interface, centroid, instantaneous contact angle, formation time, and frequency. The image processing steps and sequence were similar to the process described by Bari and Robinson (2013). Depending on the sample and exposure, parameters in the script were tuned to obtain well defined boundaries. Information on bubble formation stages was obtained by tracking the change in height of a single bubble at each frame as the bubble formed on the orifice. Volume was estimated using MATLAB with SolidWorks: MATLAB point cloud data of bubble boundaries to generate a 3D bubble model in SolidWorks. Dynamic angle was calculated by binarizing the video in MATLAB and processing each frame matrix using the following steps (Fig. 4.2): 1) tracing boundaries for orifice plate and axisymmetric bubble, 2) fitting a line to the orifice plate and bubble boundaries at the point of contact, using small curvature approximations, and 3) calculating the included angle between the fitted lines. Frequency was calculated by obtaining a cropped image from the video which displays only bubble boundaries. The matrix generated at each frame was then compared to the previous frame. A plot was generated from the matrix comparison which displayed the formation and lag time of the bubbles. Total time for bubbling was a summation of formation and lag time. Dynamic angle and frequency codes were then processed for the entire video length using LINUX on Purdue University supercomputer cluster with graphics display mode on. Output data generated from the dynamic angle code was compared with the frequency data to obtain information on effect of temperature, pore diameter, wettability and oil quality on bubble frequency as described in the results section.

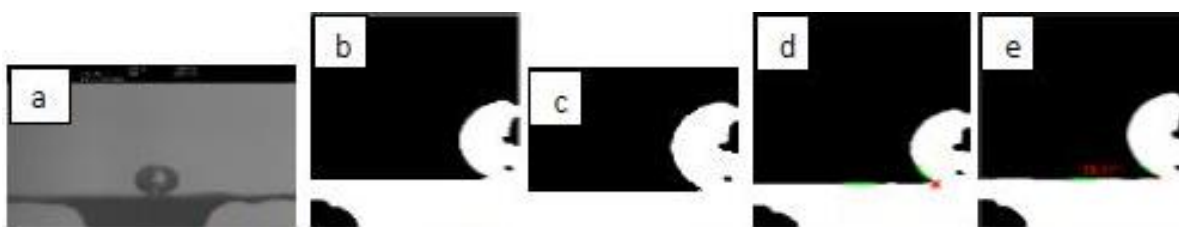


Fig. 4.2. Stages for image processing to calculate dynamic angle during bubble formation; a) original video, b) axisymmetric binary image, c) cropped bubble region, d) fitting lines to orifice plate and bubble boundaries, e) calculation of included angle

4.3. Uncertainty analysis

Uncertainty in temperature measurements was assessed using the method described by Teodori et al. (2016) (Eq. 4.5).

$$\Delta T = \sqrt{(U^2 + S^2)} \quad \text{Eq. 4.5}$$

where U is the uncertainty of the measurement instrument itself, which in this case is $\pm 1^\circ$ for the thermocouple and $\pm 1^\circ$ for the hot plate, and S is the standard deviation of the measurements.

The uncertainty associated was $\pm 2^\circ\text{C}$.

Uncertainty in flow rate measurement was based on deviation in flow meter reading of ± 0.1 ml/min. For the frequency and formation time uncertainty, these values were obtained by calculating the frames in the video captured and comparing it with the data generated from the video. The uncertainty in frequency estimation was ± 0.02 Hz.

Uncertainty estimation for the boundary detection was calculated for volume and contact angle separately; for volume estimation, volume of a known object was calculated using the code to account for the pixilation, the image was then blurred, and the volume was estimated again. The total uncertainty was between 12 - 15 % depending on the sharpness of the bubble boundary. For contact angle estimation, a similar procedure was followed using a semicircle with a known contact angle on a base. The total error estimation was 11 - 16 % based on the sharpness of the boundary.

4.4. Theory

Heat transfer during frying is similar to boiling (Farkas and Hubbard, 2000); studies have shown the importance of bubbling during heat transfer (Farkas and Hubbard, 2000; Safari et al., 2018). Studies by van Koerten et al. (2017) have developed relationships between heat transfer coefficient and bubbling based on calculated average bubble diameter and velocity for French fries. However, no study was found on the parametric effect of the fluid, process and food properties that affect bubble dynamics. These properties have been studied during boiling and the relationships are adapted to the frying process. However, during frying the rate of vapor generation is governed by the rate of heat flux through the crust. Hence, the effect of fluid, fluid/solid interaction and process variables need to be studied using pores submerged in oil at high temperatures to understand their effect on bubble formation, which is the objective of the current research.

4.5. Results and Discussion

Bubble volume and frequency were measured for experiments with distilled water and water with SDS; results were compared with literature data. The bubble volume was independent of flow rate confirming that the system was at quasi-steady state. The bubble volume decreased, and frequency increased when SDS was added to water. These results were used to test the proper functioning of the assembly (Fig. 4.1), as previous studies have shown decrease in bubble volume and increase in frequency as surface tension decreases (Chen et al., 2009; Gerlach et al., 2007; Ramakrishnan et al., 1969; Zahedi et al., 2014).

Bubble formation and ascendance was studied for oil using a constant flow rate (5 ml/min). The bubbling was at quasi steady state; bubble volume was independent of flow rate as shown by preliminary data (data not included). Bubble volume was dependent on temperature, orifice material and diameter, and oil quality as elaborated in the later sections.

Bubble formation during the process occurred in three stages (Fig. 4.3a), similar to descriptions in literature (Bari and Robinson, 2013; Yu et al., 2015). During stage 1- bubble nucleation: the bubble was shaped liked a spherical segment. The rate of change in bubble height was low during this stage, as the shape is primarily controlled by stabilizing viscous and surface tension forces. During stage 2- growth/elongation stage, the bubble dome attained a hemispherical shape, and the base of the bubble began to contract. Buoyancy force is an important force during this stage of formation and the rate of change of bubble height with time increases exponentially (Fig. 4.3b). The bubble formation then entered pinch-off stage (stage 3), when the bubble began to detach from the surface through neck formation.

Stages of growth during bubble formation were also accompanied by changes in dynamic contact angle at the three-phase contact line. The dynamic angle changed from obtuse to acute to 90° denoting the three formation stages (Fig. 4.3b). As the bubble emerged from the orifice, it formed an obtuse angle with the base (Fig. 4.3b- S1). This is the bubble nucleation stage. As the bubble volume increased, the angle rapidly decreased to an acute angle of about $30\text{-}50^\circ$ (Fig. 4.3b – S2), depending on the plate material, oil type and temperature. This is the growth/elongation stage, where buoyancy plays a dominant role in bubble shape. The angle then increased back to 90° (Fig. 4.3b- S3) due to neck formation before the bubble pinched off from the surface. Thus, the dynamic angle followed a U-shaped curve during the bubble formation stages (Fig. 4.3b) and agrees with data in literature for water (Bari and Robinson, 2013; Chen et al., 2009). The

processing of dynamic angle codes for consecutive bubbles provided information on the formation and lag time between bubbles. It is important to note that the bubble was pinned to the orifice during the formation process. Hence, the change in the angle value is representative of the change in bubble volume; the rate of change of contact angle is controlled by the liquid and surface properties.

Bubble frequency was calculated using the matrix comparison method as described in section 2.2. Formation time (t_f) is the time from bubble nucleation to when the bubble pinches off from the orifice. The lag time (t_l) is the time between formations of subsequent bubbles (Fig. 4.4d). Bubble frequency was then calculated (Eq. 4.6).

$$\text{Bubble frequency} = \frac{1}{[\text{Bubble formation time } (t_f) + \text{Lag time between bubble } (t_l)]} \quad \text{Eq. 4.6}$$

The lag time between bubbles was attributed to filling of the void created when bubble departs (Kim, 2009) and to the entering of oil inside the capillary forming a meniscus as described by Ruzicka et al. (2009). Thus, the lag time is largely controlled by the surface wettability and fluid viscosity. Similar to volume data, the formation time, dynamic angle and frequency were observed to vary based on temperature, orifice material and diameter, and oil type as elaborated in the later sections. It is important to note that all figures presenting the effects of parameters on bubble dynamics are representative of the entire dataset collected.

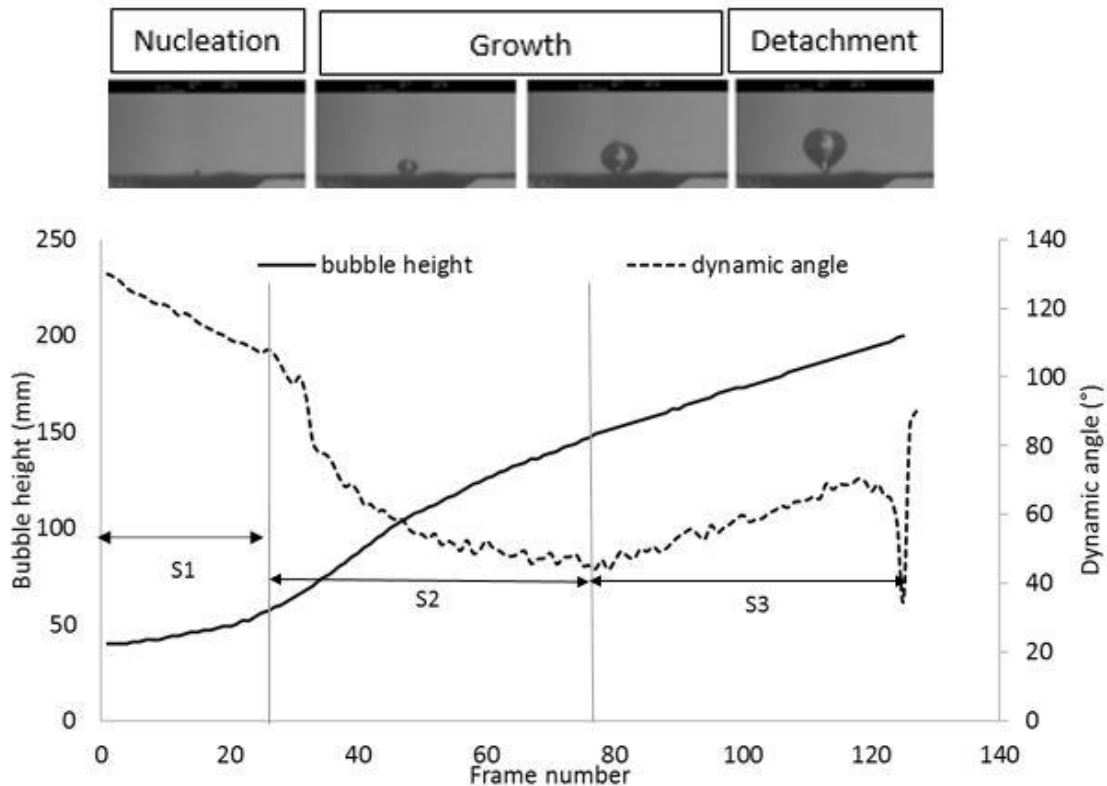


Fig. 4.3. a) Bubble formation stages represented using fresh oil at room temperature on a 0.75 mm steel orifice, b) Change in bubble height with time and dynamic angle corresponding to bubble formation stages: Stage 1 (S1) - nucleation stage, stage 2 (S2) - growth/ elongation stage, stage 3 (S3) - detachment/ pinch-off stage

4.5.1. Effect of temperature

Experiments were conducted for fresh and used oil at room temperature and 170°C for different orifice sizes and two surface materials. Increase in temperature led to decrease in bubble volume (Fig. 4.4a) and bubble formation time (Fig. 4.4b). The bubble frequency increased with increase in temperature (Fig. 4.4c).

Increase in oil temperature causes a linear decrease in oil density and surface tension, and an exponential decrease in viscosity (Sahasrabudhe et al., 2017). The changes in fluid properties were characterized in terms of change in Bo (Eq. 4.1) and Oh (Eq. 4.2) for each orifice diameter studied. For all orifice diameters, Bo increased and Oh decreased with increase in temperature. Hence the smaller formation time and bubble volume observed in the present study agrees with literature findings for aqueous-based studies (Bari and Robinson, 2013; Gerlach et al., 2007; Islam

et al., 2015; Simmons et al., 2015). Lower bubble volume and formation time can be attributed to decrease in fluid density, viscosity, and surface tension with increase in temperature. Increase in temperature also increases the wettability of oil (Aydar et al., 2016), hence oil rewets the surface faster, resulting in a decreased lag time. The decrease in lag time could also be attributed to exponential decrease in viscosity which increases the oil's ability to flow back into the void left as the bubble departs. Improved wettability as temperature increased was also observed in the dynamic angle data, where the rate of change of contact angle was higher during the formation stage, and the rewetting was faster during the lag time between bubbles at 170°C (Fig. 4.4d). Thus, the decrease in volume and increase in frequency with increasing temperature found in the literature (Bari and Robinson, 2013; Gerlach et al., 2007; Islam et al., 2015; Kulkarni and Joshi, 2005; Ramakrishnan et al., 1969; Simmons et al., 2015) agrees with the current findings.

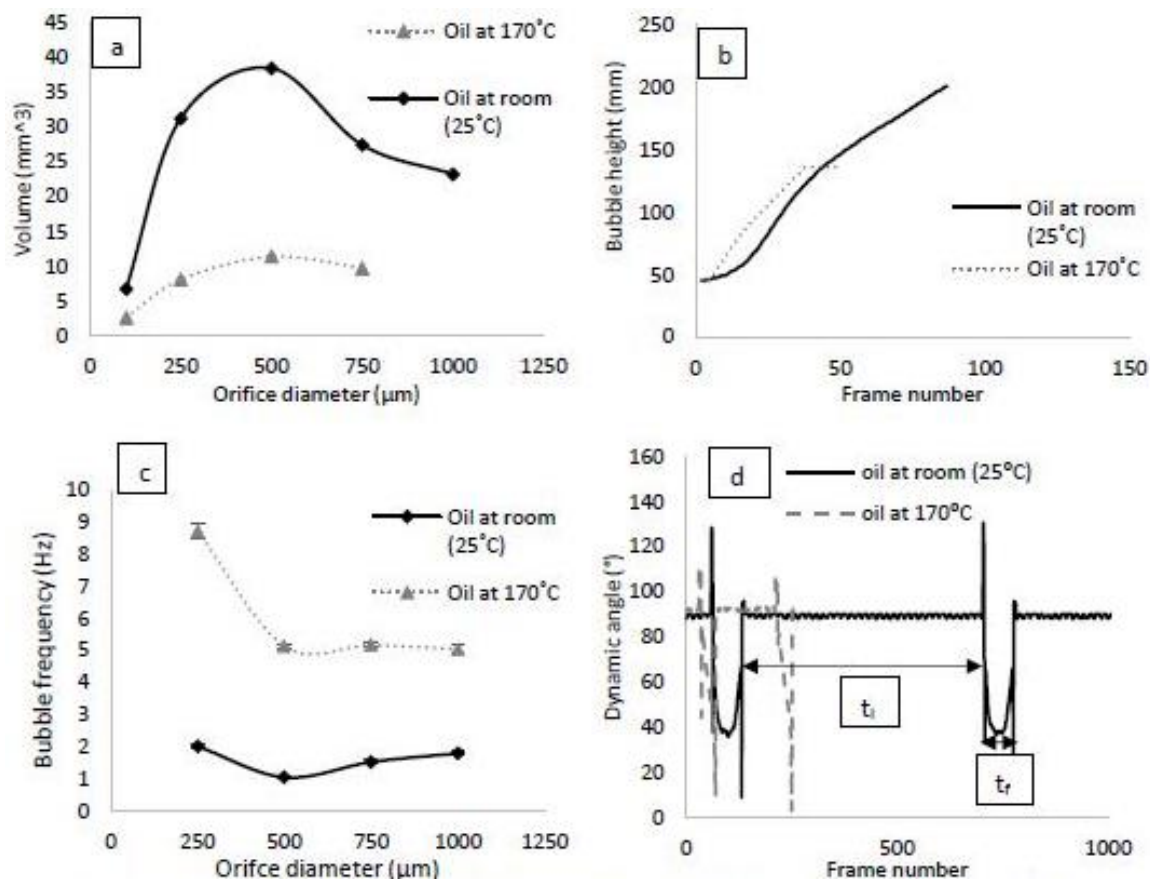


Fig. 4.4. Effect of temperature on a) bubble volume b) bubble formation time, c) bubble frequency and d) formation (t_f) and lag periods (t_l) of subsequent bubbles represented using data for fresh oil on steel surface

4.5.2. Effect of surface wettability

Experiments were conducted for fresh and used oil on steel and Teflon surfaces at room temperature and 170°C with different orifice diameters. The bubbling results for steel and Teflon were analyzed for 0.75 mm and 1 mm orifices. The surface and the capillary were made of the same material for both steel and Teflon. Teflon has a lower wettability (equilibrium angle, $\theta = 60^\circ$) with oil compared to steel ($\theta = 12^\circ$). Bubbles formed on the Teflon surface had a higher volume and a lower frequency than the steel surface. Gerlach et al. (2007) also found an increase in bubble diameter with increase in contact angle for aqueous systems and attributed it to increase in capillary force acting downwards. Higher bubble volumes on less wettable surfaces have also been reported in numerous studies in literature (Chen et al., 2009; Chesters, 1978; Yu et al., 2015; Yuan et al., 2014).

Lower frequency of bubbling on a Teflon surface was accompanied with higher lag time between two bubbles on the Teflon surface (Fig. 4.5b) caused by low wettability. The low wettability prevented oil from rewetting the void created due to bubble pinch-off during the time between consecutive bubbles. However, the bubbles on Teflon experienced a lower formation time compared to steel surface (Fig. 4.5b, 4.5c). The bubble forming on the steel surface experienced a significant lag during the nucleation stage. Capillary force acting on the steel surface was higher due to high wettability of steel. However, on the Teflon surface, the bubble expanded almost immediately and was acted upon by the partial buoyancy force. This was also observed in Fig. 4.5c where the angle on a Teflon surface almost immediately decreased to $\theta < 90^\circ$. Still images captured from bubble formation on the two orifices showed that the bubble did not completely occupy the orifice perimeter when forming on the steel surface, whereas for Teflon, the bubble occupied the entire orifice perimeter/base, and expanded slightly beyond the orifice rim (Fig. 4.5a). It is hypothesized that for non-wetting surface, the liquid sticks to itself and pulls liquid from inside the pore since the liquid does not have affinity to the non-wetting pore walls. Hence, the bubble base is pinned to the orifice rim and the bubble shape is controlled by surface tension forces. For the wetting surface, the liquid adheres to the pore walls, hence during bubble formation, the bubble base is smaller than the orifice rim and the shape of the bubble is controlled by the adhesion forces between liquid and the capillary wall. Thus, smaller bubbles are formed on a steel surface. The oil adhered to the wall also causes a significant drag force on the bubble due to capillarity, leading to an increase in bubble formation time. Thus, the difference in wettability of the surface and the pore walls results in bubbles of different shapes which governs formation and lag time between bubbles emerging from the two surfaces and therein the bubble frequency and volume.

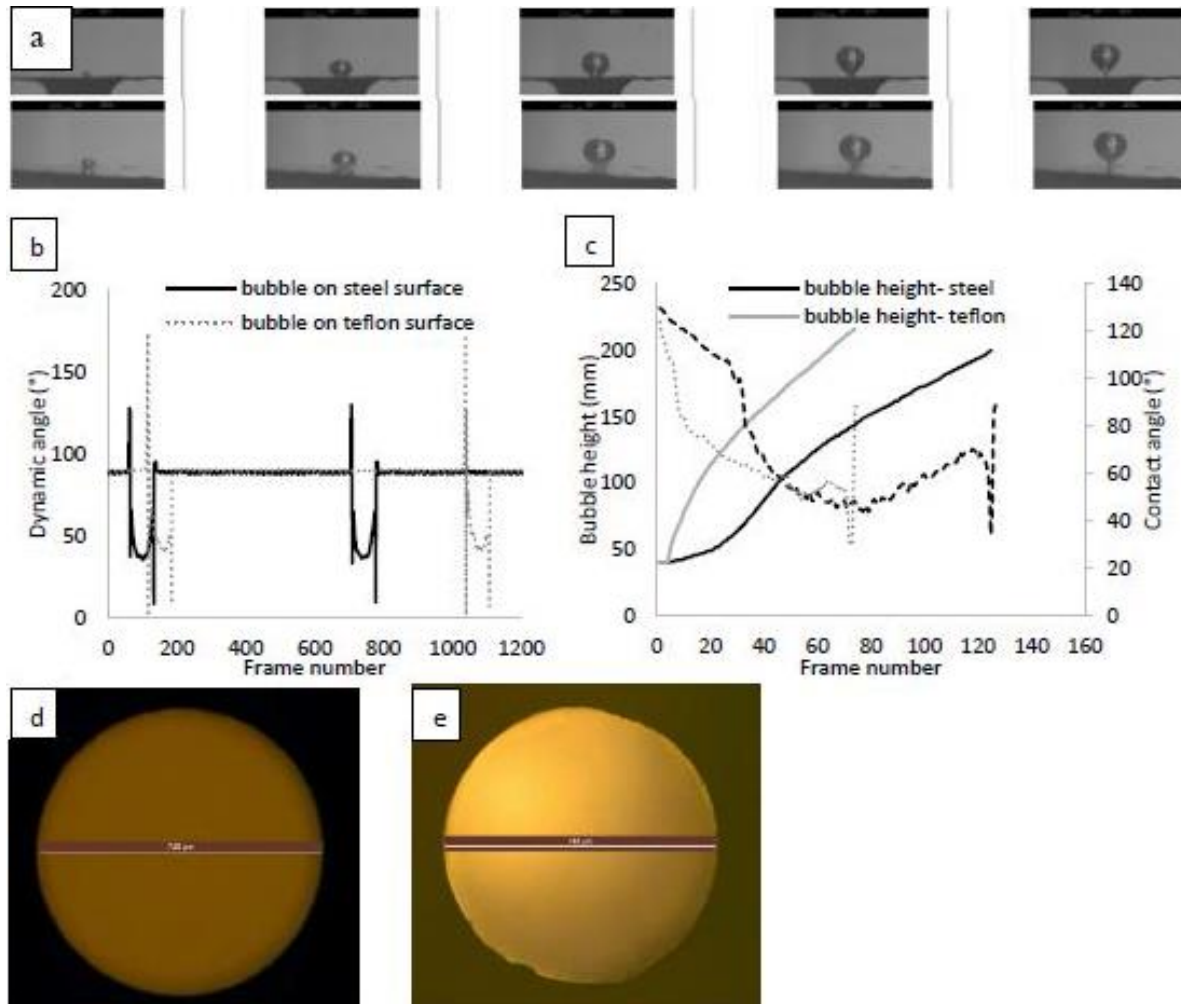


Fig. 4.5. Effect of surface wettability on bubble characteristics as demonstrated by a) video clipping of bubble formation on steel and Teflon surfaces, b) formation time and contact angle of oil on steel and Teflon orifices, c) formation and lag periods of subsequent bubbles, d) microscopy image of 0.75 mm steel orifice, e) microscopy image of 0.75 mm Teflon orifice

4.5.3. Effect of oil quality

The results from the current study showed decrease in bubble volume (Fig. 4.6a) and increase in bubble frequency with used oil (Fig. 4.6c). Degradation of oil during frying results in increased wettability of oil and increased viscosity at room temperature (Sahasrabudhe et al., 2019). The density and surface tension of oil are not affected by degradation during frying (Sahasrabudhe et al., 2019). Hence, the Bond number remains the same with change in oil quality. Degraded oil has higher Oh number at room temperature due to higher viscosity, however at 170°C , Oh is the same for both oils.

The bubble formation time in used oil was higher compared to fresh oil at room temperature (Fig. 4.6b), which can be attributed to increase in Ohnesorge number. The bubbles in used oil experience a higher drag force (Fig 4.6b), resulting in a higher formation time. At 170°C, fresh and used oil have the same viscosity, thus the bubble formation time for used oil was the same/lower than fresh oil. Increased wettability with used oil promoted faster rewetting of the void created by bubble departure in the time between two consecutive bubbles, resulting in less lag time between bubbles formed in used oil (Fig 4.6d) at both temperatures of study. The difference in surface wettability between fresh and used oil is hypothesized to affect the meniscus shape and dynamics when the oil enters the capillary in the period between two bubbles. This can eventually lead to differences in lag time as bubble forms and detaches from the pore submerged in oil of different quality, thus affecting the amount of oil absorbed by food during the immersion frying stage. Chen et al. (2009) studied bubble dynamics from an orifice submerged in water and concluded that contact angle with the surface is the main parameter that governs bubble dynamics from an orifice. Thus, the differences in bubble dynamics between fresh and used oil can be primarily attributed to change in wettability between the two oils.

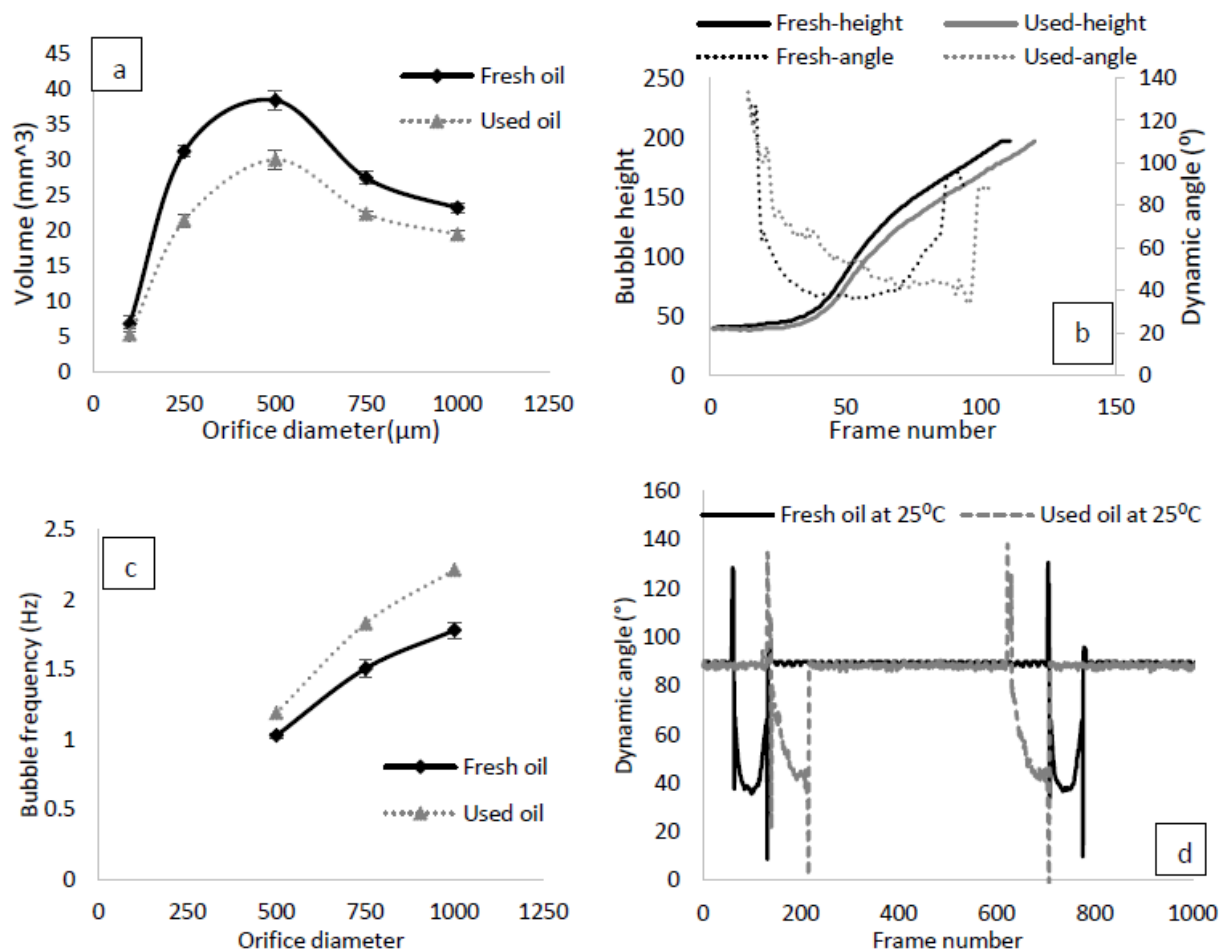


Fig. 4.6. Effect of oil quality on a) bubble volume b) bubble formation time, c) bubble frequency, and d) formation and lag periods of subsequent bubbles

4.5.4. Effect of orifice diameter

Orifice diameters were measured on a microscope (Fig. 4.5d and 4.5e). For Teflon, only orifice sizes of 1 mm and 0.75 mm could be accurately made. In the case of steel, bubbling pattern on orifice diameters from 0.1-1 mm was studied. It was observed that for the steel surface, a single bubble was formed when the diameter was more than 0.25 mm (Fig. 4.7a). This is defined as the single bubble regime as described by Badam et al. (2007). At 0.25 mm, pairing without coalescence occurred in fresh oil and pairing with coalescence occurred in used oil (Fig. 4.7a) at both temperatures of study. When the bubble formation was studied at 0.1 mm orifice diameter, the pattern changed to chain bubbling and a continuous series of bubbles was obtained (Fig. 4.7a). The change in bubble pattern from single to double to a bubbling series has been attributed by previous studies to gas chamber volume (Kovalchuk and Dukhin, 2001). There is a pressure drop

as a bubble pinches off from the orifice. When the gas chamber volume is large, the pressure deficit in the chamber is negligible. Hence, next bubble is formed immediately, which leads to the formation of a bubble series (Kovalchuk and Dukhin, 2001).

In the single bubble formation regime, the bubble volume increased as the orifice diameter decreased from 1 mm to 0.5 mm (Fig 4.4a, 4.6a) and the bubble frequency decreased (Fig. 4.4c, 4.6c). Increase in bubble volume with decrease in orifice diameter was also observed by Zahedi et al. (2014) using the volume of fluid method simulations for orifices submerged in fluids of different density, viscosity and surface tension when the gas mass flow rate was constant. In the current study, effect of orifice size on bubble volume and frequency was observed for both oils, and at both temperatures of study. Higher volume and lower frequency were also observed on the Teflon surface at orifice diameter of 0.75 mm compared to 1 mm (data not shown). Decrease in bubble frequency was due to increase in lag time as the orifice diameter decreased (Fig. 4.7b). Bubble frequency when diameter was less than 0.5 mm could not be quantified accurately due to pairing and coalescence of bubbles. Bubble formation time on the contrary decreased as the diameter decreased from 1 mm to 0.5 mm (Fig. 4.7c). This was corroborated from the dynamic angle data where the rate of change of angle was higher when the pore size was smaller (Fig. 4.7c). For the smaller orifice sizes, the dynamic angle almost instantaneously decreased to $\theta < 90^\circ$. Hence, the force of partial buoyancy acts on the bubble during the early growth stage of the bubble as can be seen by the slope of the graphs in Fig. 4.7c. This phenomenon leads to lower bubble formation time as the orifice size decreases.

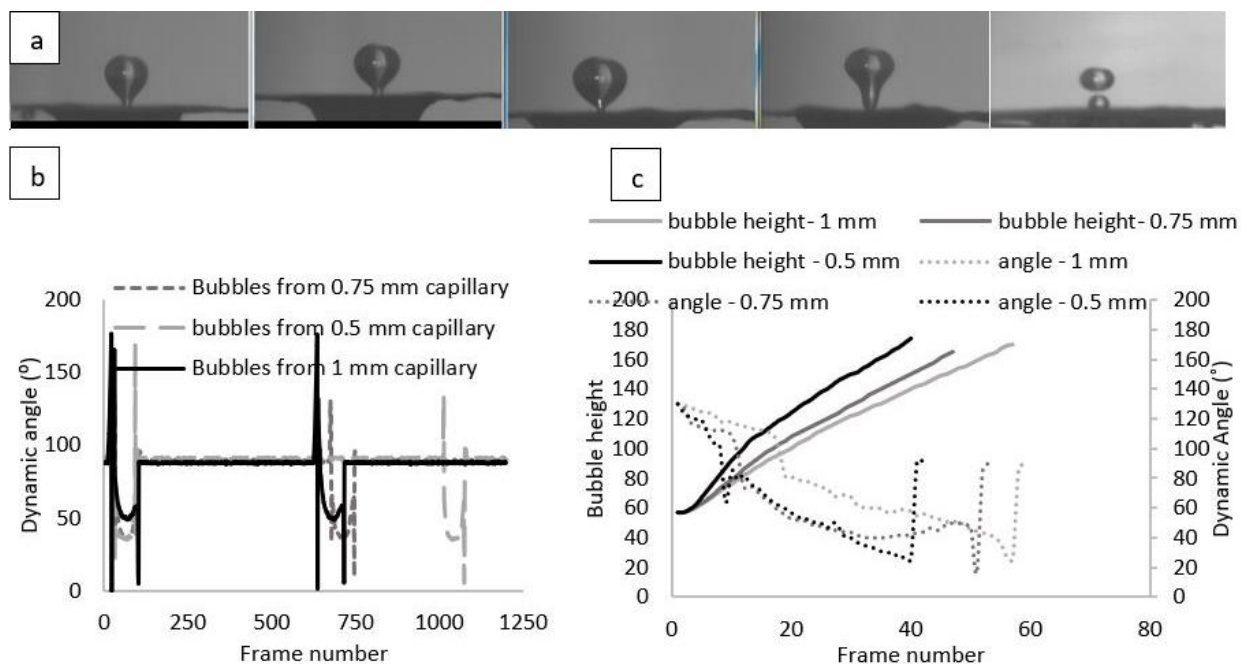


Fig. 4.7. Effect of orifice size represented using fresh oil on a steel surface a) video snips at the time of bubble pinch-off, b) formation and lag periods of subsequent bubbles, c) bubble formation time using bubble height and change in dynamic angle

4.5.5. Effect of bubble dynamics on heat transfer

Frying heat transfer can be described by drawing parallels with pool boiling (Costa et al., 1999; Farkas and Hubbard, 2000; Hubbard and Farkas, 1999). Similar to pool boiling, heat transfer in frying is largely dependent on the bubble diameter at departure (Eq. 4.4), number of nucleation sites and bubble frequency (Mikic and Rohsenow, 1969). The current study focusses on the changes in oil and surface properties that primarily affect the bubble diameter to draw inferences on convective heat transfer coefficient.

Results for the study show that bubble volume decreased, and frequency increased with increasing oil temperature. Higher oil temperature increases the thermal gradient between the bulk oil and evaporation front within the food (Bouchon, 2009; Farkas et al., 1996). This increases the rate of evaporation and thus bubbling at the oil-solid interface (Costa et al., 1999; Farinu and Baik, 2007; Farkas and Hubbard, 2000). Increased oil temperature can lead to smaller bubble diameters due to a decrease in fluid surface tension, viscosity and density (Sahasrabudhe et al., 2017). Studies have found higher heat transfer coefficients for aqueous fluids with lower surface tensions. This has been attributed to the presence of smaller bubbles at a faster rate in these solutions compared

to water (Waseca and Manglik, 2000). Thus, the formation of smaller bubbles at a faster rate at higher temperature observed in the current study supports literature findings on enhanced heat transfer coefficient at higher temperature.

Farkas and Hubbard (2000) observed enhancement of heat transfer coefficient as oil was degraded during frying. Change in oil viscosity and surface tension have been attributed as the primary contributors to enhanced heat transfer. Recent studies have shown that oil-steam surface tension and oil viscosity are not affected by oil quality at frying temperatures (Sahasrabudhe et al., 2019). However, the oil wettability increases with degradation (Sahasrabudhe et al. 2019). In the present study, bubble frequency per pore in used oil was 10-15 % higher than fresh oil at 170°C (Fig. 4.8a) and 15-25 % higher at room temperature (Fig. 4.6c). Lower bubble volume was obtained with used oil compared to fresh oil. Frying is a temperature-controlled process. Hence, formation of smaller bubbles will result in higher heat flux causing higher agitation which in turn increases the heat flux further (Farkas and Hubbard, 2000). Thus, enhanced heat transfer observed when degraded oil is used for frying can be attributed to the increased convective heat transfer caused by a large number of small bubbles formed at a higher rate in used oil. Change in wettability with oil quality is the primary contributor to the enhanced heat transfer as elaborated in section 4.3. This finding was also corroborated from bubble formation data on steel and Teflon surfaces (section 4.2), where the bubble volumes were smaller, and the frequency was higher on a steel surface. Thus, changing the wettability at the fluid/solid interface either by changing the liquid properties or by coating the surface with a wettable/non-wettable substrate can impact the overall heat transfer during immersion frying. Bubble volume increased, and frequency decreased as the orifice diameter decreased from 1 - 0.5 mm. For orifice sizes of 0.25 mm and 0.1 mm, non-linear bubble dynamics were observed. Thus, change in surface pore size distribution in food during frying can also impact the rate of heat transfer and needs to be studied further.

The current study gives a basic understanding of the factors governing bubble formation (Table 4.1), and thus heat transfer during immersion frying stage. During frying, bubbles emerge from multiple orifices and there can be lateral coalescence during the formation stage. The surface pore size distribution in food can lead to formation of bubbles of different sizes which travel at different speeds in the oil and thus increase turbulence in oil further. However, the understanding of bubble formation at multiple orifices is beyond the scope of this study and can be a topic for future consideration.

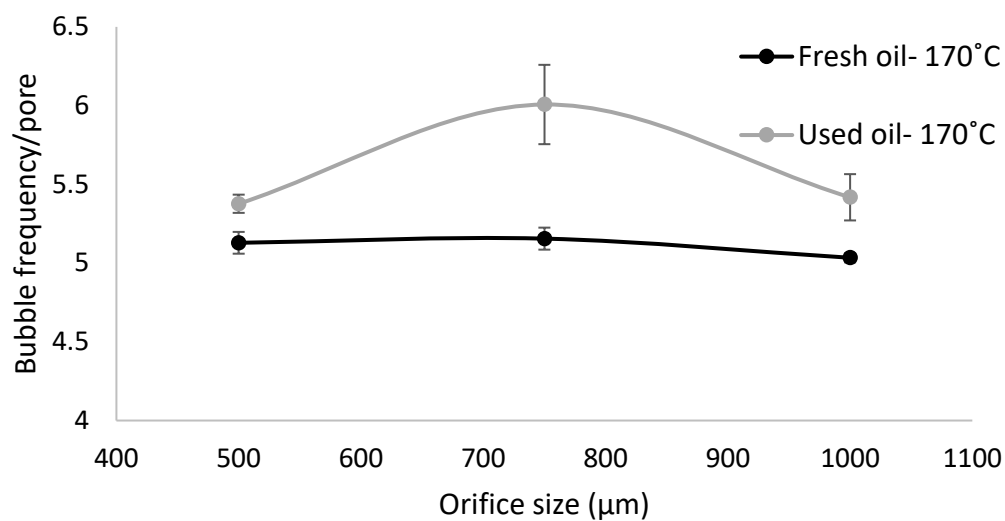


Fig. 4.8. Effect of oil quality on bubble frequency per pore. Represented at 170°C on steel surface for 0.5 mm-1 mm orifice diameter

Table 4.1. Summary of the effects of liquid and surface properties on the formation time, lag time, bubble frequency, bubble volumes and heat transfer for vegetable oil data

Property	Change in property	Formation time	Lag time	Frequency	Bubble Volume	Heat transfer rate
Temperature	↑	↓	↓	↑	↓	↑
Surface wettability	↑	↑	↓	↑	↓	↑
Oil degradation (TPM content)	↑	Higher at room temperature Same/ lower at 170°C	↓	↑	↓	↑
Orifice diameter	↓	↓	↑	1 to 0.5 mm: single bubbling 0.25 mm: pairing w/wo coalescence 0.1 mm: chain bubbling	Increased from 1 to 0.5 mm 0.25mm- large coalesced bubbles 0.1mm - small volume bubbles	↑

4.6. Conclusion

Degradation of oil during frying may result in enhanced heat transfer rate due to formation of a higher number of small bubbles. Heat transfer during frying is controlled by temperature of oil and oil degradation, as well as food properties such as surface wettability and pore size distribution. The results from this study can be used to understand the changes in heat transfer coefficients in frying as the oil and food properties are changed.

4.7. Funding sources

This work was supported by AFRI Grant no. 2014-67017-21831 from the USDA National Institute of Food and Agriculture, Improving Food Quality – A136.

4.8. Acknowledgements

The authors would like to thank Dr. Dhananjay Pai, Dr. Shankarli Pradhan, and Dr. Carl Wassgren for letting us access to use equipment's in their lab. The authors would also like to thank the Purdue research computing group, Dr. Carlos Corvalan and Dr. Jiakai Lu for their assistance in data analysis on Purdue computer cluster.

4.9. References

- Aydar, A., Rodriguez-Martinez, V., Farkas, B. (2016). Determination and modeling of contact angle of Canola oil and olive oil on a PTFE surface at elevated temperatures using air or steam as surrounding media. *LWT- Food Science and Technology*, 65, 304–310.
- Badam, V.K., Buwa, V., Durst, F. (2007). Experimental investigations of regimes of bubble formation on submerged orifices under constant flow condition. *Canadian Journal of Chemical Engineering*, 85, 257–267.
- Bari, S.D., Robinson, A.J. (2013). Experimental study of gas injected bubble growth from submerged orifices. *Experimental Thermal and Fluid Science*, 44, 124–137.
- Blumenthal, M.M., Stier, R.F. (1991). Optimization of deep-fat frying operations. *Trends Food Science Technology*, 2, 144–148.
- Bouchon, P. (2009). Understanding oil absorption during deep-fat frying. *Advances in Food Nutrition Research*, 57, 209–234.
- Chen, Y., Mertz, R., Kulenovic, R. (2009). Numerical simulation of bubble formation on orifice plates with a moving contact line. *International Journal of Multiphase Flow*, 35, 66–77.
- Chesters, A.K. (1978). Modes of bubble growth in the slow-formation regime of nucleate pool boiling. *International Journal of Multiphase Flow*, 4, 279–302.

- Costa, R.M., Oliveira, F.A., Delaney, O., Gekas, V. (1999). Analysis of the heat transfer coefficient during potato frying. *Journal of Food Engineering*, 39, 293–299.
- Dana, D., Saguy, I.S. (2006). Mechanism of oil uptake during deep-fat frying and the surfactant effect- theory and myth. *Advances Colloid Interface Science*, 128–130, 267–272.
- Dhir, V.K. (1998). Boiling Heat Transfer. *Annual Review of Fluid Mechanics*, 30, 365–401.
- Dhir, V.K., Abarajith, H.S., Li, D. (2007). Bubble dynamics and heat transfer during pool and flow boiling. *Heat Transfer Engineering*, 28, 608–624.
- Farinu, A., Baik, O. D. (2007). Heat transfer coefficients during deep fat frying of sweet potato: Effects of product size and oil temperature. *Food Research International*, 40, 989–994.
- Farkas, B. E., Hubbard, L.J. (2000). Analysis of convective heat transfer during immersion frying. *Drying Technology*, 18, 1269–1285.
- Farkas, B.E., Singh, R.P., Rumsey, T.R. (1996). Modeling heat and mass transfer in immersion frying. I, model development. *Journal of Food Engineering*, 29, 211–226.
- Gerlach, D., Alleborn, N., Buwa, V., Durst, F. (2007). Numerical simulation of periodic bubble formation at a submerged orifice with constant gas flow rate. *Chemical Engineering Science*, 62, 2109–2125.
- Hubbard, L.J., Farkas, B.E. (1999). A method for determining the convective heat transfer coefficient during immersion frying. *Journal of Food Process Engineering*, 22, 201–214.
- Islam, M.T., Ganesan, P.B., Sahu, J.N., Sandaran, S.C. (2015). Effect of orifice size and bond number on bubble formation characteristics: A CFD study. *Canadian Journal of Chemical Engineering*, 93, 1869–1879.
- Kalogianni, E.P., Karastogiannidou, C., Karapantsios, T.D. (2009). Effect of the presence and absence of potatoes under repeated frying conditions on the composition of palm oil. *Journal of American Oil Chemists' Society*, 86, 561–571.
- Kandlikar, S.G. (2003). Heat transfer mechanisms during flow boiling in microchannels 33–46.
- Kim, J. (2009). Review of nucleate pool boiling bubble heat transfer mechanisms. *International Journal of Multiphase Flow*, 35, 1067–1076.
- Kovalchuk, V.I., Dukhin, S.S. (2001). Dynamic effects in maximum bubble pressure experiments. *Colloids Surf. Physicochemical Engineering Aspects*, 192, 131–155.
- Kulkarni, A.A., Joshi, J.B. (2005). Bubble formation and bubble rise velocity in gas–liquid systems: A review. *Ind. Engineering Chemical Research*, 44, 5873–5931.
- Mikic, B.B., Rohsenow, W.M. (1969). A new correlation of pool-boiling data including the effect of heating surface characteristics. *Journal of Heat Transfer*, 91, 245–250.
- Mir-Bel, J., Oria, R., Salvador, M.L. (2012). Influence of temperature on heat transfer coefficient during moderate vacuum deep-fat frying. *Journal of Food Engineering*, 113, 167–176.
- Mohanty, R.L., Das, M.K. (2017). A critical review on bubble dynamics parameters influencing boiling heat transfer. 78, 466–494.
- Phan, H.T., Caney, N., Marty, P., Colasson, S., Gavillet, J. (2009). Surface wettability control by nanocoating: The effects on pool boiling heat transfer and nucleation mechanism. *International Journal on Heat Mass Transfer*, 52, 5459–5471.

- Pioro, I.L., Rohsenow, W., Doerffer, S.S. (2004). Nucleate pool-boiling heat transfer. I: review of parametric effects of boiling surface. *International Journal on Heat Mass Transfer*, 47, 5033–5044.
- Ramakrishnan, S., Kumar, R., Kuloor, N.R. (1969). Studies in bubble formation—I bubble formation under constant flow conditions. *Chemical Engineering Science* 24, 731–747.
- Ruzicka, M.C., Bunganic, R., Drahoš, J. (2009). Meniscus dynamics in bubble formation. Part I: Experiment. *Chemical Engineering Research Design*, 87, 1349–1356.
- Safari, A., Salamat, R., Baik, O. D. (2018). A review on heat and mass transfer coefficients during deep-fat frying: Determination methods and influencing factors. *Journal of Food Engineering*, 230, 114–123.
- Sahasrabudhe, S.N., Rodriguez-Martinez, V., O’Meara, M., Farkas, B.E. (2017). Density, viscosity, and surface tension of five vegetable oils at elevated temperatures: Measurement and modeling. *International Journal of Food Properties*, 0, 1–17.
- Sahasrabudhe, S. N., Chaudhari, S. S., and Farkas, B. E. (2019). Experimental measurement of factors affecting dynamics of bubble growth from a submerged orifice: Applications to the frying process. *Journal of Food Engineering*, 251, 36-44.
- Shekrladze, I.G. (2008). Boiling heat transfer: Mechanisms, models, correlations and the lines of further research. *Open Mechanical Engineering Journal*, 2, 104–127.
- Simmons, J.A., Sprittles, J.E., Shikhmurzaev, Y.D. (2015). The formation of a bubble from a submerged orifice. *European Journal of Mechanics*, 53, 24–36.
- Teodori, E., Palma, T., Valente, T., Moita, A.S., Moreira, A.L.N. (2016). Bubble dynamics and heat transfer for pool boiling on hydrophilic, superhydrophobic and biphilic surfaces. *Journal of Physics: Conference Series*, 745, 032132.
- Tong, L.S., Tang, Y.S. (1997). *Boiling heat transfer and two-phase flow*. CRC Press.
- van Koerten, K.N., Somsen, D., Boom, R.M., Schutyser, M.A.I. (2017). Modelling water evaporation during frying with an evaporation dependent heat transfer coefficient. *Journal of Food Engineering*, 197, 60– 67.
- Wasekar, V.M., Manglik, R.M. (2000). Pool boiling heat transfer in aqueous solutions of an anionic surfactant. *Journal of Heat Transfer*, 122, 708.
- Yu, X., Wang, Y., Huang, C., Du, T. (2015). Three stages of bubble formation on submerged orifice under constant gas flow rate. *Journal of Physics: Conference Series*, 656(1): 012042.
- Yuan, J., Li, Y., Zhou, Y. (2014). Effect of contact angle on bubble formation at submerged orifices. *Journal of Material Science*, 49, 8084–8094.
- Zahedi, P., Saleh, R., Moreno-Atanasio, R., Yousefi, K. (2014). Influence of fluid properties on bubble formation, detachment, rising and collapse; Investigation using volume of fluid method. *Korean Journal of Chemical Engineering*, 31, 1349–1361.
- Zhang, L., Shoji, M. (2001). Aperiodic bubble formation from a submerged orifice. *Chemical Engineering Science*, 56, 5371–5381.

5. PARAMETRIC STUDY ON LIQUID AND SURFACE PROPERTIES AFFECTING MENISCUS DYNAMICS DURING BUBBLE FORMATION

*Shreya N. Sahasrabudhe*¹, *Jennifer A. Staton*², *Brian E. Farkas*^{1*}

¹ Department of Food Science, College of Agriculture, Purdue University. West Lafayette, IN 47907 USA.

² Department of Chemical Engineering, University of California, Davis, One Shields Avenue, Davis, CA 95616, USA

Corresponding Author

*Contact author: 745 Agriculture Mall Drive. West Lafayette, IN 47907; Tel.: +1 765 494 8256; fax: +1 765 494 7953; e-mail: bfarkas@purdue.edu

5.1. Introduction

The dynamics of bubble formation in a liquid play an important role in a wide array of phenomena observed in the petrochemical, mineral, food and pharmaceutical industries. For processes such as distillation, boiling, frying, whipping, or fluidization, understanding bubble dynamics can be useful for the accurate prediction of heat and mass transfer (Kulkarni and Joshi, 2005; Zahedi et al., 2014), and understanding of bubble-bubble and bubble-liquid interactions (Mosdorf and Wyszowski, 2010). Liquid properties and liquid-solid interactions influence the hydrodynamic properties of the process and are required for the accurate estimation of transfer coefficients (Kulkarni and Joshi, 2005; Ramakrishnan et al., 1969).

Experiments have been conducted and mathematical models developed to understand the effect of fluid properties, fluid-solid interaction, and process parameters on bubble dynamics from an orifice submerged in a liquid (Bari and Robinson, 2013; Gerlach et al., 2007; Kulkarni and Joshi, 2005; Ramakrishnan et al., 1969; Yu et al., 2015; Yuan and Lee, 2013). Bubble formation is divided into three stages: nucleation, growth and detachment. The bubble shape changes from a spherical segment during nucleation stage to a hemispherical shape during growth stage to formation of a neck at the surface before pinch-off (Bari and Robinson, 2013; Sahasrabudhe, Chaudhari and Farkas, 2019). The formation of bubbles can be described using a force balance

between surface tension, buoyancy, pressure force (gas flow rate), inertial force and viscous drag (Bari and Robinson, 2013; Gerlach et al., 2007; Kalaikadal, 2012; Ramakrishnan et al., 1969; Yu et al., 2015; Zhang and Shoji, 2001). Surface tension, inertial forces and viscous drag are known to stabilize the bubble. Buoyancy and pressure force cause destabilization and eventual detachment of the bubble (Fig. 5.1) (Bari and Robinson, 2013; Ramakrishnan et al., 1969). Thus, understanding the balance between these forces aids in understanding bubble dynamics. To assess this, dimensionless numbers such as Reynolds number Re , Bond Number Bo , Weber number We , and Capillary number Ca have been used (Gerlach et al., 2007; Simmons et al., 2015; Stanovsky et al., 2011).

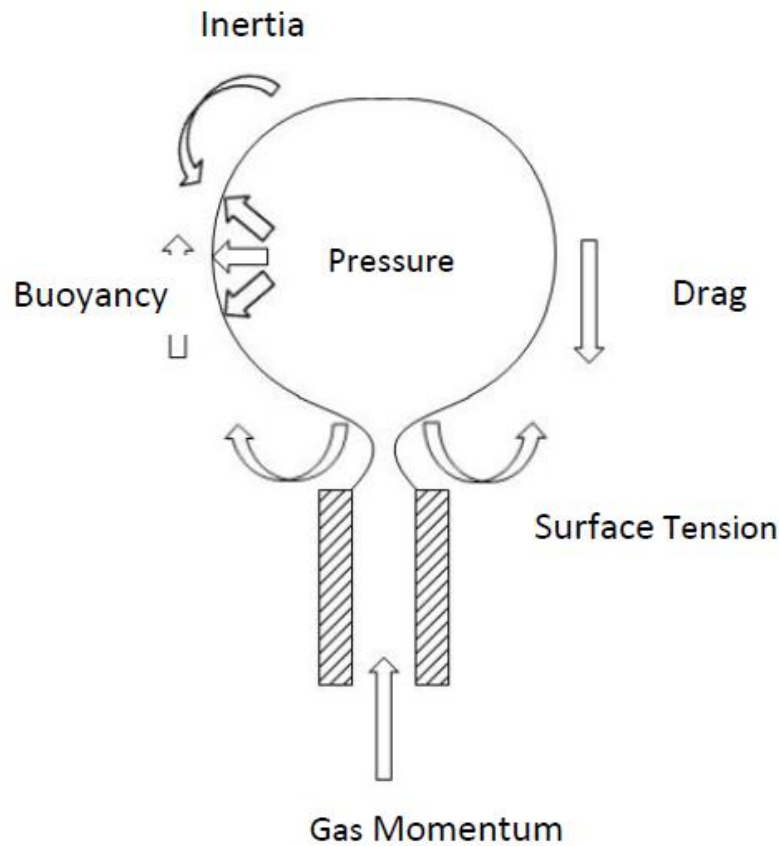


Fig. 5.1. Force balance for a bubble formation from a submerged liquid (Kalaikadal, 2012)

Reynolds number (Re) is used to differentiate between inertial and viscous driven flows, with high Re values indicating inertial driven flow. Bond number (Bo) predicts if flow is gravity or capillarity controlled. The flow behavior can be categorized as capillarity controlled when Bo

$\ll 1$, capillarity/gravity controlled when the $Bo \sim 1$ resulting in meniscus oscillations, and gravity controlled when $Bo > 1$ resulting in weeping (Stanovsky et al., 2011). Weeping is the gravity controlled entrance of liquid into a capillary during the time between subsequent bubbles (McCann and Prince, 1969). Capillary length (λ) is the characteristic length scale for an interface between two fluids at which $Bo = 1$. Weber number (We) is used to distinguish between inertial and capillarity driven flow. Values of We are highly dependent on the flow rate of the gas during bubbling, with high flow rates leading to high We values. At lower We (<1), the gas-liquid interface reforms in the time interval between subsequent bubbles. The meniscus formed may enter the capillary in this time interval. At high We (>1), the meniscus is destroyed by the gas flow (Stanovsky et al., 2011). Hence, the meniscus does not close between consecutive bubbles and the bubbles exist as a stream described as jetting. Capillary number (Ca) is the ratio of viscous to surface tension forces acting across an interface between a liquid and gas. High Ca numbers indicate that the surface tension forces have a negligible effect on bubble dynamics. The values of these dimensionless numbers control the dynamics of bubble growth as they influence the volume and frequency of bubble formation.

Studies have also been conducted on the ingress of fluid between bubbles (Ruzicka, et al., 2009a), and mathematical models have been developed to predict the dynamics of meniscus growth and its effect on periodicity of bubble formation. Stanovsky et al. (2011) conducted a parametric study to understand the effect of orifice diameter, fluid flow rate, gas chamber size, liquid height and liquid viscosity on meniscus dynamics during bubble formation, and hence on bubble periodicity. The study found that a change in the orifice diameter shifted the bubbling regime from capillarity driven to gravity driven behavior and was characterized using Bo . In the capillarity driven regime, the meniscus entered the capillary and the motion was described using a piston. At high flow rates, the bubble formation was inertially driven and was described using We . An increase in the chamber volume and liquid height was found to increase total bubble formation time as well as bubbling time. The main effect of liquid viscosity observed was dampening of the meniscus oscillations in the capillary during the waiting time. Stanovsky et al. (2011) however did not consider the effect of liquid surface tension or the contact angle at the solid-liquid interface on meniscus motion and bubble periodicity.

Maximum bubble pressure method (MBPM) is a technique to measure dynamic surface tension of a liquid. The principle of this technique is based on a submerged bubble assembly, where

the capillary orientation can be upwards or downwards facing. The equipment calculates liquid surface tension based on differential pressure changes as bubbles emerge from the tips of two separate capillaries immersed at an equal depth in the fluid. The differential pressure between the two capillaries is measured, and the bubbling pattern is described in terms of the bubble lifetime (t_l) and the dead-time (t_d) (Kovalchuk and Dukhin 2001; Dukhin et al., 1996). Bubble lifetime is the sum of the times t_{11} , t_{12} and t_{13} . Forward meniscus motion (t_{11}) is the time from bubble pinch-off (collapse of gas bridge) to maximum meniscus penetration depth (h) inside the capillary. Reverse meniscus motion (t_{12}) is the time during which the meniscus moves back to the end of the capillary. During the next stage of growing bubble evolution (t_{13}), the bubble radius decreases and becomes equal to the capillary radius (Dukhin et al., 1998a, Dukhin et al., 1998b). For both capillaries, pressure rises as the bubble grows from the initial formation of the meniscus to the formation of a hemispherical cap with diameter equal to the orifice diameter (Fig. 5.2). This time period is the bubble lifetime (t_l) and the pressure when the hemispherical bubble cap exists is the maximum pressure (Dukhin et al., 1996). As the bubble continues to grow, the pressure begins to decrease until detachment occurs. This is the dead time (t_d) and the decrease in pressure during this period is due to an increase in the radius of curvature of the bubble. These changes in pressure during the bubble growth and detachment can lead to ingress of fluid in the capillary in the time between two bubbles (Fig. 5.2).

The motion of the meniscus between consecutive bubbles was described by (Dukhin et al., 1996; Dukhin et al., 1998a; Kovalchuk and Dukhin, 2001) using slow oscillations and fast oscillations. The type of oscillation is dependent on the time for pressure restoration in the capillary also called the hydrodynamic relaxation time (t_h). Hydrodynamic relaxation time (t_h) is sum of the times t_{11} and t_{12} known as the forward and reverse meniscus motion respectively (Fig 5.2) (Dukhin et al., 1998a, Fainerman and Miller, 1998, Kovalchuk and Dukhin 2001).

For short wide capillaries, pressure restoration time (t_h) is much shorter than t_{13} . Thus, the condition for the presence of fast oscillations is $t_{11}+t_{12} \lll t_{13}$. Hence, the pressure along the capillary is restored before the maximum pressure in the bubble is overcome. After bubble pinch-off, the pressure in the capillary at the orifice (P_b) is lower than the excess pressure in the gas reservoir (P_s). However, the gas velocity in the capillary reaches its maximum value. Hence gas from the reservoir flows into the capillary driven by excess pressure difference and inertia causing a smoothing of the pressure profile along the capillary. The capillary is shut off by meniscus

formation immediately after bubble pinch-off (Dukhin et al., 1998b). Thus, gas flow immediately encounters the meniscus and compresses the adjacent gas layers. The meniscus then oscillates at the capillary end due to the inertia and elasticity of gas.

For long narrow capillaries, gas flow within the capillary follows Poiseuille flow since significant viscous dissipation occurs which suppresses inertial effects. The pressure restoration time (t_h) is higher than t_{13} (Dukhin et al., 1998a). Thus, the pressure near the meniscus is not restored immediately after bubble-pinch off. There is a low pressure near the capillary surface at the moment of bubble pinch-off. Thus, the capillary pressure of the newly forms meniscus exceeds the pressure in the adjacent gas layer. This leads to displacement of meniscus inside the capillary. When the gas pressure becomes equal to the meniscus capillary pressure, meniscus moves back to the capillary tip (Dukhin et al., 1998a; Kovalchuk and Dukhin, 2001). Hence, for long narrow capillaries where the liquid wets the surface, the liquid always enters the capillary. Once the pressure is restored in the capillary, a new bubble is formed. The depth of meniscus entry is dependent on the liquid properties as well as liquid-solid interaction parameters.

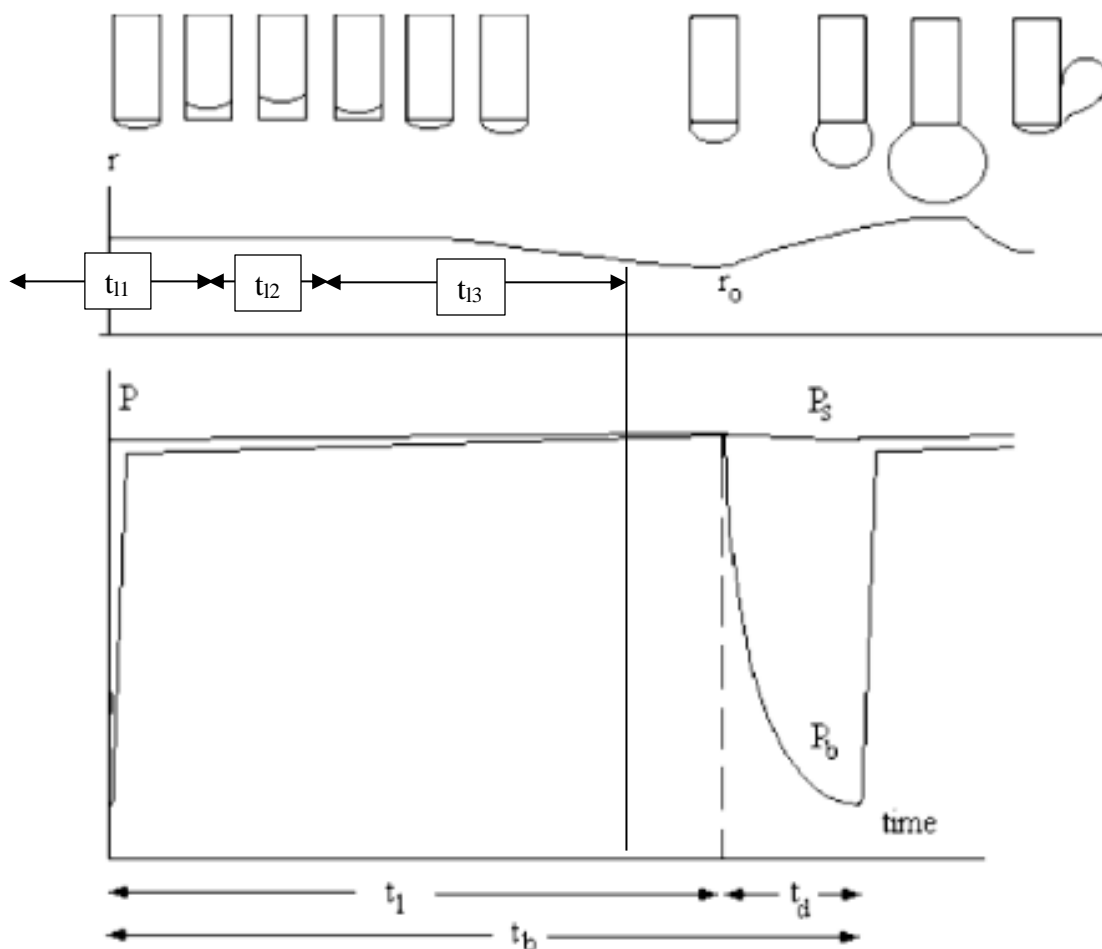


Fig. 5.2. Bubble formation, variation of bubble radius r and pressure within bubble P_b and measuring system P_s during the bubble lifetime (t_1) and deadtime (t_d) for a downward facing capillary. Stages t_{11} , t_{12} , and t_{13} represent stages of meniscus motion during bubble formation time. (Kovalchuk and Dukhin 2001)

Studies by Gerlach et al. (2007); Kulkarni and Joshi (2005); Ramakrishnan et al. (1969); Simmons et al. (2015); Wang et al. (2016) have focused on understanding the effect of system properties, liquid parameters, and capillary diameters on bubble formation and growth from a submerged orifice. Meniscus dynamics during bubble formation has been shown to be responsible for bubble formation pattern and is known to dictate the overall bubbling frequency (Ruzicka, et al., 2009a, 2009b). The dynamics of flow during the bubble formation process are highly driven by surface tension. In addition, the liquid-solid contact angle has been attributed by studies to be the most important factor affecting bubble dynamics (Gerlach et. al, 2005). However, to our knowledge, no studies have been conducted examining the effect of liquid properties (primarily

surface tension) or liquid-solid interactions on meniscus dynamics during bubble formation. Furthermore, the studies in the past have been conducted in either capillarity driven, or gravity driven regimes and the parametric effect of both regimes is not widely understood. A parametric study on meniscus behaviors can help predict the flow behavior and bubble frequency for a wide range of fluids and fluid-solid surfaces when the physical properties of the fluid and solid surfaces are known.

5.2. Materials and Methods

Experiments were performed using deionized water, sodium n-dodecyl sulfate (SDS) solutions, and glycerol to understand effect of liquid properties on bubble formation from a capillary. SDS (Sodium n-dodecyl sulfate, 99 %, Molecular Biology Grade, Catalogue no. G31-1) and glycerol (Clear, Colorless/USP/FCC, Catalogue no. AAJ6760622) were obtained from Fisher-Scientific, Pittsburgh, PA USA. SDS solutions were prepared at two different concentrations (2.67 mM and 8 mM) in water to understand the effect of surface tension on the bubble dynamics. Glycerol solutions were prepared at two different concentrations (26.7 % and 80 %) to evaluate the effect of viscosity on bubble dynamics.

5.2.1. Protocol for silanization of glass

To evaluate the effect of wetting on bubble formation dynamics, glass capillaries and coverslips were silanized using octadecyltrichlorosilane (OTS) from Gelest Inc (Morrisville, PA). Prior to silanization, the glass substrates were carefully sonicated in a Hellmanex solution (Hellma Analytics; Mülheim, Germany) using a sonicator bath. The substrates were rinsed thoroughly with MilliQ deionized water (Millipore; Burlington, MA) and then dried with clean nitrogen. Following drying, the capillaries were sonicated in acetone, then isopropanol, and then rinsed with MilliQ deionized water and dried again with clean nitrogen. Finally, the capillaries were UV-Ozone treated for 1 hour. Immediately following the UV-Ozone treatment, the glass capillaries or coverslips were allowed to come to room temperature and then placed in a jar with 50mL of toluene. 15uL of OTS was then slowly dispensed over the glass substrates while a stir bar gently stirred the solution. The reaction was left to proceed for 1 hour, after which, the glass substrates were removed and placed in a clean jar of toluene for 15 minutes under stirring to remove excess silanes. The

substrates were then dried with clean nitrogen and placed in an oven at 130°C for 2 hours for curing.

5.2.2. Surface tension measurement- rising bubble

Dynamic surface tension measurements for all the liquids used in the study were obtained with a Teclis drop-profile tensiometer (Model Tracker S; Longessaigne, France). For each experiment, the sample was dispensed into a quartz cuvette and placed in the path of a collimated light beam that was positioned opposite a CCD camera. A rising air bubble was quickly formed in the fluid using a stainless-steel J-shaped needle; the volume of the bubble (4 μL) was maintained with the aid of the WDROP software provided by Teclis. Silhouette images of the rising air bubble were captured with the CCD camera and shape of the interface was used to determine the surface tension over time by comparison with Young-Laplace equation as described in Sahasrabudhe, Staton and Farkas (2019). All measurements were performed in triplicate with an accuracy of 0.1 mN/m and the average of the three trials is reported.

5.2.3. Contact angle measurements

Static contact angles of all the liquids used in the study were measured on a hydrophilic and a hydrophobic surface at room temperature using a ramé-hart goniometer, equipped with an automated dispensing system (P/N 100-22, ramé-hart Instrument Co., Succasunna, USA). Glass cover slips were used as a hydrophilic substrate for the measurement. Silanized glass cover slips were used as a hydrophobic surface. Disposable tips were used while changing liquids, volume of 3 μL was dispensed using 30 μl tip, and the baseline was adjusted to measure the static contact angle as described by Sahasrabudhe, Staton and Farkas (2019). Parameters measured were drop height, base diameter, and contact angle (left side, right side, and mean).

5.2.4. Maximum bubble pressure tensiometer (MBPM)

A SensaDyne maximum bubble pressure tensiometer (Model Tracker QC6000; Mesa, AZ) was used to capture qualitative information on bubble formation. Nitrogen was introduced through a glass capillary submerged in the fluid at a flow rate that was controlled using an external flowmeter (EW-32014-15- 65 MM, Cole-Parmer, IL). The capillary was configured to release a bubble upwards (inverted). All capillaries had an initial diameter of 4 mm and either tapered down to a diameter of 0.5 mm, 1 mm or did not taper at all to give a tip diameter of 4 mm. All systems

were allowed a period of 10 min for equilibration once the flow rate was set. Once the system was equilibrated, videos of bubble formation and detachment were captured using the slow-motion capture feature of the iPhone 6s (240 frames/sec), attached to a macro lens (The 3rd Gen. Phone Macro Lens, 20X Magnification) to obtain a magnified image at a high resolution.

5.2.5. Submerged orifice assembly (SOA)

An assembly (Fig. 5.3) was built to understand the formation of bubbles from a submerged orifice. Pressurized nitrogen gas was supplied through an in-line regulator (625-04-04-01-00, Smith Equipment's, IN) connected to a flow meter (EW-32014-15- 65 MM, Cole-Parmer, IL), a pressure transducer (0-10 inch of water) (PX459-10WGI, OMEGA Engineering, INC, Norwalk, CT, USA), and finally to an orifice submerged in the fluid of interest through a T-fitting as described in Sahasrabudhe, Chaudhari and Farkas (2019). A transducer was used to measure pressure every 0.05 sec and was connected to a controller (TSISP16 ThinkStation, Team Labs, USA) which displayed the output as a current signal (4–20 mA). The current readings were converted to pressure data in units of Pascals using Eq. 5.1 based on the measurement ranges for the transducer and the controller. Flow rates of (1.25 ml/min, 2.5 ml/min, and 6 ml/min) were used to understand the effect of flow rate on the bubble dynamics.

$$\text{Pressure (Pa)} = \text{Current reading} * 155.53 \frac{\text{Pa}}{\text{mA}} \quad \text{Eq. 5.1}$$

The orifice was submerged in a 500 ml Pyrex beaker which was large enough such that the influence of the side walls was negligible (Denner, 2018). The beaker was filled with 400 ml of fluid to ensure that the liquid level was sufficient to prevent any environmental effects (Hayes et al., 1959; Denner, 2018). Bubble growth and departure were studied from a single orifice with diameters between 0.5–4 mm to understand the effect of pore size on bubble dynamics. The orifice diameters were selected based on Bo calculations, such that capillary controlled and gravity-controlled regimes would be obtained for all fluids studied. Experiments were conducted with glass capillaries (hydrophilic) as well as silanized glass capillaries (hydrophobic) so the effect of wettability on bubble dynamics could also be evaluated. All experiments were conducted at room temperature.

Videos of bubble formation and detachment were obtained using an iPhone 6s similar to the procedure described in section 5.2.4.

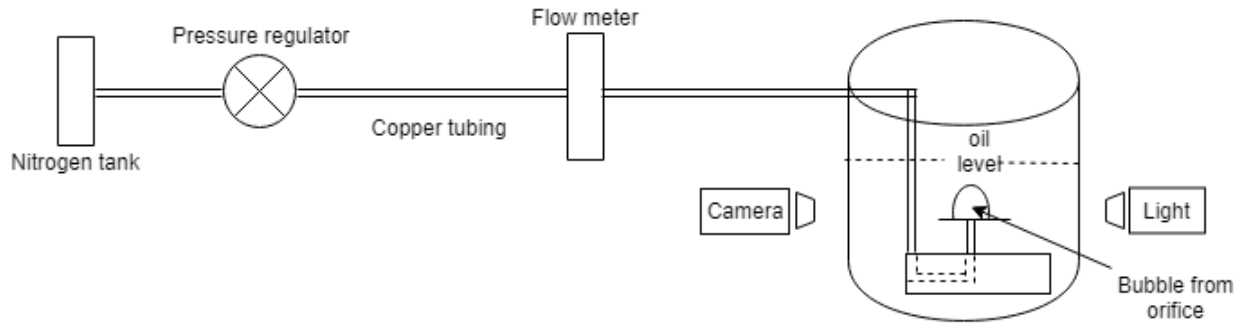


Fig. 5.3. Submerged orifice assembly to measure bubble dynamics. (Sahasrabudhe, Chaudhari and Farkas, 2019)

5.2.6. Force of curvature estimation

A MATLAB code was written to determine the axial and radial force of curvature during necking as the bubble pinches off from the capillary. The sum of the curvature forces helped to determine the direction of motion of the fluid after bubble pinch-off. Depending on the sample and image exposure, parameters in the script were tuned to obtain well defined boundaries for the bubble using the code described by Sahsrabudhe, Chaudhari and Farkas (2019). The first and second derivative of the boundary was calculated using MATLAB and conditions were set to obtain the coordinates of the necking arc. Based on the chord and the height of the arc, the axial radius (R_a) was obtained (Eq. 5.2). The radial radius (R_r) was half of the distance between the points on the arc with coordinates corresponding to the minimum distance based on the second derivative of the bubble boundary. Force of curvature (F_c) was then calculated using the general form of Laplace pressure (Eq. 5.3).

$$\text{Axial radius } (R_a) = \frac{\text{height}}{2} + \frac{\text{width}^2}{8\text{height}} \quad \text{Eq. 5.2}$$

$$F_c = \gamma * \left(\frac{1}{R_a} + \frac{1}{R_r} \right) \quad \text{Eq. 5.3}$$

5.2.7. Design of experiments

Experimental designs for the MBPM and SOA discussed above were developed based on the variables used and the parameters measured as described below. For both instruments, the fluids used were water, SDS in water, and glycerol in water. Effects of wettability were also tested with both instruments using glass and silanized glass capillaries.

For MBPM, flow rate, capillary diameter, fluid and surface properties were varied as described in Table 5.1. Only qualitative data for bubble behaviors as a function of fluid and liquid-solid properties were obtained from the MBPM. Observations of depth of entry or no entry of liquid inside the capillary between two consecutive bubbles were recorded.

For SOA, flow rate, capillary diameter, fluid and surface properties were varied as described in Table 5.1. Pressure was measured every 0.05 sec during bubble growth, detachment and the time between consecutive bubbles. Mean pressure and pressure drop during necking was calculated based on the pressure data. Bubbling frequency was obtained from the pressure data based on the sawtooth pattern of the signal. Qualitative observations of depth of entry or no entry of liquid inside the capillary between two consecutive bubbles were made using recorded video. Force of curvature during necking was calculated based on images obtained from the video data of the bubbling and processed using MATLAB code as described in section 5.2.6.

Table 5.1. Variables measured using the MBPM and SOA instruments

Variable	Maximum bubble pressure tensiometer (MBPM)	Submerged orifice assembly (SOA)
Flow rate (ml/min)	1.25, 2.5	1.25, 2.5, 6
Capillary diameter (mm)	0.5, 1, 4	0.5, 1, 2, 3, 4
Viscosity		
- Water and Glycerol	80 % glycerol	26.7 % and 80 % glycerol
Surface tension		
- Water and SDS	8 mM SDS	2.67 mM and 8 mM SDS
Surface properties	Glass capillaries Silanized glass capillaries	Glass capillaries Silanized glass capillaries

5.2.8. Statistical analysis

Measurements were performed in triplicate and data was analyzed using Minitab 17 (Minitab Inc., State College PA, USA). Regression (REG) analysis was performed on SOA pressure data for all fluids from both hydrophobic and hydrophilic capillaries. Tukey's test ($\alpha=0.05$) was used to determine differences among measured changes in pressure (ΔP) with changes in physical properties of fluids as well as change in the capillary wettability.

5.3. Results and Discussion

Density of the fluids was calculated using mixture formula (Eq. 5.4) and viscosity of glycerin solution was calculated using glycerin table (Glycerin Producers Association, 1963). Surface tension of all liquids was measured using the rising bubble technique described in section 5.2.2. Contact angle for all the fluids was measured on a glass coverslip and silanized coverslip using sessile drop technique described in section 5.2.3. The values for all measured and calculated physical properties are reported in Table 5.2. The force (F_γ) at triple contact point between the capillary surface, liquid and air was calculated using liquid properties (Eq. 5.5) (Table 5.2).

$$\rho_{mix} = \frac{\rho_1 V_1 + \rho_2 V_2}{V_1 + V_2} \quad \text{Eq. 5.4}$$

$$F_\gamma = \gamma \sin\theta \quad \text{Eq. 5.5}$$

where ρ_{mix} is the density of the mixture, ρ_1, ρ_2 and V_1, V_2 are the densities and volumes of the each fluid added, F_γ is the force at triple contact point, γ is the liquid surface tension, θ is the contact angle between the liquid and the capillary surface.

Table 5.2. Physical properties of fluids used for bubble formation experiments

Fluid	Surface tension (mN/m)	Viscosity (cP)	Density (g/ml)	Contact angle on cover-slip		Force at triple contact point ($\gamma \sin\theta$)	
				Non-silanized	Silanized	Non-silanized	Silanized
Water	73	1	1.00	32	110	38.42	68.14
26.7 % Glycerol	72	6	1.02	46	101	30.99	65.00
80 % Glycerol	64	60	1.21	42	92	27.84	63.46
2.67 mM SDS solution	56	60	1.00	10	67	9.72	51.16
8mM SDS solution	33	1	1.00	7	56	4.02	27.36

Bubble formation was studied using a maximum bubble pressure tensiometer and submerged orifice assembly (SOA) to understand the effect of liquid properties and liquid-solid interaction on meniscus dynamics during bubble formation. The variables studied were capillary

diameter, viscosity, liquid surface tension and capillary wettability. Gauge pressure during bubble formation and detachment from SOA was measured to understand the effect of liquid and liquid-solid properties on pressure changes as the meniscus enters the capillary. The pressure change occurred in a sawtooth pattern (Fig. 5.4). Differential pressure data from MBPM also showed a saw-tooth pattern (data not shown). Irrespective of the capillary diameter or liquid-solid properties, the pressure increased from initial meniscus formation until the formation of hemispherical cap at the capillary end which was the bubble lifetime. This was recorded as the maximum pressure similar to previous observations by (Dukhin et al., 1996; Dukhin et al., 1998a; Kovalchuk and Dukhin, 2001). The pressure then decreased as the bubble grew until pinch-off which was the deadtime.

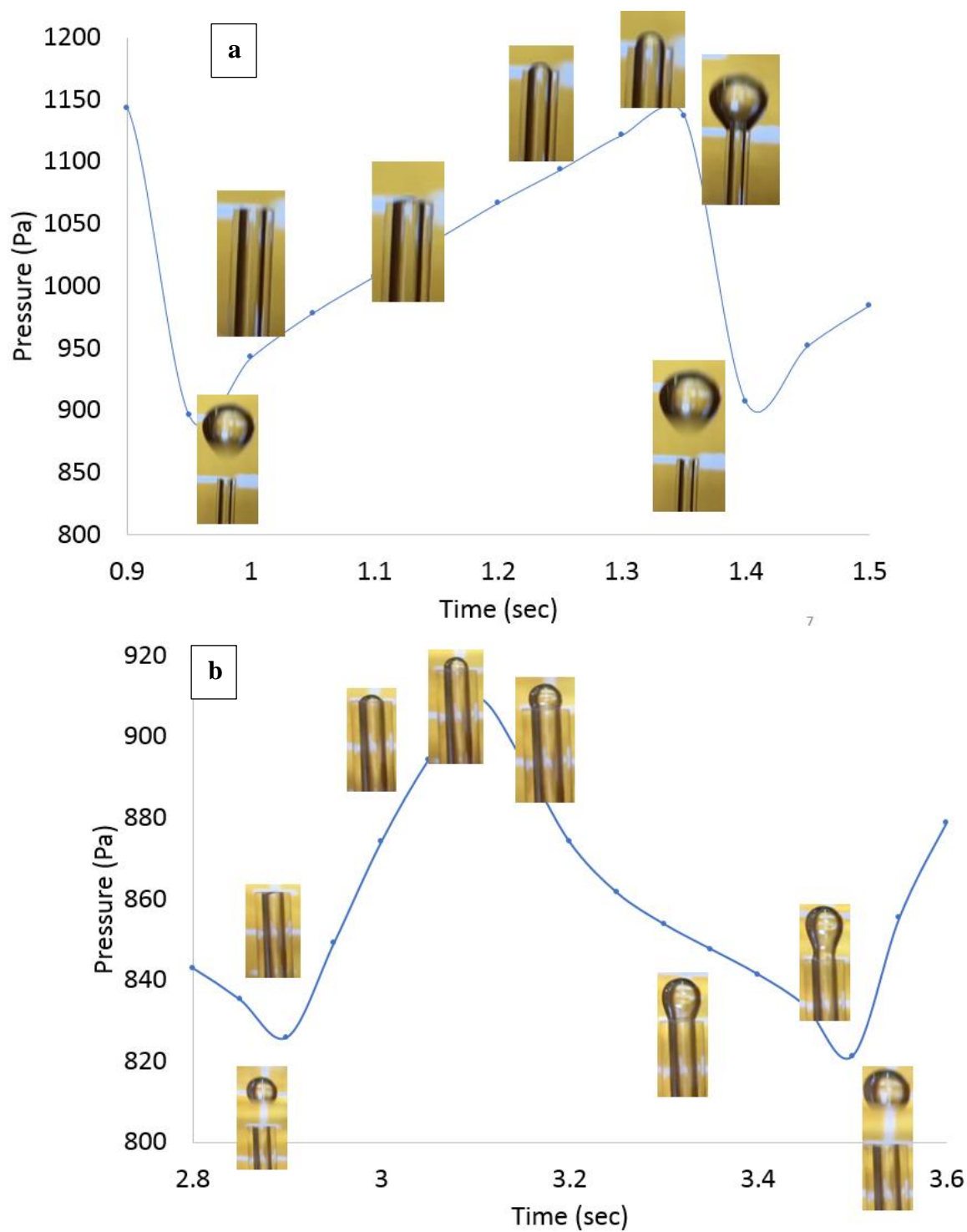


Fig. 5.4. Change in pressure during bubble formation and detachment for an upward facing capillary: a) 1 mm capillary b) 3 mm capillary

5.3.1. Effect of capillary diameter

The change in pressure as the bubble emerged from the capillary is represented in Fig. 5.4. Overall the sawtooth pattern was observed for all the capillary diameters studied. The mean pressure decreased with an increase in capillary diameter as was expected based on Bernoulli's principle (Widden, 1996). The motion of the meniscus between bubble formation was similar to the piston motion as discussed by (Ruzicka et al., 2009a, 2009b).

Weber number ($We = \frac{\rho v^2 d}{\gamma}$) was used to determine if flow behavior was dominated by inertial or surface tension forces. Weber number for all capillary diameters was calculated using gas properties. Based on Weber number values, bubbling was driven by surface tension forces when the capillary diameter (d) was > 0.5 mm. For the 0.5 mm capillary, $We \sim 1$ which could result in a jetting behavior. The video analysis of bubble formation from capillaries of different sizes also supports this theory. The meniscus did not fully form between consecutive bubbles for 0.5 mm capillaries. However, meniscus formation occurred for capillaries of 1, 2, 3 and 4 mm diameter. The depth of meniscus entry and mechanism of meniscus formation varied based on capillary diameter as described below.

Bond number ($Bo = \frac{\Delta \rho g d^2}{\gamma}$) was used to compare gravitational and surface tension forces during bubble dynamics. Based on theory, $Bo > 1$ signifies gravity controlled flow and $Bo < 1$ signifies capillary controlled flow (Stanovsky et al., 2011; Thome and Cioncolini, 2017). When $Bo > 1$, liquid weeps into the capillary after bubble detachment and is defined as gravity weeping. The Bond number and capillary length ($\lambda = \sqrt{\frac{\gamma}{\rho g}}$) were calculated for each fluid based on liquid properties (Table 5.1), and the bubble characteristics were divided into three regimes, capillarity, meniscus oscillation and weeping (Stanovsky et al., 2011). For the 0.5 mm capillary ($d \ll \lambda$), the flow was purely capillarity controlled. For the 4 mm capillary ($d \gg \lambda$), weeping was observed in the current study, and is in agreement with the literature findings (Peng et al., 2002; Stanovsky et al., 2011). For 1 mm, 2 mm and 3 mm capillaries ($d \sim \lambda$), surface tension and gravity forces were comparable. This resulted in meniscus oscillation in the time interval between consecutive bubbles and is in agreement with literature data (Stanovsky et al., 2011). The type of meniscus oscillation was categorized as a slow or fast oscillation (Dukhin, et al.1998a; Kovalchuk and Dukhin, 2001) as elaborated in the section 5.1.

The rate of change of pressure during bubble lifetime for the 0.5 mm and 1 mm capillaries, is less than deadtime $[(\frac{dP}{dt})_l \ll (\frac{dP}{dt})_d]$. The meniscus motion followed a piston-like behavior for all wetting fluids in a 1 mm capillary. This is characteristic of slow oscillation as described by Dukhin et al. (1998a). Hence, for the 1 mm capillary, the meniscus always enters the capillary for a wetting liquid. The depth of meniscus entry and the curvature of the meniscus is dependent on the liquid properties as well as liquid-solid interaction as described in section 5.3.3. For the 2 mm and 3 mm capillaries $[(\frac{dP}{dt})_l > (\frac{dP}{dt})_d]$. Meniscus oscillation for 2 mm and 3 mm capillaries post bubble detachment was observed irrespective of fluids studied. The meniscus oscillations in the time interval between bubbles is characteristic of fast oscillations as described by Dukhin et al. (1998b). The meniscus position in the capillary at which the pinch off occurs depends on the liquid surface tension and the solid-liquid wettability as discussed in section 5.3.3. Thus, the meniscus undergoes slow oscillations when it enters a 1 mm capillary for all fluids and it undergoes fast oscillations for the 2 mm and 3 mm capillaries.

The measured pressure change during bubble lifetime and dead-time is observed for all liquids at all capillary sizes. The size of the capillary influences whether the flow is gravity driven or capillarity driven and determines the type of meniscus oscillation between consecutive bubbles. The meniscus behavior as a function of capillary diameter is summarized in Table 5.3.

Table 5.3. Effect of capillary diameter on meniscus dynamics during bubble formation

Regime Type based on We		Observations (Type of oscillations)									
Fluid	Orifice diameter (mm)	0.5	1	2	3	4	0.5	1	2	3	4
Water	Capillarity	Capillarity/gravity driven			Gravity driven weeping		No meniscus entry-jetting	Liquid enters-small amount	Meniscus oscillates on surface	Meniscus oscillates on surface	Very small meniscus oscillation
SDS (2.66mM)		Capillarity/gravity driven			Gravity driven weeping			High amount of liquid entry	Meniscus oscillates inside capillary	Meniscus oscillates inside capillary	Weeping
Water + SDS (8 mM)		Capillarity/gravity driven	Gravity driven weeping			High amount of liquid entry		Meniscus oscillates inside capillary	Meniscus enters initially weeping-later stages	Weeping	
glycerol (26.7 %)		Capillarity/gravity driven			Gravity driven weeping			No liquid entry	Meniscus oscillates on surface	Meniscus oscillates on surface	Meniscus oscillates on surface
glycerol (80 %)		Capillarity/gravity driven			Gravity driven weeping			Liquid enters-small amount	Meniscus oscillates on surface	Meniscus oscillates on surface	Dampened oscillations on surface

5.3.2. Effect of liquid viscosity

The effect of liquid viscosity on meniscus dynamics during bubble formation was studied using water, and glycerol/water mixtures at two different concentrations of glycerol 26.7 % and 80 %. The properties of these fluids are summarized in Table 5.2.

There was no effect of viscosity ($p > 0.05$) on bubble lifetime and dead-time for all capillary diameters studied. Thus, the change in viscous forces (up to 60x) does not have an impact on the bubble formation process. This result agrees with previous findings in literature by (Davidson and Schüler, 1997; Gerlach et al., 2007; Majidi, 2015) where a negligible effect of viscosity on bubble formation time was observed at low flow rates.

In-order to further understand the effect of viscosity on bubble formation, change in pressure (ΔP) obtained from SOA data during bubble formation for all three fluids was compared (Fig. 5.5). The pressure values were not statistically different at 95 % confidence interval ($p > 0.05$) when compared using Tukey's test. The bubble shape in the three fluids, as well as the pattern of meniscus oscillations observed was not affected by a change in viscosity (Fig. 5.6).

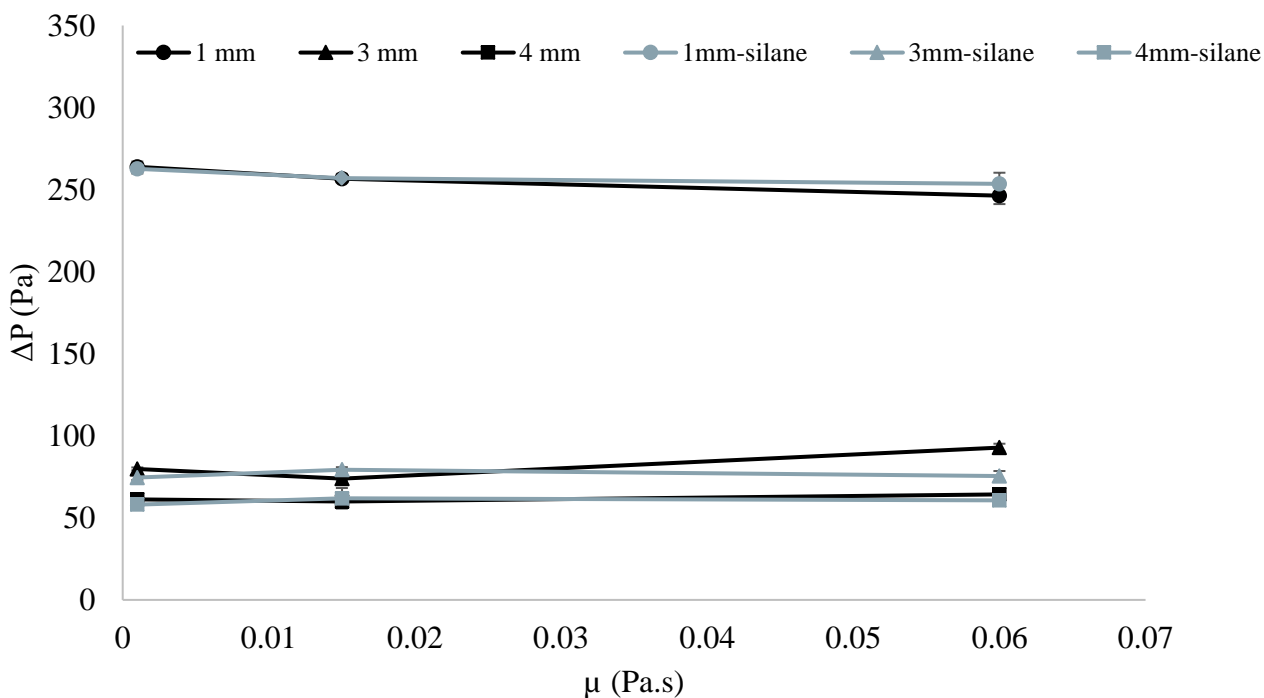


Fig. 5.5. Effect of viscosity on change in pressure during bubble formation and detachment. Results plotted for 1 mm, 3 mm and 4 mm (\circ , Δ , \square) diameters respectively for bubbles from glass and silanized capillaries.

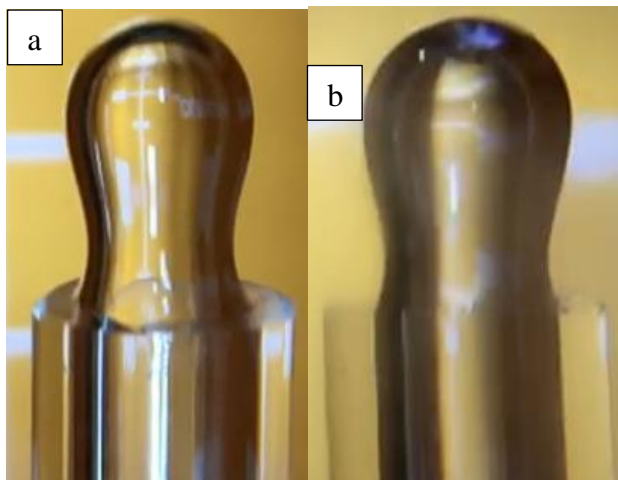


Fig. 5.6. Video snip of bubble formation in a) water from a 3mm glass capillary, b) 80 % glycerol from a 3 mm glass capillary

5.3.3. Effect of surface tension and contact angle

The effect of liquid surface tension on the meniscus dynamics during bubble formation was studied using water and SDS/water mixtures at two different concentrations of SDS, 2.67 mM and 8 mM. The effect of solid-liquid wettability was studied by conducting bubble formation experiments with all fluids on glass (hydrophilic) and silanized glass (hydrophobic) capillaries. The properties of these fluids and the contact angle on both surfaces are summarized in Table 5.2.

In order to understand the combined effect of surface tension and contact angle on meniscus dynamics during bubble formation, the force at triple contact point (F_γ) was calculated (Table 5.2). The change in pressure (obtained from SOA data) during bubble formation was plotted against F_γ to understand the effect of the liquid-solid properties on meniscus dynamics (Fig. 5.7). As contact angle increased, F_γ increased. However, ΔP decreased with an increase in F_σ when experiments were conducted using a wettable glass capillary. Conversely, ΔP increased with an increase in F_γ when conducting experiments using a non-wetting silanized capillary (Fig. 5.7). When statistical analysis was conducted, it was observed that there was no effect of silanization ($p > 0.05$) on ΔP values for water at all the capillary diameters studied. However, the ΔP values for bubble formation from a glass capillary \gg silanized capillary ($p < 0.05$) for SDS solutions at both concentrations and at all diameters of capillaries used. The differences in pressure amplitude were maximum for the 1 mm capillary where slow oscillations occurred.

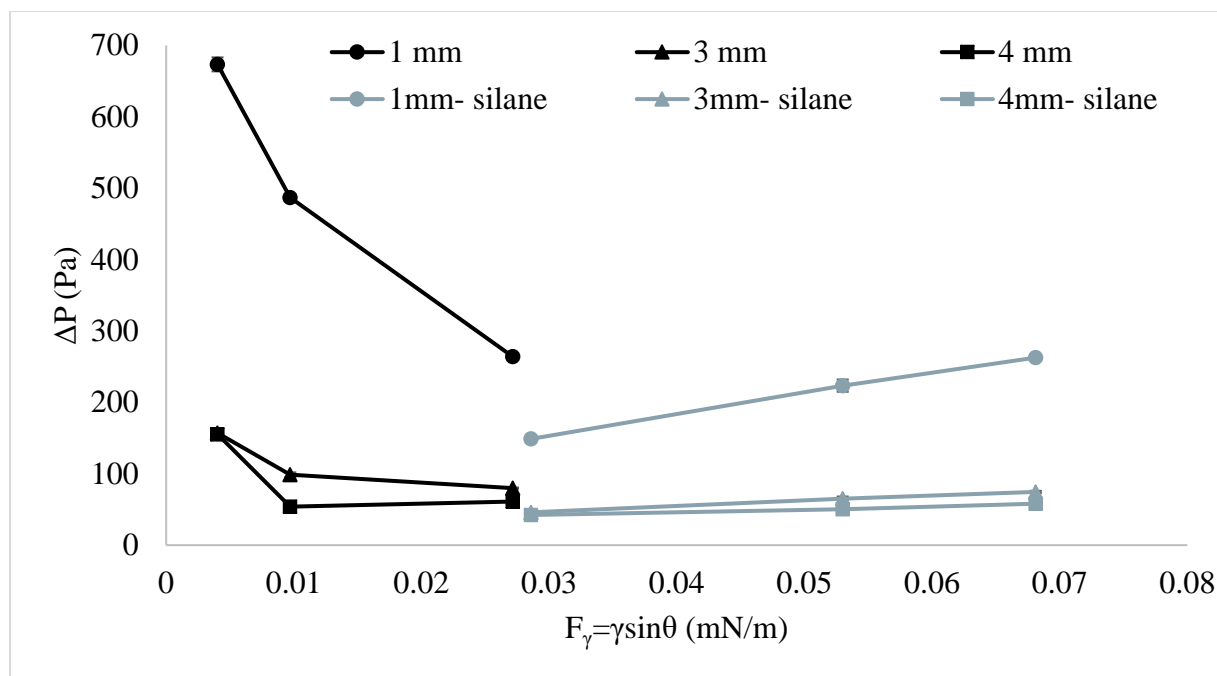


Fig. 5.7. Combined effect of surface tension and contact angle ($F_\gamma = \gamma \sin \theta$) on ΔP for 1 mm, 3 mm and 4 mm (\circ , Δ , \square) capillary diameters respectively for bubbles from glass and silanized capillaries.

Qualitative observation from videos of bubble formation were used to further understand the meniscus behavior due to changes in liquid properties and capillary wettability. The images shown (Fig. 5.8-5.10) are snips obtained from the bubble formation video data for the SOA instrument. Bubbles formed in SDS solutions at both concentrations (2.6 mM and 8 mM), exhibited the same behavior. Hence, snips for only the 8 mM SDS and water are reported for ease of understanding the results.

It was observed that the depth of liquid meniscus in the 1 mm glass capillary when SDS solutions (Fig. 5.8a) were used was greater compared to the meniscus depth for water (Fig. 5.8c). Thus, the entry of SDS solutions in glass capillaries results in high pressure drop observed with SDS (Fig. 5.7). For the 1 mm silanized capillary, the SDS liquid meniscus depth (Fig. 5.8b) was on the order of magnitude to that of water in the 1 mm glass capillary (Fig. 5.8c). There was no liquid entry observed with water (Fig. 5.8d) in the 1 mm silanized capillary. The water meniscus in 1 mm silanized capillary was concave instead of convex, due to the high contact angle between water and the silanized surface. The observations in the study are consistent with literature

observations (Dukhin et al., 1998a, Dukhin et al., 1998b, Fainerman and Miller, 1998) for slow oscillations where meniscus always enters the capillary if the liquid wets the capillary surface.

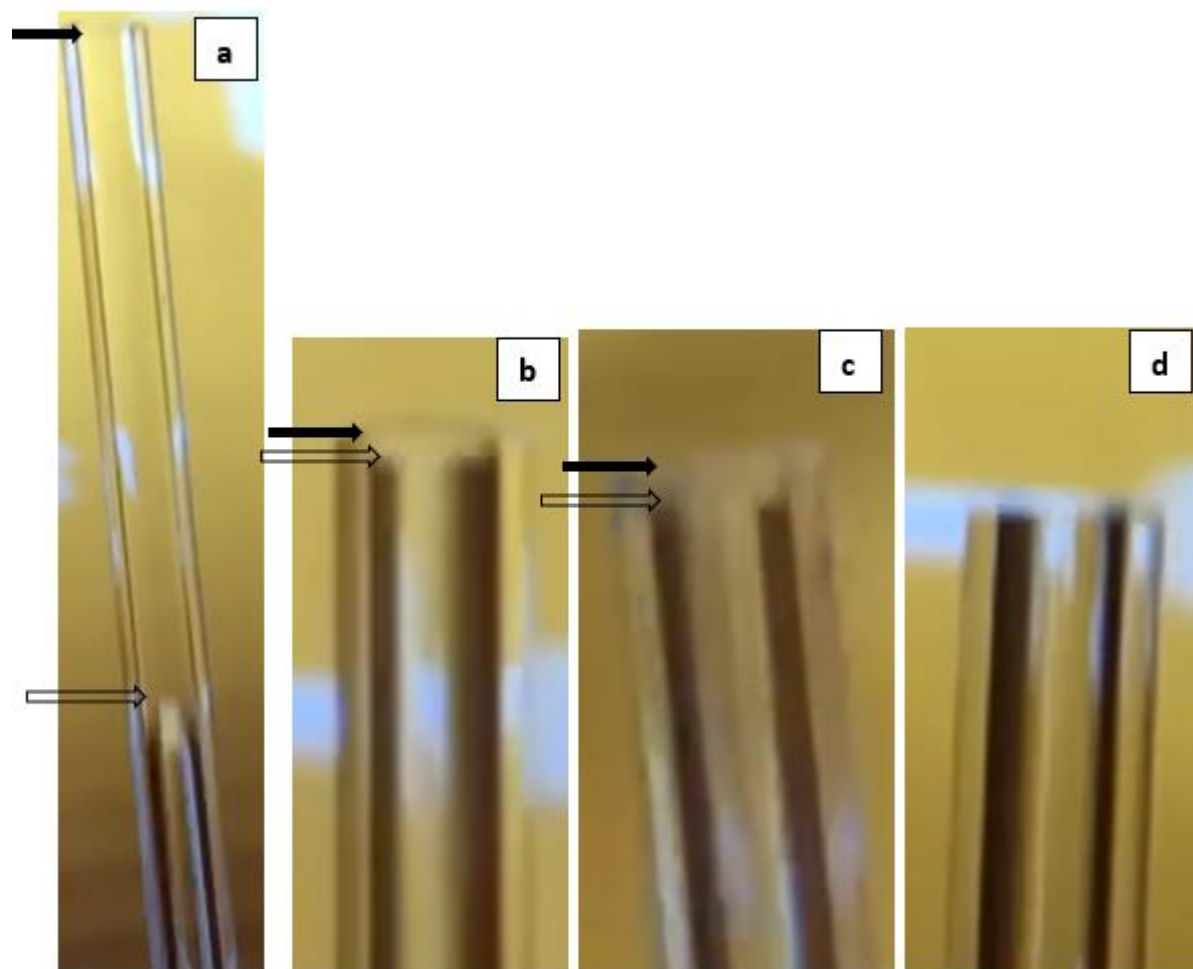


Fig.

5.8. Meniscus entry pattern during bubble formation from 1 mm capillary in a) 8 mM SDS solution from glass capillary, b) 8 mM SDS solution from silanized capillary, c) water from glass capillary, d) water from silanized capillary. Solid arrows (\blackrightarrow) indicate the capillary surface. Hollow arrows (\Rightarrow) indicate the meniscus surface.

Hollow arrows (\Rightarrow) indicate the meniscus surface.

Gravity weeping was observed in 4 mm glass capillaries for the low surface tension SDS solutions. The liquid wept into the capillary post bubble detachment and eventually bubbles were formed inside the capillary due to liquid accumulation (Fig. 5.9a). The pressure drop increased over time (observed with SOA data- data not reported) consistent with observations for weeping behaviors (Peng et al., 2002; Stanovsky et al., 2011). The weeping phenomena was not observed with water due to the high tension of the liquid (Fig. 5.9c), and the meniscus oscillated on the 4

mm capillary surface. For the 4 mm silanized capillaries, the liquid meniscus oscillated on the capillary surface for SDS and water (Fig. 5.9b and 5.9d) and no weeping phenomena was observed. This was attributed to the low wettability of the surface.

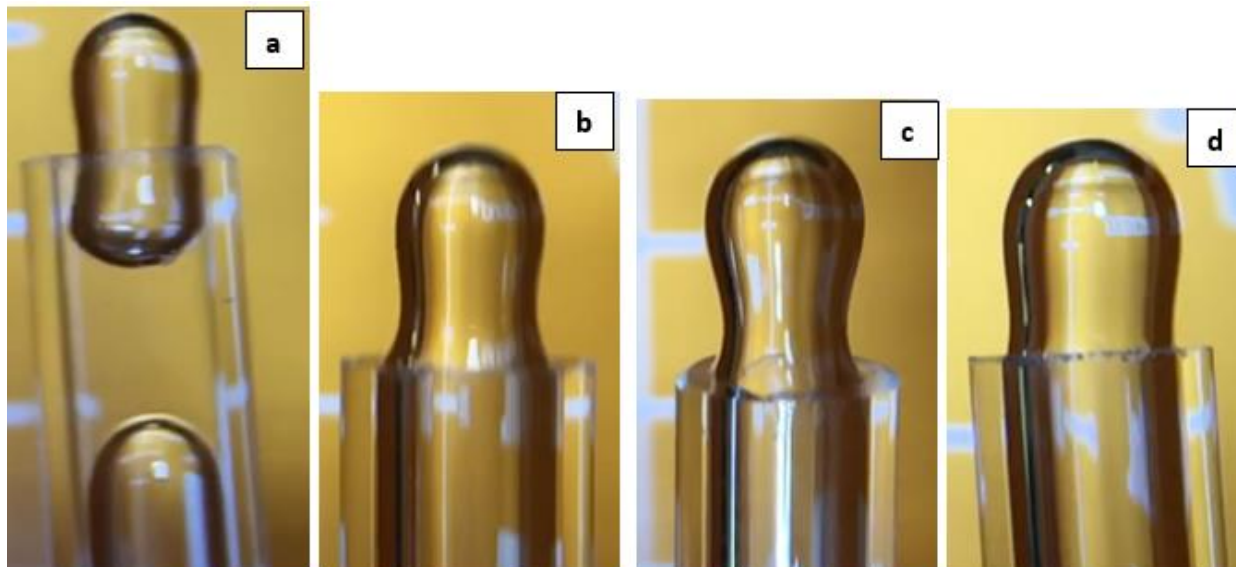


Fig. 5.9. Necking during bubble pinch-off from 4 mm capillary in a) 8 mM SDS solution from glass capillary, b) 8 mM SDS solution from silanized capillary, c) water from glass capillary, d) water from silanized capillary

For the 2 mm and 3 mm glass capillaries, bubble necking before pinch-off occurred inside the capillary for SDS solutions (Fig. 5.10a) and on the capillary surface for water (Fig. 5.10c). Liquid meniscus oscillations were observed at this position before the pressure started to rise again to form the next bubble. For the 2 mm and 3 mm silanized capillaries, the necking occurred on the capillary surface for SDS and water (Fig. 5.10b and 5.10d). Meniscus oscillations post bubble pinch-off observed for SDS and water were consistent with observation for fast oscillation of meniscus by Dukhin et al. (1998b) and Fainerman and Miller (1998). The position at which the meniscus oscillated was dependent on the force of curvature during necking as described below.

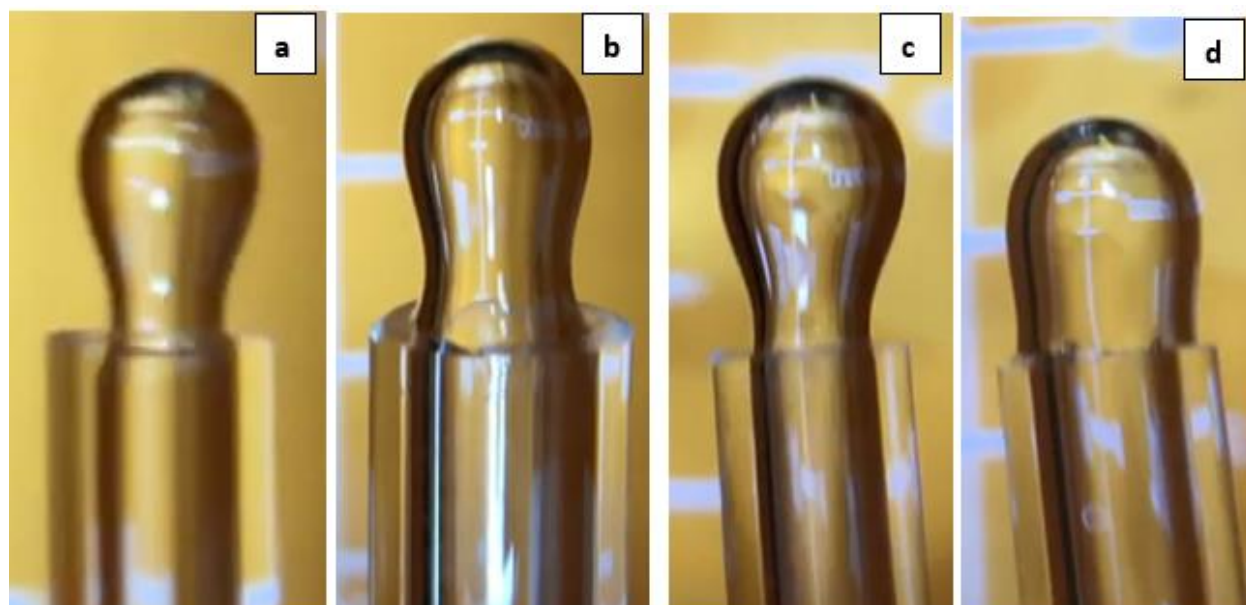


Fig. 5.10. Necking during bubble pinch-off from 3mm capillary in a) 8 mM SDS solution from glass capillary, b) 8 mM SDS solution from silanized capillary, c) water from glass capillary, d) water from silanized capillary

To quantify the effect of surface tension and contact angle on necking during bubble pinch-off, and thus on meniscus dynamics, force of curvature during necking was calculated using video snips from SOA data as described in section 5.2.6. A radial force acts along the neck radius resulting in constriction and pinch-off of the neck. An axial force is tangential to the neck and causes the entry of liquid into the capillary (Fig. 5.11). The balance between these opposing forces was responsible for the shape and motion of the meniscus post bubble pinch-off. For the 1 mm glass capillaries, the axial force \gggg radial force for the SDS solutions. Hence, there was a large entry of liquid observed inside the capillary. The liquid meniscus then moved back to the capillary rim as the pressure inside the capillary started building as described in the slow oscillation phenomena. For bubble formation in water from 1mm glass capillaries, and for SDS solutions from 1 mm silanized capillaries, the axial force $>$ radial force but the magnitude of difference was much less than the SDS solutions on 1mm glass capillaries. Thus, the meniscus entry was minimal in these cases. For the bubble formation in water from 1 mm silanized capillaries, the neck formation was insignificant. Hence, the axial force could not be calculated. Thus, the description of slow oscillation phenomena by Dukhin et al. (1998a) is valid only for wettable capillaries and can be explained on the basis force of curvature at necking estimations.

The axial force for bubble formation in SDS solutions was greater than radial force for the 2 mm and 3 mm glass capillaries. Therefore, liquid entered the capillaries during bubble formation, resulting in neck formation inside the capillary. The meniscus oscillated at the necking position followed by rising to the orifice rim as the pressure inside the capillary started building up during bubble formation. Thus, the necking occurs inside the orifice due to the force of curvature. However, in these capillaries, pressure is restored immediately after bubble detachment. Hence, the meniscus does not penetrate further into the capillaries. Instead it oscillates at the pinch-off position due to inertia and elasticity of gas as described by Dukhin et al. (1998b). For bubble formation in water from 2 mm and 3 mm glass and silanized capillaries and SDS solutions from 2 mm and 3 mm silanized capillaries, the axial force < radial force. Hence, the neck formation occurred at the capillary surface. Thus, there was no liquid entry during the time interval between consecutive bubbles. The meniscus oscillations at the capillary surface post bubble detachment were consistent with fast oscillation process reported by Dukhin et al. (1998b).

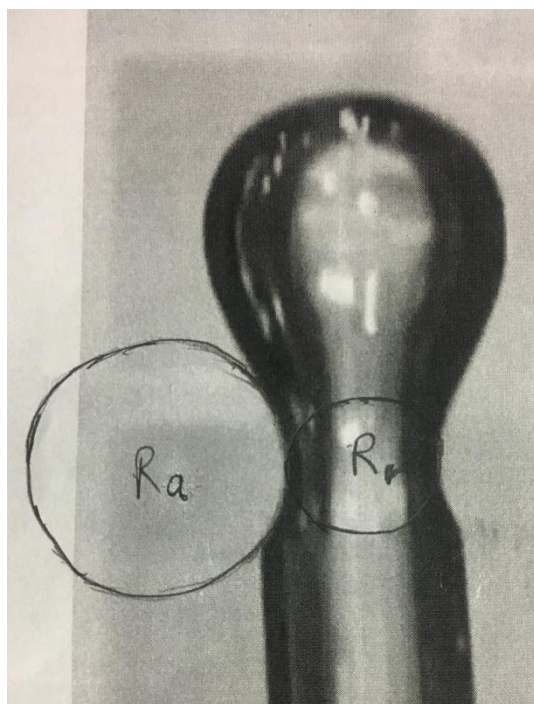


Fig. 5.11. Representative image for calculation radii of curvature during necking. R_a is the axial radius. R_r is the radial radius

5.4. Conclusion

This study concluded that for each fluid, capillary diameter and fluid properties can be used to predict if the bubble formation and meniscus dynamics is capillarity or gravity driven and can be estimated based on Bond number. For the capillarity driven regime, the depth of meniscus entry was dependent on the fluid surface tension and the solid-liquid wettability. For the capillarity/gravity driven regime, the type of meniscus oscillations was dependent on the rate of change of pressure during the bubble lifetime and deadtime. For the gravity driven regime, weeping occurred for low surface tension fluids on a wettable capillary. The study also found that fluid viscosity does not have an impact on bubble formation and meniscus dynamics from a submerged orifice. Fluid surface tension and contact angle between liquid and solid were thus primary factors controlling the meniscus behavior when comparing capillaries of the same size. For the long narrow capillaries, the depth of meniscus entry increased with increase in surface wettability and decrease in surface tension. For the short wide capillaries, the meniscus oscillated on the surface for the high-tension fluids. Meniscus oscillations occurred inside the capillary for low tension fluid with wettable capillaries. The forces of curvature at the time of necking can be used as a predictive parameter to estimate the depth of penetration of liquid inside long narrow capillaries, as well as the position of meniscus oscillations in short wide capillaries. Liquid surface tension as well as contact angle with the capillary surface were shown to have a significant effect on meniscus dynamics during bubble formation and thus can influence the bubble formation frequency, pattern and volume.

5.5. References

- Abraham, J.P., Gorman, J.M. (Eds.), *Advances in Heat Transfer*, Elsevier, pp. 157–224.
- Davidson, J. F., & Schüler, B. O. G. (1997). Bubble formation at an orifice in a viscous liquid. *Chemical Engineering Research and Design*, 75, S105–S115.
- Di Bari, S., & Robinson, A. (2013). Experimental study of gas injected bubble growth from submerged orifices. *Experimental Thermal and Fluid Science*, 44, 124–137.
- Dukhin, S. S. (1998). Hydrodynamic processes in dynamic bubble pressure experiments 2. Slow meniscus oscillations, 13. *Colloids and Surfaces A: Physicochemical and Engineering Aspects*, 138(1), 51-63.
- Dukhin, S. S., Fainerman, V. B., & Miller, R. (1996). Hydrodynamic processes in dynamic bubble pressure experiments 1. A general analysis. *Colloids and Surfaces A: Physicochemical and Engineering Aspects*, 114, 61–73.

- García, M., Ferrero, C., Bértola, N., Martino, M., & Zaritzky, N. (2002). Edible coatings from cellulose derivatives to reduce oil uptake in fried products. *Innovative Food Science & Emerging Technologies*, 3(4), 391–397.
- Gerlach, D., Alleborn, N., Buwa, V., & Durst, F. (2007). Numerical simulation of periodic bubble formation at a submerged orifice with constant gas flow rate. *Chemical Engineering Science*, 62(7), 2109–2125.
- Kalaikadal, D. S. (2012). A Parametric Investigation of Gas Bubble Growth and Pinch-off Dynamics from Capillary-tube Orifices in Liquid Pools. (Doctoral Dissertation). Retrieved from <https://etd.ohiolink.edu/>.
- Kovalchuk, V. I., & Dukhin, S. S. (2001a). Dynamic effects in maximum bubble pressure experiments. *Colloids and Surfaces A: Physicochemical and Engineering Aspects*, 192(1), 131–155.
- Kovalchuk, V. I., & Dukhin, S. S. (2001b). Dynamic effects in maximum bubble pressure experiments. *Colloids and Surfaces A: Physicochemical and Engineering Aspects*, 192(1–3), 131–155.
- Kulkarni, A. A., & Joshi, J. B. (2005). Bubble Formation and Bubble Rise Velocity in Gas–Liquid Systems: A Review. *Industrial & Engineering Chemistry Research*, 44(16), 5873–5931.
- Majidi, L. (2015). Influence of viscosity gradient on bubble formation at a submerged orifice. (Master of Science Thesis). Retrieved from <https://repository.library.northeastern.edu/files/neu:336865>
- Mallikarjunan, P., Chinnan, M. S., Balasubramaniam, V. M., & Phillips, R. D. (1997). Edible Coatings for Deep-fat Frying of Starchy Products. *LWT - Food Science and Technology*, 30(7), 709–714.
- McCann, D. J., & Prince, R. G. H. (1969). Bubble formation and weeping at a submerged orifice. *Chemical Engineering Science*, 24(5), 801–814.
- Mosdorf, R., & Wyszowski, T. (2010). Frequency and non-linear analysis of bubble paths in bubble chain. *Acta Mechanica et Automatica*, Vol. 4(4), 71–77.
- Peng, W. L., Yang, G., & Fan, L.-S. (2002). Experimental Studies of Liquid Weeping and Bubbling Phenomena at Submerged Orifices. *Industrial & Engineering Chemistry Research*, 41(6), 1666–1677.
- Ramakrishnan, S., Kumar, R., & Kuloor, N. R. (1969). Studies in bubble formation—I bubble formation under constant flow conditions. *Chemical Engineering Science*, 24(4), 731–747.
- Ras, R. H. A., Tian, X., & Bayer, I. S. (2017). Superhydrophobic and Superoleophobic Nanostructured Cellulose and Cellulose Composites. In H. Kargarzadeh, I. Ahmad, S. Thomas, & A. Dufresne (Eds.), *Handbook of Nanocellulose and Cellulose Nanocomposites* (pp. 731–760). Weinheim, Germany: Wiley-VCH Verlag GmbH & Co. KGaA.

- Ruzicka, M. C., Bunganic, R., & Drahoš, J. (2009). Meniscus dynamics in bubble formation. Part I: Experiment. *Chemical Engineering Research and Design*, 87(10), 1349–1356.
- Simmons, J. A., Sprittles, J. E., & Shikhmurzaev, Y. D. (2015). The formation of a bubble from a submerged orifice. *European Journal of Mechanics - B/Fluids*, 53, 24–36.
- Stanovsky, P., Ruzicka, M. C., Martins, A., & Teixeira, J. A. (2011). Meniscus dynamics in bubble formation: A parametric study. *Chemical Engineering Science*, 66(14), 3258–3267.
- Thome, J. R., & Cioncolini, A. (2017). Flow Boiling in Microchannels. In E. M. Sparrow, J. P. Abraham, & J. M. Gorman (Eds.), *Advances in Heat Transfer*, Vol. 49, pp. 157–224.
- Wang, Y., Huang, C., & Wu, X. (2016). Influencing Factors and Scaling Law of Bubble Detachment at a Submerged Orifice. In *Volume 7: Fluids Engineering* (p. V007T09A043). Phoenix, Arizona, USA: ASME.
- Widden, M. (1996). *Fluid Mechanics*. Macmillan International Higher Education.
- Yu, X., Wang, Y., Huang, C., & Du, T. (2015). Three stages of bubble formation on submerged orifice under constant gas flow rate. *Journal of Physics: Conference Series*, 656(1), 012042.
- Yuan, Y., & Lee, T. R. (2013). Contact Angle and Wetting Properties. In *Surface Science Techniques*, pp. 3–34.
- Zahedi, P., Saleh, R., Moreno-Atanasio, R., & Yousefi, K. (2014). Influence of fluid properties on bubble formation, detachment, rising and collapse; Investigation using volume of fluid method. *The Korean Journal of Chemical Engineering*, 31(8), 1349–1361.
- Zhang, L., & Shoji, M. (2001). Aperiodic bubble formation from a submerged orifice. *Chemical Engineering Science*, 56(18), 5371–5381.

6. CONCLUSIONS AND FUTURE WORK

Surface and interfacial tension (IFT) affect transport rates of fluid across interfaces, dispersion of solids in liquid, droplet formation in spraying, and stability of emulsions. Raw materials and food products are processed at elevated temperatures to render them safe and desirable. However, little is known about the effect of temperature on interfacial properties. Immersion frying is one such technique to process food by heating in oil at 160-200°C. During frying, there is simultaneous heat and mass transfer causing the food to absorb oil, as it loses moisture in the form of steam.

The current study showed that the primary property that changes as oil degrades due to use during frying is the contact angle of oil on a surface. Oil wettability increases as oil degrades due to use in frying. Surface tension and contact angle are primary factors that influence bubble formation and meniscus dynamics from a submerged orifice and hence could affect heat transfer and oil absorption during frying as the oil quality degrades. Increased heat transfer and oil absorption as oil degrades during frying can hence be related to the increase in wettability with degraded oil. Results from meniscus formation in the time interval between subsequent bubbles show that the entry of liquid is dependent on the orifice diameter, liquid surface tension and wettability. Small pore sizes of food will thus tend to absorb more oil due to the slow oscillations phenomena explained in this study. The depth of penetration is highly dependent on the surface tension and solid-liquid wettability. Higher wettability and lower surface tension will result in increased oil absorption during immersion frying. Developing new oleophobic matrices/ coatings can thus help to reduce oil absorption during immersion frying.

Studies in the past have shown that oil wettability also influences drainage of oil during post-frying cooling. The drainage phenomenon is a balance between oil viscosity and wettability. Studies on oil absorption reduction have shown gum coatings to be effective in oil reduction up to 50 %. In earlier studies, the mechanism of oil absorption reduction by use of edible coatings is hypothesized to be altering the water-holding capacity of foods by trapping moisture inside and preventing the replacement of water by oil (García et al., 2002; Mallikarjuna et al., 1997). However, the exact mechanism for the functioning of these coatings has still not been understood. Furthermore, video data from frying experiments conducted in the present study (data not shown)

with coated and uncoated potato chips did not show differences in bubble formation pattern which is an indicator of moisture loss.

Based on conclusions drawn from studies in this dissertation, wettability is a major factor influencing adhesion, hence can affect oil drainage during post-frying cooling. Hence, preliminary studies were conducted to measure contact angle between oil and coated and uncoated steel surfaces. The steel surfaces were coated with oleophobic NS- 200 coating (NanoSlic[®], Greenley, CO, USA) and different commonly used gum coatings such as 1 % MC, 1 % guar, 1 % pectin, and 1 % each of pectin and MC. The contact angle between the different surfaces and vegetable oil was measured using sessile drop technique described in chapter 3. The preliminary results are shown in Table 6.1.

Table 6.1. Effect of coatings on contact angle with vegetable oil

Surface	Contact angle (°)
Uncoated Steel	17.4
1 % Pectin	20.1
1 % each Pectin + MC	20.6
1 % Guar	24.6
1 % MC	40.4
NS- 200 steel	77.5

The results show that contact angle is lowest for an uncoated steel surface indicating it is highly wettable. With the use of oleophobic coatings (NS- 200), angles of around 70° were obtained. The oil droplets roll off the surface of the NanoSlic coated steel. Coatings such as pectin had a small effect on the contact angle, however, with MC, contact angle of 40° was observed. MC is shown to be an effective coating in reducing oil absorption. Hence the decrease in oil absorption with the use of food gums as coatings may be attributed to the decrease in coated food surface wettability. Development of GRAS oleophobic coatings could promote drainage of oil during post-frying cooling and thus reduce oil absorption. However, experiments were conducted only on a coated steel surface. For direct application of results to frying, studies on porous food surfaces need to be conducted with an aim to develop matrices that have low oil wettability leading to reduced oil absorption in fried food.